Improving methods to search for signatures of astronomical chaos in time series

Dissertation

zur Erlangung des
Doktorgrades der Naturwissenschaften
- Dr. rer. nat. –

im Fachbereich Geowissenschaften
der Universität Bremen

vorgelegt von
Melanie Reinelt

Bremen, Juni 2019

Erstgutachter: Prof. Dr. Heiko Pälike, Universität Bremen
Zweitgutachter: Prof. Dr. Frits Hilgen, Universiteit Utrecht

Das Promotionskolloquium fand am 1. November 2019 statt.

“Words are flowing out
Like endless rain into a paper cup
They slither wildly as they slip away across the universe…”

- John Lennon

“Mars is bright tonight.”

- Ronan

Preface

This PhD thesis is submitted for the doctoral degree in natural sciences (Dr. rer. nat.) at the Faculty of Geosciences, University of Bremen, Germany. The research described herein was conducted under the supervision of Prof. Dr. Heiko Pälike at the Paleoceanography group at MARUM – Center for Marine Environmental Sciences and Faculty of Geosciences, University Bremen, Germany between June 2016 and May 2019. The PhD project was funded by the European Research Council Consolidator Grant EarthSequencing (617462). The thesis is written in cumulative form and includes the collection of three manuscripts. In total, the dissertation has 5 chapters.

Melanie Reinelt

Acknowledgement

First of all, I would like to thank my supervisor Prof. Dr. Heiko Pälike for giving me the opportunity to conduct this PhD project. Your knowledge is incredible, and I truly appreciate you sharing it with me. I thank you for all the ideas and input from your side.

Further I want to thank Christian Zeeden for all the fruitful discussions and your vast support. Thank you for your quick revisions, your excitement about the methods and your help with the manuscripts.

I also like to thank my working group Paleoceanography for sharing your experiences and knowledge with me.
Thank you, Mathieu, for your great introduction into this topic at the beginning of my PhD and for your support during the first year. Further I thank you for your helpful comments and ideas for the second manuscript.
Thank you, Heather, for your English! I'm happy that I was the one who had the pleasure teaching you, in return, one of the most important German words ‚Arschgeige'. I will never forget our paddling and running… Ouch!

I like to thank Prof. Frits Hilgen for agreeing on being the second reviewer of my thesis.

At this point I would also like to say thank you to some friends. Foremost, thank you Dieter, for your constant motivation and support, and for being a friend. Thank you, Natalie, for all the nice coffee breaks (once upon a time), the pleasant conversations and for sharing your PhD-thing experience with me. Thank you, Mick and Thomas for cheering me up and feeding me with cookies. I thank Abby for her calm and smooch temper. Thanks for purring!
Last but not least, I would like to acknowledge myself. After all the hard times I've gone through in my life, completing my PhD is an incredible miracle. Thank you, Mel!

Table of contents

Abstract

Incoming solar radiation (insolation) received on Earth is controlled by Earth's rotational parameters and its distance from the sun. These quasi-cyclic variations in the Earth's eccentricity, axial tilt, and precession, also called Milankovitch cycles, alter the local and global climate on Earth in time scales of 10^4 to 10^6 years. As astronomically forced climate variation is imprinted in sediments, this information can be utilized in combination with other stratigraphic and dating methods to establish precise and high-resolution geological time scales. Astronomical time scales have been constructed by tuning cyclic climatic records to theoretical orbital solutions. These astronomical models are calculated with present (initial) conditions. However, the chaotic dynamics of the Solar System pose limits on the prediction and calculation of an accurate solution for the orbital and precessional motion of the Earth over more than ~50 Ma. One main manifestation of astronomical chaos is quantifiable in resonance changes of the secular (fundamental) frequencies between Mars (g_4, s_4) and Earth (g_3, s_3). The frequencies g_3 and g_4 are associated with the precession of the perihelion, the closest approach to the Sun. The frequencies s_3 and s_4 relate to the precession of the nodes, the intersection of the orbital plane with the reference plane. The resonance of 2:1 defined as $2(s_4 - s_3) = (g_4 - g_3)$ changes into a 1:1 resonance expressed as $(g_4 - g_3) = (s_4 - s_3)$.
The challenge is to detect resonance changes induced by astronomical chaos in the geological record in order to test and extend the applicability of theoretical astronomical models. This would contribute to the precision of astronomically tuned age models which are needed to reconstruct Earth history.

This PhD thesis aims to address this challenge by providing reliable methods to detect chaotic transitions in geological time series and by searching for signatures of astronomical chaos during the last 66 Million years.

Manuscript 1 (**Chapter 2**) demonstrates a conceptual approach of thorough tests and applications of various techniques to identify chaotic transitions in time series. The approach, consisting of frequency analyses combined with filter and amplitude investigations, is based on a step-by-step development with the help of different

astronomical solutions. The tests initiated with a non-noisy eccentricity and obliquity solution (La2004), were subsequently applied on ZB17e, a solution consisting of eccentricity and inclination, and then extended to the eccentricity solution La2010c enhanced with additional auto-regressive noise. A final test on real geological data conclude, that although frequency and amplitude analyses pose difficulties when conducted separately, the combination of methods increase the robustness of the application.

After developing improved and reliable methods, the second aim is to search for chaotic transitions during the last 66 Ma. In Manuscript 2 **(Chapter 3),** previously tested methods were applied on a splice of seven IODP/ODP datasets representing iron content from globally distributed sites. This splice covers the Eocene, Paleocene and encompasses the Cretaceous-Paleogene boundary. Applying frequency analyses, two chaotic transitions were indicated between ~44 – 52 Ma and ~62 – 66 Ma. The combination of amplitude modulation and additional filter investigations could confirm these results. The detected transitions are most in accordance with the calculations of La2010a and La2010d.

Two recent studies report evidences for astronomical chaos: Study a) detected two chaotic transitions in the Late Cretaceous between 84 and 93 Ma and study b) identified a ~1.747 Myr short $g_4 – g_3$ period (recently: ~ 2.4 Myr). Manuscript 3 (**Chapter 4**) demonstrates the test of previously improved methods on preferably various type of data and to support the results of Chapter 3. For testing the application, sonic velocity and gamma radiation of study b) and Formation Micro-Resistivity Imaging data of study a) were chosen, representing geophysical borehole measurements. A further test was conducted on $\delta^{13}C$ data of study a). The application of frequency analyses and further amplitude investigations indicated evidences for astronomical chaos in agreement with the respective studies, consistent with the astronomical solutions La2004 (a) and La2010d (b).

Kurzfassung

Die auf der Erde eintreffende Sonneneinstrahlung wird durch die Rotationsparameter der Erde und ihrer Entfernung von der Sonne gesteuert. Diese quasi-zyklischen Variationen in der Exzentrizität, der Obliquität und der Präzession der Erde, auch Milankovitch-Zyklen genannt, verändern das lokale und globale Klima auf der Erde in Zeitskalen von 10^4 bis 10^6 Jahren. Da astronomisch forcierte Klimaveränderung in Sedimenten eingeprägt ist, kann diese Information, in Kombination mit anderen Stratigraphie- und Datierungsmethoden, genutzt werden, um präzise und hochauflösende geologische Zeitskalen zu erstellen. Die astronomischen Zeitskalen werden durch Abgleichung klimatischer Zyklen auf theoretische Orbitallösungen konstruiert. Diese theoretischen, astronomischen Modelle werden mit heutigen (Anfangs-) Bedingungen berechnet. Die chaotische Dynamik des Sonnensystems schränkt jedoch die Vorhersage und Berechnung einer exakten Lösung für die Orbital- und Präzessionsbewegung der Erde über ~50 Millionen Jahre ein. Eine der wichtigsten Erscheinungsformen von astronomischem Chaos ist in Resonanzveränderungen der säkularen (fundamentalen) Frequenzen zwischen Mars (g_4, s_4) und Erde (g_3, s_3) quantifizierbar. Die Frequenzen g_3 und g_4 werden mit der Präzession des Perihels, dem sonnennächsten Punkt, in Verbindung gebracht. Die Frequenzen s_3 und s_4 beziehen sich auf die Präzession der Knoten, der Schnittpunkt der Orbitalebene mit der Referenzebene. Die Resonanz von 2:1, definiert als $2(s_4 - s_3) = (g_4 - g_3)$, ändert sich in eine 1:1-Resonanz, ausgedrückt als $(g_4 - g_3) = (s_4 - s_3)$.
Die Herausforderung besteht darin, Resonanzveränderungen, die durch astronomisches Chaos verursacht werden, in geologischen Daten zu erkennen, um die Anwendbarkeit theoretischer astronomischer Modelle zu testen und zu erweitern. Dies würde zur Präzision von astronomisch getunten Altersmodellen beitragen, die für die Rekonstruktion der Erdgeschichte verwendet werden.

Diese Doktorarbeit nimmt sich dieser Herausforderung an und liefert verlässliche Methoden, um chaotische Übergänge in geologischen Zeitreihen zu erkennen und nach Signaturen für astronomisches Chaos in den letzten 66 Millionen Jahren zu suchen.

Manuskript 1 (**Kapitel 2**) demonstriert einen konzeptionellen Ansatz ausführlicher Tests und Anwendungen verschiedener Techniken, um chaotische Übergänge in Zeitreihen zu identifizieren. Der Methodenansatz, bestehend aus Frequenzanalysen kombiniert mit Filter- und Amplitudenuntersuchungen, basiert auf einer schrittweisen Entwicklung mit Hilfe verschiedener astronomischer Lösungen. Die Tests, die mit einer rauschfreien Exzentrizitäts- und Präzessions- Lösung (La2004) eingeleitet wurden, wurden anschließend auf ZB17e angewandt, einer Lösung, die Exzentrizität- und Inklinationsberechnungen liefert, und dann auf die Exzentrizitäts-Lösung (La2010c) inklusive zusätzlich zugefügtem auto-regressiven Rauschen erweitert. Ein abschließender Test an realen geologischen Daten kommt zu dem Schluss, dass Frequenz- und Amplitudenanalysen bei separater Durchführung zwar Schwierigkeiten bereiten, die Kombination der Methoden aber die Robustheit der Anwendung erhöht.

Nach der Entwicklung verbesserter und zuverlässiger Methoden ist das zweite Ziel die Suche nach chaotischen Übergängen während der letzten 66 Ma. In Manuskript 2 (**Kapitel 3**) wurden zuvor getestete Methoden auf einen Datensatz, bestehend aus sieben zusammengesetzten IODP/ODP-Datensätzen, angewendet, die den Eisengehalt von global verteilten Lokationen darstellen. Dieser Datensplice umfasst das Eozän, das Paläozän und die Kreide/Paläogen-Grenze. Bei der Anwendung von Frequenzanalysen wurden zwei chaotische Übergänge zwischen ~44 – 52 Ma und ~62 – 66 Ma angezeigt. Die Kombination aus Amplitudenmodulation und zusätzlichen Filteruntersuchungen konnten diese Ergebnisse bestätigen. Die entdeckten Übergänge stimmen mit den Berechnungen von La2010a und La2010d überein.

Zwei neuere Studien berichten von Beweisen für astronomisches Chaos: Studie a) entdeckte zwei chaotische Übergänge in der Spätkreide zwischen 84 und 93 Ma und Studie b) identifizierte eine ~1.7 Myr kurze g_4 – g_3 Periode (heute: ~2.4 Myr). Manuskript 3 (**Kapitel 4**) präsentiert das Testen der vorher optimierten Methoden auf vorzugsweise verschiedene Arten von Daten und unterstützt die Ergebnisse von Kapitel 3. Für die Prüfung der Anwendbarkeit wurden sonic velocitiy und gamma radiation Daten der Studie b) und Formation Micro-Resistivity Imaging Daten der Studie a) ausgewählt, die geophysikalische Bohrlochmessungen repräsentieren. Ein weiterer Test wurde an $\delta^{13}C$ Daten von Studie a) durchgeführt. Die Anwendung von

Frequenzanalysen und weiteren Amplitudenuntersuchungen zeigte Hinweise für astronomisches Chaos im Einklang mit den jeweiligen Studien und übereinstimmend mit den astronomischen Lösungen La2004 (a) und La2010d (b).

Chapter 1

General Introduction

1.1. Motivation and research aim

Quasi-periodic variations in the Earth's rotation parameters, Earth's position within its orbit, and its distance to the Sun force variations in incoming solar radiation (insolation). Insolation alternations lead to climate cycles on Earth of time scales from 10^4 to 10^6 years. These astronomically driven cycles are recorded in various sedimentary geo archives and became an important part of integrated stratigraphy (Cyclostratigraphy) (e.g. Hays et al., 1976; Hinnov, 2013, Hilgen et al., 2015). Age models based on cyclostratigraphy are often adjusted to theoretical astronomical models as sequencing template. These astronomical solutions are calculations and approximations with present (initial) conditions. However, due to the gravitational interactions of the bodies within the Solar System it is theoretically impossible to precisely predict the behaviour of the bodies from their current positions, masses and velocities (Laskar, 1990). The "chaotic" behaviour induced by gravitational interactions between the bodies in the solar system, including a strong chaotic behaviour between the asteroids Ceres and Vesta, poses limits to integrate Earth's astronomical motions. Consequently, the establishment of astronomical solutions for creating astronomically calibrated geological time scales is limited beyond 50 Ma with enough precision (Laskar, 1999). The aim of this thesis is to develop a methodology to determine signatures of astronomical chaos in the geological record in order to test and verify theoretical astronomical models. This would extend the applicability of astronomical solutions for serving as tuning targets and contribute to the precision of astronomically tuned age models.

1.2. The elements of the Earth's orbit

1.2.1. Geophysical parameters and fundamental frequencies of the Solar System

Earth's climatic variations are caused by changes in shape and orientation in and of the elliptical orbit as a consequence of the gravitational interactions between all bodies of the Solar System. Figure 1.1 illustrates that position, shape, and orientation of an orbit and the location of a body in an orbit at any given time are represented by six geophysical parameters (Keplerian elements) **a, b, i, λ, ω, Ω.** The element **a** is the semi-major and **b** the semi-minor axis of the orbital ellipse, **e** the eccentricity of the

ellipse, **i** is the inclination describing the angle between the orbital and the reference plane. The longitude of the ascending node **N** is described by the angle **Ω** measured from a fixed position (vernal (spring) equinox, γ). The position of the perihelion (closest approach to the Sun) P and its motion $\tilde{\omega}$ is defined by $\tilde{\omega} = \Omega + \omega$ (longitude of the perihelion) (e.g. Berger, 1988, 1980; Pälike, 2005).

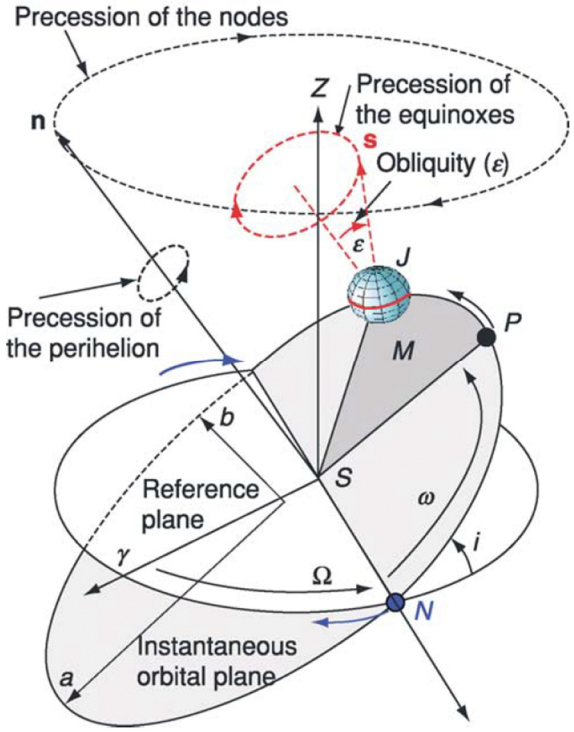

Figure 1.1 Earth's astronomical parameters showing an elliptical Earth orbit with major axis a and minor axis b, the precession of the perihelion (P), the axial tilt (Obliquity, ε), the precession of the equinoxes (γ), and the precession of the nodes (N). Inclination i describes the angle between the orbital and the reference plane (Pälike, 2005).

Knowledge of the planetary motions and orbits forms the basis for estimating the Earth's orbital parameters that affect insolation. The individual fundamental frequencies of each planet of the Solar System (1. Mercury, 2. Venus, 3. Earth, 4. Mars, 5. Jupiter, 6. Saturn, 7. Uranus and 8. Neptune) are combined in the terms g_i and s_i. The term g_i refers to the orbital elements e (eccentricity) and ω (longitude of the perihelion) and describe the variation of a body in its orbit whereas s_i is related to i (inclination) and Ω (longitude of the ascending node) and describe the orientation and motion of an orbital plane with respect to a reference plane. As s_i frequencies arise

from counterclockwise motions, these are negative. The fundamental frequency of Jupiter (s_5) is zero due to its large mass and because of the angular momentum conservation within the system (Zeebe, 2017). The axial or general precession (in Figure 1.1: Precession of the equinoxes) is defined by sin ω, where ω is the angle between the northern hemisphere spring equinox γ and the perihelion P. The origin of the general precession is a 'nodding' motion (nutation) of the Earth's spin axis resulting from lunar and solar (and other planets) gravitational pull acting on the Earth. The spinning top and the gravitational force result into a 'wobble' motion (Lambeck, 1980). This precession rate k or p has a recent period of ~25.8 kyr (Berger, 1976; Laskar et al., 2004) but it is affected by tidal dissipation and dynamical ellipticity.

Table 1.1. Fundamental frequencies of each planet (arcseconds/year) calibrated from Laskar (2011) with periods (kyr). g_i are Eigenmodes that refer to corresponding planets. The periods/kyr were calculated with $1 / \frac{360*60*60}{\text{Frequency (arcseconds/year)}}$

Planet	Term	Frequency ("/year)	Period (kyr)	Term	Frequency ("/year)	Period (kyr)
Mercury	g_1	5.590	231.8	s_1	-5.610	-231.0
Venus	g_2	7.453	173.9	s_2	-7.060	-183.6
Earth	g_3	17.368	74.6	s_3	-18.848	-68.8
Mars	g_4	17.916	72.3	s_4	-17.751	-73.0
Jupiter	g_5	4.257	304.4	s_5	0.000	
Saturn	g_6	28.245	45.9	s_6	-26.348	-49.2
Uranus	g_7	3.088	419.7	s_7	-2.993	-433.1
Neptune	g_8	0.673	1925.7	s_8	-0.692	-1873.5
Pluto	g_9	-0.350	-3702.1	s_9	-0.350	-3702.1

1.2.2. Eccentricity

Earth's orbital eccentricity **e** quantifies the amount by which the Earth's orbit deviates from a perfect circle, while e = 0 represents a circular orbit. Eccentricity is the only orbital parameter that influences the total annual insolation received by Earth's surface. However, changes in Earth's orbital eccentricity are very small. The present eccentricity of the Earth is e ≈ 0.01671 and has varied between 0 and 0.06 in the past (Berger and Loutre, 1991; Laskar et al., 1993). More significant is the influence of

eccentricity on the variation of the distance between the Earth and the Sun throughout the year and on the insolation at the closest (perihelion) and furthest (aphelion) position to the Sun.

The period of long eccentricity (~405 ky) arises from the interactions of the planets Venus and Jupiter calculated from fundamental frequency components of these planets ($g_2 – g_5$) and is the most stable eccentricity cycle stabilized by Jupiter's large mass (Laskar 2011). The interactions of different frequency components produce beat terms, the origin of amplitude modulation terms. Long eccentricity is a modulation of interfering short eccentricity terms, for example ($g_4 - g_5$) - ($g_4 - g_2$) result into $g_2 – g_5$ (~405 kyr) (see Table 1.2 for all frequency terms of eccentricity). This type of modulation also appears for short eccentricity (and all other orbital cycles) and is explained in detail in section 1.2.4. Amplitude modulation. Eccentricity frequencies are independent of the precession constant p (Jacques Laskar, 1999).

Table 1.2 Principal components of eccentricity calculated from La2010a (Laskar 2011). s_i and g_i are Eigenmodes that refer to corresponding planets (Table 1.1). Periods in kyr were calculated with $1 / \frac{360*60*60}{\text{Frequency (arcseconds/year)}}$

Term	Frequency (arcseconds/year)	Period (kyr)
g2 - g5	3.196	405.6
g4 - g5	13.659	94.9
g4 - g2	10.463	123.9
g3 - g5	13.111	98.9
g3 - g2	9.915	130.7

1.2.3. Obliquity

The obliquity or axial tilt **ε** is defined by the angle between the rotational and orbital axis of the Earth (Figure 1.1). It determines the angle of insolation, and thus the latitudinal distribution of insolation (strongest at high latitudes) and the seasonal contrast. The greater the tilt, the more intense are the seasonal differences in both hemispheres (Imbrie et al., 1993). The recent obliquity of 23.44° (Laskar et al., 1993) changes between ~22 and 24.5° with a dominant periodicity of ~41 kyr due to motions of **i** and **Ω** of Mars and Earth's orbit (s_3 and s_4) and with major amplitude modulations at 173 kyr and 1.2 Myr. As the Earth's general precession rate p (or k) depends on

Earth's rotational speed, dynamical ellipticity and the Earth-Moon distance which have varied through geological time, obliquity (and precession) cycles were shorter in the past (Berger and Loutre, 1994; Berger et al., 1989).

Table 1.3 Principal components of obliquity calculated from La2010a (Laskar 2011). p is the "constant" of general precession of the Earth with a recent period of ~25.8 kyr. si and gi are Eigenmodes that refer to corresponding planets (Table 1.1). Periods in kyr were calculated with $1 / \frac{360*60*60}{\text{Frequency (arcseconds/year)}}$

Term	Frequency ("/year)	Period (kyr)
$p + s_3$	31.443	41.2
$p + s_4$	32.540	39.8
$(p + s_3 + g_4 - g_3)$	31.991	40.5
$p + s_6$	23.943	54.1
$(p + s_3 - g_4 + g_3)$	30.89	41.95
$p + s_1$	44.68	29.01

1.3. Amplitude modulation, the 'fingerprint' of orbital cycles

An important fact of all orbital components is that their frequencies interfere with each other and generate long-period beats. It is possible to verify – for example – the eccentricity signal by the amplitude modulation of precession (Shackleton et al., 1995) because changes in eccentricity determine the amplitude of the climatic precession, as the climatic precession, e*sin ω, is defined by the product of eccentricity e and the axial precession (sin ω). As demonstrated in a Thomson Multitaper (Thomson, 1982) evolutive spectrum of the astronomical calculation La2004 (Laskar et al., 2004) from 0 to 10 Ma (Figure 1.2), a modulation in amplitudes also applies for eccentricity (~100 kyr -> ~405 kyr -> ~2.4 Myr) and obliquity (~41 kyr -> ~173 kyr -> ~1.2 Myr). The long term eccentricity ~2.4 Myr period arises from the term $g_4 – g_3$, while $s_4 - s_3$, with a period of ~1.2 Myr, should be evident in the modulation of obliquity (Hinnov, 2000; Jacques Laskar, 1999; Laskar, 1990; Laskar et al., 1993).

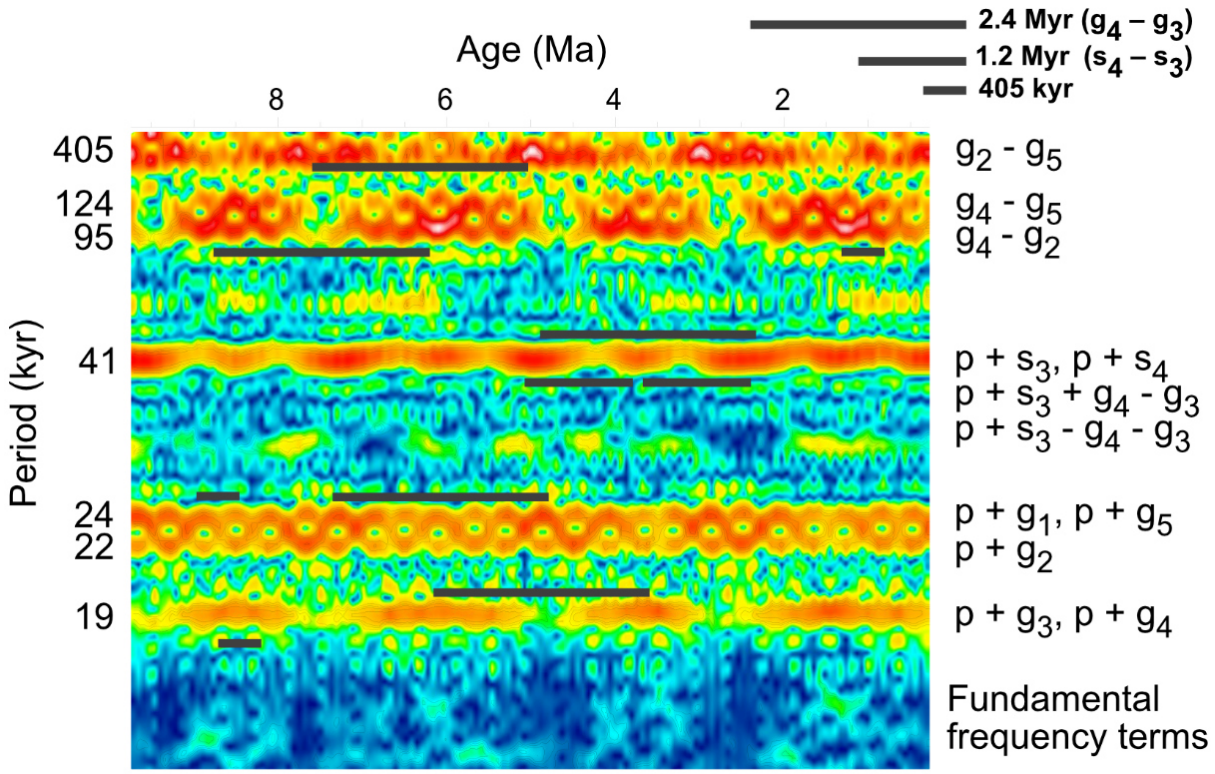

Figure 1.2 Thomson Multitaper (Thomson, 1982) evolutive spectrum of the astronomical calculation La2004 (Laskar et al., 2004) from 0 to 10 Ma, generated by using a macOS tool. The analyses show the relative amplitude at a particular frequency and time, while red corresponds to a high amplitude, blue to a low amplitude. some amplitude modulation terms of $g_3 - g_4$ (2.4 Myr), $2(g_3 - g_4)$ (1.2 Myr), and 405 kyr arising from different frequency terms are highlighted. Fundamental frequency components producing the periods of long eccentricity (405 kyr), short eccentricity (95, 124 kyr), obliquity (41 kyr), and precession (24, 22, and 19 kyr) are specified.

The grand 2.4 and 1.2 Myr eccentricity and obliquity cycles can be determined in the geological record, although the interfering higher frequencies that produce them can't be measured directly in sedimentary records due to a lack of resolution (Olsen et al., 2019). A clear imprint of relevant orbital variations is important for amplitude investigations; otherwise results may be dominated by noise (Zeeden et al., 2015) The long-term amplitude modulations of eccentricity and obliquity (precession amplitude modulation is equal to eccentricity amplitude modulation) are summarized in Table 1.4.

Table 1.4 Relevant amplitude modulation terms for eccentricity and obliquity from interfering terms to "beat" terms with periods. p is the "constant" of general precession of the Earth (with a recent period of ~25.8 kyr) but which itself is influenced over time by e.g., tidal dissipation. s_i and g_i are Eigenmodes that refer to corresponding planets (Table 1.1).

Type	'Interfering' term	'Beat' term	Period
long and short eccentricity amplitude modulation terms	$(g_4 - g_5) - (g_4 - g_2)$ $(g_3 - g_5) - (g_3 - g_2)$	$(g_4 - g_5)$	405 kyr
	$(g_4 - g_5) - (g_3 - g_5)$ $(g_4 - g_2) - (g_3 - g_2)$	$(g_4 - g_3)$	2.4 Myr
obliquity amplitude modulation terms	$(p + s_3) - (p + s_4)$	$(s_4 - s_3)$	1.2 Myr
	$(p + s_3 + g_4 - g_3) - (p + s_3 - g_4 + g_3)$	$2(g_4 - g_3)$	1.2 Myr
	$(p + s_3) - (p + s_3 + g_4 - g_3)$	$(g_4 - g_3)$	2.4 Myr
	$(p + s_3) - (p + s_3 - g_4 + g_3)$		

1.4. Astronomical solutions

Since Milankovitch published the first full astronomical theory of glaciation proposing that Pleistocene ice ages on the Northern Hemisphere were related to cyclic changes in the distribution of insolation across the Earth (Milanković, 1941), astronomical models evolved from analytical approximations to detailed, numerical solutions.

35 years after Milankovitch, Hays et al. (1976) reconstructed sea surface temperatures and determined the climate response of precession and obliquity over the past 500,000 years. By this time, Bretagnon (1974) computed the terms of planetary eccentricity and inclination, which was then used to for the calculation of precession and insolation quantities of the Earth by Berger (1978).

Following these developments, Laskar realized strong divergences in the system of the inner planets, so that the traditional methods could not be used for the integration of the secular equations. To overcome this difficulty, he switched to a numerical integration which stepwise resulted into a full solution for precession and obliquity of the Earth (Laskar, 1990). Following Quinn et al. (1991), Laskar et al. (1993) refined their astronomical model by including parameters for tidal dissipation, valid from 0 to 35 Ma (La1993). With the improvements in computer technology, Laskar et al. (2004)

and Varadi et al. (2003) were able to provide a long term integration of the orbital motion of the Solar System based on Lunar Laser Ranging (LLR) observations. Both orbital solutions, Varadi et al. (2003) and La2004 Laskar et al. (2004), are valid from 0 to 40 Ma, but the main limitations due to the chaotic motion of the Solar System remain (Jacques Laskar, 1999; Laskar, 1990).

Due to its stability the 405-kyr eccentricity can be used for orbital tuning far back in time. While the initial conditions of La2004 (Laskar et al., 2004) were adjusted to the JPL ephemeris DE406 (Standish, 1998), La2010 (Laskar et al., 2011a) incorporates two new planetary ephemerides INPOP06 and INPOP08 (Fienga et al., 2009, 2006) and also includes the five major asteroids, Ceres, Vesta, Pallas, Iris and Bamberga. The solution La2010d has been fitted to the INPOP06 ephemeris, while solutions La2010a, La2010b, La2010c have been fitted INPOP08. However, later emerged that INPOP06 is probably more precise, and Westerhold et al. (2012) showed that geological data is better represented by La2010d. Improved solar system observations allowed a new high precision algorithm to be developed, INPOP10a (Fienga et al., 2011). This then lead to the construction of a new long-term solution La2011, which additionally took into account the strong chaotic behaviour induced by Ceres and Vesta that complicates the Earth's orbital eccentricity calculation (Laskar et al., 2011b). All solutions were referred to the International Celestial Reference Frame J2000.

The most recent solutions of the orbital and precessional motion of the Earth (ZB17a - p) were presented by Zeebe (2017). He used new integrator algorithms to calculate different solutions adjusted to DE431 (Folkner et al., 2014) and INPOP13c (Fienga et al., 2014) ephemerides, with the Moon as a separate object and with an Earth–Moon gravitational quadrupole. He also included 9 Planets and 10 Asteroids, valid from 0 to 54 Ma. A special feature of ZB17 solutions is, that the reference frame was rotated to fit with the solar quadrupole moment which is directed along the solar rotation axis. The inclination offset is about 7° from the invariable plane and ECLIPJ2000. ECLIPJ2000 refers to ecliptic coordinates based on the J2000 frame. The inclination to the invariable plane of J2000 is ~1.57° (Souami and Souchay, 2012).

1.5. Cyclostratigraphy and its limitations

Astronomically forced climate change, and the cycles it leaves in the sedimentary record, has become an important part of integrated stratigraphy (Cyclostratigraphy) (e.g. Hays et al., 1976; Hinnov, 2013, Hilgen et al., 2015). Cyclostratigraphy, radioisotopic numerical dating and other standard stratigraphic are now increasingly combined to establish precise and high-resolution geological time scales. Tying cyclic variations in the sedimentary record to astronomical target curves has resulted into, for example, the Astronomically Tuned (Neogene) Time Scale (ATNTS: (Gradstein et al., 2012; Hilgen et al., 2012; Hinnov and Hilgen, 2012) extended to the Oligocene (Pälike et al., 2006) and, for the Paleogene, the Geological Time Scale (GTS) (e.g., GTS2012, Gradstein et al., 2012). Cyclostratigraphic durations of e.g. biozones or magnetochrons and relative age spans between biostratigraphic events have also been used to test and refine radioisotopic ages (e.g. Meyers et al., 2012b; Westerhold et al., 2012; Zeeden et al., 2014). In addition, orbital tuning has been used to investigate the Earth's climate response to astronomical forcing (Berger, 1989; Hays et al., 1976; Meyers et al., 2012a; Pälike et al., 2006).

1.6. Chaotic behaviour of the Solar System

In 1990, Laskar discovered the chaotic behaviour of the Solar System due to the gravitational interactions of the bodies in the Solar System. He determined 'chaotic zones' of the planets based on the variation of the main fundamental frequencies of each planet and noted the largest variation in the orbits of the inner planets (Mercury, Venus, Earth and Mars) (Laskar, 2015). In addition, the close encounters of the orbits of Ceres and Vesta induce a strong chaos and influence the calculation of Earth's eccentricity (Laskar et al., 2011b). One quantifiable chaotic motion of the Solar System manifests itself in resonance changes of the secular (fundamental) frequencies between Mars and Earth. The frequencies of Mars' and Earth's orbit expressed in $(g_4 - g_3) - 2(s_4 - s_3)$ oscillate at present at 0, in libration. But this motion does not persist for ever and can evolve into a new state, into circular and even more into libration motion with different $g_4 - g_3$ and $2(g_4 - g_3)$ periods afterwards. During the circular motion, the expression $(g_4 - g_3) - 2(s_4 - s_3) = 0$ changes into $(g_4 - g_3) - (s_4 - s_3) = 0$. This implies a change from a 2:1 resonance into a 1:1 (Laskar, 1999). This resonance change should be observable in the cyclostratigraphical record by investigating amplitude modulation

patterns of eccentricity and obliquity as implemented by Shackleton et al. (1999) and Pälike et al. (2004), who extracted the 1.2 Myr obliquity and the 2.4 Myr eccentricity period and precession amplitude modulation for a 12 Myr-long interval of ODP Leg 154 and 199 spanning the Oligocene-Miocene boundary. They demonstrated the feasibility differentiating between astronomical models with (La1993 (Laskar et al., 1993)), and without a chaotic transition, as predicted in La2004 (Laskar et al., 2004) and confirmed the absence of astronomical chaos within this time interval.

1.7. Searching for evidences for astronomical chaos – state of the art

Searching for chaotic events has received increased research attention in recent years. In this section, some of the most important studies are mentioned.

After interpretation of anhysteretic remanent magnetization (ARM) data from the Maokou Formation of the Shangsi section, South China, Fang et al. (2015, 2017) state that the 2:1 secular resonance of $g_4 – g_3$ and $s_4 – s_3$ is preserved throughout the section, and that the orbits of Earth and Mars maintained the 2:1 resonance until the end of the Late Paleozoic Ice Age. They also observed slightly shorter $g_4 - g_3$ and $s_4 - s_3$ periodicities in the Early–Middle Permian than those observed in the Cenozoic Era. Later, they reported a resonance transition in magnetic susceptibility measurements of the Luokun section, South China in the Chinese Carboniferous (early Moscovian; Fang et al., 2018). Wu et al., (2018) reported evidences for five chaotic resonance transitions between 300 - 330 Ma in the continental section at Naqing, South China.

Using the Geological Orrery, a network of orbital records, Olsen et al. (2019) analysed Triassic-Jurassic (202 – 229 Ma) lacustrine and fluvial sediments of the Newark Basin and Colorado Plateau. With spectral (Multitaper Method and Wavelet) and Frequency analyses of depth rank and colour from recovered cores and sonic-velocity and gamma radiation borehole measurements, they detected at 1.7 Myr $g_4 - g_3$ eccentricity period during this time interval, matching the La2010d eccentricity solution (Laskar et al., 2011a). This shorter $g_4 - g_3$ period represents a fingerprint of Solar System chaos.

More recent chaotic events have been detected in the Late Cretaceous in North American Libsack (82 – 90 Ma) and Iona (90 – 97 Ma) cores. Ma et al. (2017) reported one 1:1 resonance ‘transition zone’ in Formation Micro-Resistivity Imaging (FMI) data, a proxy for carbonate content, of the Libsack core between 84 and 88 Ma. In 2019 they extended their assessment using grayscale and $\delta^{13}C$ data of the Iona core in order to

find out, whether the 2:1 resonance was present in the Solar System before this transition. In doing so, they discovered another transition between 89 and 93 Ma (Ma et al., 2019).

The most recent transition was reported by Westerhold et al. (2017) at ~52 Ma in multiple proxy analyses, matching well to La2010b and La2010c (Laskar et al., 2011a) and also to Zb17e (~54 Ma; Zeebe, 2017).

The discovery of ancient chaotic intervals is a significant step forward, however, the most critical time to investigate for chaotic transitions is those closest to the terminus of astronomical solution accuracy previous to 55 Ma (Hinnov, 2018).

1.8. Fundamental frequency analyses

One technique to analyse the chaotic motion of the Solar System is based on Laskar's Numerical Analysis of Fundamental Frequencies (NAFF) algorithm. Like Fourier transformation the NAFF algorithm converts a quasiperiodic signal into its frequency domain but even more precisely than Fourier transformation. The analyses of the variation of the fundamental frequencies over a defined time enables the detection of astronomical chaos.

A quasiperiodic function of time with complex values for a given number of Terms **N** is

$$\mathbf{f(t)}=\sum_{\mathbf{k=1}}^{\mathbf{N}} a'_k e^{i\,\nu'_k t}$$

where a_k are amplitudes decreasing with **k**.

The NAFF algorithm computes a'_k and ν'_k in an iterative way for a finite time span t. A weight function is used to find the maximum amplitude and the first periodic term $e^{i\,\nu'_1 t}$, in order to calculate the first frequency ν'_1 from the complex amplitude a'_1 obtained by orthogonal projection. Then the process is restarted on the remaining part of the function $\mathbf{f1(t)} = \mathbf{f(t)} - a'_1 e^{i\,\nu'_1 t}$. Detailed mathematical principles are given by Laskar (2003), Laskar (1993), Papaphilippou (1999) and Valluri and Merritt (1998).

1.9. Specific objectives

The objectives of this thesis are as follows

- **To develop and improve methods to detect chaotic transitions in time series**
  In order to improve and extend the applicability of astronomical models, it is crucial to detect signatures of astronomical chaos in the geological record. To achieve this, reliable methods are essential. Therefore, various techniques are tested on time series with well-known positions of chaotic transitions.

- **To create a continuous and high-resolution dataset for over 35 million years to serve a useful record to search for evidences for astronomical chaos**
  As one main manifestation of astronomical chaos should be detectable in the evolution of $g_4 - g_3$ and $2(g_4 - g_3)$ periods in eccentricity and obliquity amplitude modulation, a complete and long geological record is essential. The most critical time to investigate for chaotic transitions is those closest to the terminus of astronomical solution accuracy previous to 55 Ma, so a splice covering at least the Eocene and the Paleocene is needed.

- **To search for evidences for chaotic behaviour during the last 66 Million years**
  Application of the in 1) tested and developed methods on the record generated in 2) to search for chaotic transitions.

- **To decide which astronomical solution match geological best to improve the applicability of theoretical solutions for developing age models.**
  After applying the in 1) developed methods on the record 2), it should be possible to determine, which solutions match geological data.

1.10. Thesis outline

This dissertation comprises an 'introductory' chapter (**Chapter 1**) followed by three stand-alone manuscripts (**Chapters 2, 3 and 4**). **Chapter 5** summarises the main conclusions of the three manuscripts, discusses the main findings, the limitations of the methods and provides ideas for future research.

The research goals mentioned in section 1.1 and outlined in 1.9 were addressed in three individual manuscripts. Manuscript 1 and 2 have been submitted to peer-reviewed international journals and the third is in preparation for submission.

The writing and design of the manuscripts and figures were done by myself. All co-authors contributed to the discussion and interpretation and provided comments and suggestions on the manuscripts. Heiko Pälike provided FORTRAN codes for computing both fundamental (NAFF) and instantaneous frequency analyses, and a macOS tool for calculating Thomson Multitaper (Thomson, 1982) evolutive spectra. The R-Script to test optimal filter settings for the identification of orbital frequencies was scripted by Christian Zeeden (Zeeden et al., 2018), but discussed and adapted for this thesis. Mathieu Martinez gave an introduction and training to spectral analyses and assisted with creating the splice for Manuscript 2. As Chapter 2 and 3 are stand-alone manuscripts that base on the first, some repetitions are mandatory.

Chapter 2 "Detecting chaotic transitions in geological time series: Applying improved methodologies"

Melanie Reinelt, Christian Zeeden, Heiko Pälike

Status: Submitted to *Planetary and Space Science.*

This chapter presents thorough analyses and tests of various methods to identify chaotic transitions in time series. The conceptual and methodological approach consists of fundamental and instantaneous frequency analyses and additional filter and amplitude investigations and is based on a step-by-step development on different astronomical solutions and a final test on real geological data.

Chapter 3 "Investigating astronomical chaos in the Eocene-Paleocene-Late Cretaceous 69 - 34 Ma

Melanie Reinelt, Christian Zeeden, Mathieu Martinez, Heiko Pälike

Status: Submitted to *Earth and Planetary Science Letters.*

The second manuscript demonstrates the application of previously tested techniques consisting of frequency analyses and amplitude investigations on a splice of seven IODP/ODP datasets representing iron content from globally distributed sites. This splice covers the Eocene, the Paleocene and encompasses the Cretaceous-Paleogene boundary. The analyses indcated two chaotic transitions between ~44 – ~52 Ma and ~62 – ~66 Ma which are most in accordance with the calculations of La2010a, La2010d and ZB17e.

Chapter 4 "Testing astronomical transitions in the Mesozoic with improved methodologies"

Melanie Reinelt, Christian Zeeden, Heiko Pälike

Status: In preparation for submission to e.g. *Geophysical Research Letters.*

Demonstrated in manuscript three, the previously developed techniques are subjected to further tests. In order to cover various type of data and studies reporting evidences for the chaotic behaviour of the solar system, we selected two studies: Olsen et al. (2019) who discovered a 1.747 Myr $g_4 - g_3$ grand eccentricity period in sonic velocity and natural gamma borehole logs of Triassic-Jurassic (202 – 229 Ma) lacustrine/fluvial sediments: and b) Ma et al. (2019) who detected two chaotic transitions in Formation Micro-Resistivity Imaging (FMI) and $\delta^{13}C$ data of the Late Cretaceous (82 – 97 Ma).

1.11. References

Berger, A.&, Loutre, M.F., 1994. Astronomical forcing through geological time, in: Orbital Forcing and Cyclic Sequences (IAS Special Publication), P. L. de Boer and D. G. Smith, Eds. pp. 15–24.

Berger, A., 1989. Pleistocene climatic variability at astronomical frequencies. Quat. Int. 2, 1–14. https://doi.org/10.1016/1040-6182(89)90016-5

Berger, A., 1988. Milankovitch Theory and climate. Rev. Geophys. 26, 624–657. https://doi.org/10.1029/RG026i004p00624

Berger, A., 1980. The Milankovitch Astronomical Theory of Paleoclimates.

Berger, A., Loutre, M., Dehant, V., 1989. Influence of the changing lunar orbit on the astronomical frequencies of pre-Quaternary insolation patterns. Paleoceanography 4, 555–564.

Berger, A., Loutre, M.F., 1991. Insolation values for the climate of the last 10000000 years. Quat. Sci. Rev. 10, 297–317. https://doi.org/10.1016/0277-3791(91)90033-Q

Berger, A.L., 1978. Long-Term Variations of Daily Insolation and Quaternary Climate

Changes. J. Atmos. Sci. 35, 2362–2367. https://doi.org/10.1175/1520-0469(1978)035<2362:LTVODI>2.0.CO;2
Berger, A.L., 1976. Obliquity and precession for the last 5 000 000 years. Astron. Astrophys. 51, 127–135. https://doi.org/10.1038/269044a0
Bretagnon, P., 1974. Termes à longue périodes dans le système solaire. Astron. Astrophys. 30, 141–154.
Fang, Q., Wu, H., Hinnov, L.A., Jing, X., Wang, X., Jiang, Q., 2015. Geologic evidence for chaotic behavior of the planets and its constraints on the third-order eustatic sequences at the end of the Late Paleozoic Ice Age. Palaeogeogr. Palaeoclimatol. Palaeoecol. 440, 848–859. https://doi.org/10.1016/j.palaeo.2015.10.014
Fang, Q., Wu, H., Hinnov, L.A., Jing, X., Wang, X., Yang, T., Li, H., Zhang, S., 2017. Astronomical cycles of Middle Permian Maokou Formation in South China and their implications for sequence stratigraphy and paleoclimate. Palaeogeogr. Palaeoclimatol. Palaeoecol. 474, 130–139. https://doi.org/10.1016/j.palaeo.2016.07.037
Fang, Q., Wu, H., Wang, X., Yang, T., Li, H., Zhang, S., 2018. Astronomical cycles in the Serpukhovian-Moscovian (Carboniferous) marine sequence, South China and their implications for geochronology and icehouse dynamics. J. Asian Earth Sci. 156, 302–315. https://doi.org/10.1016/j.jseaes.2018.02.001
Fienga, A., Laskar, J., Kuchynka, P., Manche, H., Desvignes, G., Gastineau, M., Cognard, I., Theureau, G., 2011. The INPOP10a planetary ephemeris and its applications in fundamental physics. Celest. Mech. Dyn. Astron. 111, 363–385.
Fienga, A., Laskar, J., Morley, T., Manche, H., Kuchynka, P., Poncin-Lafitte, C. Le, Budnik, F., Gastineau, M., Somenzi, L., 2009. INPOP08, a 4-D planetary ephemeris: From asteroid and time-scale computations to ESA Mars Express and Venus Express contributions. https://doi.org/10.1051/0004-6361/200911755
Fienga, A., Manche, H., Laskar, J., Gastineau, M., 2006. INPOP06: A new planetary ephemeris. Proc. Int. Astron. Union 2, 471. https://doi.org/10.1017/S1743921307011465
Fienga, A., Manche, H., Laskar, J., Gastineau, M., Verma, A., 2014. INPOP new release: INPOP13b. ArXiv e-prints 423.
Folkner, W.M., Williams, J.G., Boggs, D.H., Park, R.S., Kuchynka, P., 2014. The Planetary and Lunar Ephemerides DE430 and DE431, The Interplanetary Network Progress Report.
Gradstein, F.M., Ogg, J.G., Schmitz, M.D., Ogg, G.M., 2012. The Geologic Time Scale 2012. https://doi.org/10.1016/B978-0-444-59425-9.01001-5
Hays, J.D., Imbrie, J., Shackleton, N.J., 1976. Variations in the Earth's Orbit: Pacemaker of the Ice Ages. https://doi.org/10.1126/science.194.4270.1121
Hilgen, F.J., Hinnov, L.A., Abdul Aziz, H., Abels, H.A., Batenburg, S., Bosmans, J.H.C., de Boer, B., Hüsing, S.K., Kuiper, K.F., Lourens, L.J., Rivera, T., Tuenter, E., Van de Wal, R.S.W., Wotzlaw, J.-F., Zeeden, C., 2015. Stratigraphic continuity and fragmentary sedimentation: the success of cyclostratigraphy as

part of integrated stratigraphy. Geol. Soc. London, Spec. Publ. 404, 157–197. https://doi.org/10.1144/SP404.12
Hilgen, F.J., Lourens, L.J., Van Dam, J.A., Beu, A.G., Boyes, A.F., Cooper, R.A., Krijgsman, W., Ogg, J.G., Piller, W.E., Wilson, D.S., 2012. The Neogene Period, The Geologic Time Scale 2012. Elsevier. https://doi.org/10.1016/B978-0-444-59425-9.00029-9
Hinnov, L.A., 2018. Cyclostratigraphy and Astrochronology in 2018, Stratigraphy & Timescales. Elsevier Ltd. https://doi.org/10.1016/bs.sats.2018.08.004
Hinnov, L.A., 2013. Cyclostratigraphy and its revolutionizing applications in the earth and planetary sciences. Bull. Geol. Soc. Am. 125, 1703–1734. https://doi.org/10.1130/B30934.1
Hinnov, L.A., 2000. New Perspectives on orbitally forced Stratigraphy 12, 727–732. https://doi.org/10.1177/0741713604268894
Hinnov, L.A., Hilgen, F.J., 2012. Cyclostratigraphy and Astrochronology. Geol. Time Scale 2012 1–2, 63–83. https://doi.org/10.1016/B978-0-444-59425-9.00004-4
Imbrie, J., Boyle, I.E. a, Clemens, S.C., Duffy, A., Howard, I.W.R., Kukla, G., Kutzbach, J., Martinson, D.G., Mclntyre, A., Mix, A.C., Molfino, B., Morley, J.J., Pisias, N.G., Prell, W.L., Peterson, L.C., Toggweiler, J.R., 1993. On the Structure and Origin of Major Glacial Cycles. Paleoceanography 8, 699–735. https://doi.org/10.1029/93pa02751
Lambeck, K., 1980. The Earth's Variable Rotation: Geophysical Causes and Consequences. Cambridge Univ. Press. https://doi.org/doi.org/10.1017/S0016756800025929
Laskar, J., 2015. Stability of the Solar System. Scolarpedia.
Laskar, J., 2003. Frequency map analysis and quasiperiodic decompositions. https://doi.org/10.1109/PAC.2003.1288929
Laskar, J., 1999. The limits of Earth orbital calculations for geological time-scale use. Philos. Trans. R. Soc. A Math. Phys. Eng. Sci. 357, 1735–1759. https://doi.org/10.1098/rsta.1999.0399
Laskar, J., 1993. Frequency analysis for multi-dimensional systems. Global dynamics and diffusion. Phys. D Nonlinear Phenom. Vol. 67, Issues 1–3, 15 August 1993, Pages 257-281 67, 257–281. https://doi.org/https://doi.org/10.1016/0167-2789(93)90210-R
Laskar, J., 1990. The chaotic motion of the solar system: A numerical estimate of the size of the chaotic zones. Icarus 88, 266–291. https://doi.org/10.1016/0019-1035(90)90084-M
Laskar, J., Fienga, A., Gastineau, M., Manche, H., 2011a. La2010: A new orbital solution for the long term motion of the Earth 4. https://doi.org/10.1051/0004-6361/201116836
Laskar, J., Gastineau, M., Delisle, J.-B., Farrés, A., Fienga, A., 2011b. Strong chaos induced by close encounters with Ceres and Vesta. Astron. Astrophys. 532, L4. https://doi.org/10.1051/0004-6361/201117504
Laskar, J., Joutel, F., Boudin, F., 1993. Orbital, precessional, and insolation

quantities for the Earth from -20 Myr to + 10 Myr. Astron. Astrophys. (ISSN 0004-6361), vol. 270, no. 1-2, p. 522-533.
Laskar, J., Robutel, P., Joutel, F., Gastineau, M., Correia, A.C.M., Levrard, B., 2004. A long-term numerical solution for the insolation quantities of the Earth. Astron. Astrophys. 428, 261–285. https://doi.org/10.1051/0004-6361:20041335
Ma, C., Meyers, S.R., Sageman, B.B., 2019. Testing Late Cretaceous astronomical solutions in a 15 million year astrochronologic record from North America. Earth Planet. Sci. Lett. 513, 1–11. https://doi.org/10.1016/j.epsl.2019.01.053
Meyers, S.R., Sageman, B.B., Arthur, M.A., 2012a. Obliquity forcing of organic matter accumulation during Oceanic Anoxic Event 2. Paleoceanography 27, 1–19. https://doi.org/10.1029/2012PA002286
Meyers, S.R., Siewert, S.E., Singer, B.S., Sageman, B.B., Condon, D.J., Obradovich, J.D., Jicha, B.R., Sawyer, D.A., 2012b. Intercalibration of radioisotopic and astrochronologic time scales for the Cenomanian-Turonian boundary interval, western interior Basin, USA. Geology 40, 7–10. https://doi.org/10.1130/G32261.1
Milanković, M., 1941. Kanon der Erdbestrahlung und seine Anwendung auf das Eiszeitenproblem. R. Serbian Sci, Académie royale serbe. Éditions speciales 33.
Olsen, P.E., Laskar, J., Kent, D. V., Kinney, S.T., Reynolds, D.J., Sha, J., Whiteside, J.H., 2019. Mapping Solar System chaos with the Geological Orrery. Proc. Natl. Acad. Sci. 201813901. https://doi.org/10.1073/PNAS.1813901116
Pälike, H., 2005. Orbital Variation (Including Milankovitch Cycles). Encycl. Geol. 410, 410–421. https://doi.org/10.1016/B0-12-369396-9/00123-4
Pälike, H., Frazier, J., Zachos, J.C., 2006. Extended orbitally forced palaeoclimatic records from the equatorial Atlantic Ceara Rise. Quat. Sci. Rev. 25, 3138–3149. https://doi.org/10.1016/j.quascirev.2006.02.011
Papaphilippou, Y., 1999. Frequency maps of LHC models. Proc. 1999 Part. Accel. Conf. (Cat. No.99CH36366) 3, 1554–1556. https://doi.org/10.1109/PAC.1999.794171
Quinn, T.R., Tremaine, S., Duncan, M., 1991. A three million year integration of the earth’s orbit. Astron. J. 101, 2287–2305. https://doi.org/10.1086/115850
Shackleton, N.J., Crowhurst, S.J., Weedon, G.P., Laskar, J., 1999. Astronomical calibration ofOligocene-Miocene time. R. Soc. London Philos. Trans. 357, 1907–1929.
Shackleton, N.J., Hagelberg, T., Crowhurst, S.J., 1995. Evaluating the success of astronomical tuning: Pitfalls of using coherence as a criterion for assessing pre-Pleistocene timescales. Paleoceanography 10, 693–697. https://doi.org/10.1029/95PA01454
Souami, D., Souchay, J., 2012. The solar system’s invariable plane. Astron. Astrophys. 543, A133. https://doi.org/10.1051/0004-6361/201219011
Standish, E.M., 1998. JPL Planetary and Lunar Ephemerides, DE405/LE405. Jet Propuls. Lab. Interoffice Memo. IOM 312.F.
Thomson, D.J., 1982. Spectrum Estimation and Harmonic Analysis 70.

Valluri, M., Merritt, D., 1998. Regular and Chaotic Dynamics of Triaxial Stellar Systems. Astrophys. J. 506, 686–711. https://doi.org/10.1086/306269
Varadi, F., Runnegar, B., Ghil, M., 2003. Successive Refinements in Long-Term Integrations of Planetary Orbits. Am. Astron. Soc. 592, 620–630.
Westerhold, T., Röhl, U., Frederichs, T., Agnini, C., Raffi, I., Zachos, J.C., Wilkens, R.H., 2017. Astronomical Calibration of the Ypresian Time Scale: Implications for Seafloor Spreading Rates and the Chaotic Behaviour of the Solar System? Clim. Past Discuss. 1–34. https://doi.org/10.5194/cp-2017-15
Westerhold, T., Röhl, U., Laskar, J., 2012. Time scale controversy: Accurate orbital calibration of the early Paleogene. Geochemistry, Geophys. Geosystems 13, 1–19. https://doi.org/10.1029/2012GC004096
Wu, H., Fang, Q., Wang, X., Hinnov, L.A., Qi, Y., Shen, S., Yang, T., Li, H., Chen, J., Zhang, S., 2018. An ~34 m.y. astronomical time scale for the uppermost Mississippian through Pennsylvanian of the Carboniferous System of the Paleo-Tethyan realm. Geology 47, 83–86. https://doi.org/10.1130/g45461.1
Zeebe, R.E., 2017. Numerical Solutions for the orbital motion of the Solar System over the Past 100 Myr: Limits and new results. Astron. J. 154, 193. https://doi.org/10.3847/1538-3881/aa8cce
Zeeden, C., Hilgen, F.J., Hüsing, S.K., Lourens, L.L., 2014. The Miocene astronomical time scale 9-12-Ma: New constraints on tidal dissipation and their implications for paleoclimatic investigations. Paleoceanography 29, 296–307. https://doi.org/10.1002/2014PA002615
Zeeden, C., Kaboth, S., Hilgen, F.J., Laskar, J., 2018. Taner filter settings and automatic correlation optimisation for cyclostratigraphic studies. Comput. Geosci. 119, 18–28. https://doi.org/10.1016/j.cageo.2018.06.005
Zeeden, C., Meyers, S.R., Lourens, L.J., Hilgen, F.J., 2015. Testing astronomically tuned age models. Paleoceanography 30, 369–383. https://doi.org/10.1002/2014PA002762

Chapter 2

Detecting chaotic transitions in geological time series: Applying improved methodologies

Melanie Reinelt[1], Christian Zeeden[2], Heiko Pälike[1]

[1]MARUM - Center for Marine Environmental Sciences, University of Bremen, Leobener Str. 8, 28359 Bremen, Germany
[2]LIAG - Leibniz Institute for Applied Geophysics, GEOZENTRUM HANNOVER, Stilleweg 2, 30655 Hannover

Abstract

Astrochronology is an important tool for developing geological age models, and is part of numerous integrated stratigraphic studies. Such age models are often adjusted to astronomical solutions, which are based on the numerical integration of modern (initial) conditions of the solar system back in time. Due to the chaotic behaviour of the solar system, the duration over which Earth's orbital variations can be computed with confidence is limited. In this context it is thus relevant to detect chaotic transitions in geological data, in order to verify and extend astronomical models. One manifestation of astronomical chaos is the change of two resonant fundamental frequencies of Mars' and Earth's orbit. ~100 kyr eccentricity and obliquity amplitude modulation can provide 'fingerprints' of these transitions.

Here, we develop and test several methods for detecting such transitions in geological data. For this, we use different astronomical solutions partly including auto-regressive noise, and we re-investigate one Paleogene dataset. The major difference of this approach to previous studies is that we combine complex frequency analyses with traditional amplitude modulation of eccentricity and obliquity. We filter 2.4 and 1.2 Myr cycles from data, and require an increase in amplitude of the 1.2 Myr cycle and a decreasing 2.4 Myr amplitude during a chaotic transition. Applying this approach, we confirm a proposed transition in ODP material of Site 1258 at ~ 52 Ma.

2.1. Introduction

Quasi-periodic variations in the orientation of Earth's orbit around the sun - Milankovitch cycles - influence incoming solar radiation (insolation) and climate-sensitive processes in Earth history. These astronomically driven cycles are recorded in various sedimentary archives and became an important part of integrated stratigraphy (e.g. Hays, Imbrie, & Shackleton, 1976; Hinnov, 2013, Hilgen et al., 2015). Age models based on cyclostratigraphy are often directly correlated to theoretical astronomical models. As these astronomical solutions are calculated with present (initial) conditions, they are limited due to the chaotic behaviour of the Solar System. Eccentricity is stable back until ~ 50 Ma (Laskar et al., 2011a; Zeebe, 2017), but further back in time only the frequency (and not the amplitude modulation) of the 405 kyr eccentricity cycle remains stable. Its phase is rather constant until ~200 Ma, but its presence can be used further back in time for reconstructing relative time scales (Hilgen et al., 2015).

The Earth's orbit is affected by motions of other planets:
The position of an orbit and the position of a body in an orbit is represented by Keplerian elements: ***a***, ***b***, ***i***, λ, ω, Ω, where ***a*** is the semi-major and ***b*** the semi-minor axis of the orbital ellipse, ***e*** the eccentricity of the ellipse, ***i*** is the inclination describing the angle between the orbital and the reference plane. The longitude of the ascending node **N** is described by the angle Ω measured from a fixed position (vernal equinox, γ). The position of the perihelion (closest approach to the sun) P and its motion $\tilde{\omega}$ is defined by $\tilde{\omega} = \Omega + \omega$ (longitude of the perihelion) (Berger, 1980, 1988; Berger and Loutre, 1991; Pälike, 2005).
The individual frequencies of each considered major body of the Solar System
(i = 1,…,8: 1. Mercury, 2. Venus, 3. Earth, 4. Mars, 5. Jupiter, 6. Saturn, 7. Uranus and 8. Neptune) are combined in the terms $\mathbf{g_i}$ and $\mathbf{s_i}$. The frequencies g_i refer to the orbital elements ***e*** (eccentricity) and ω (longitude of the perihelion) and describe the variation of a body within its orbit whereas s_i is related to ***i*** (inclination) and Ω (longitude of the ascending node) and describe the orientation of the orbital plane itself.
A combination of fundamental g_i and s_i frequency terms leads to different beats; the relevant periods of eccentricity and obliquity for this study are given in Table 2.1.

Table 2.1. Leading frequency components for long (~405 kyr) and short (~100 kyr) eccentricity and obliquity for the last 4 Myr of La93. p is the "constant" of general precession of the Earth (with a recent period of ~ 25.8 kyr) but which itself is influenced over time by.e.g., tidal dissipation. s_i and g_i are Eigenmodes that refer to corresponding planets (see text). Relevant amplitude modulation terms for eccentricity and obliquity from interfering terms to "beat" terms with periods.

Term	Frequency ("/year)	Period (kyr)	Type	Interfering term	Beat term	Period (Myr)
g_2-g_5	3.1996	406.182	~405 kyr and ~100 kyr eccentricity amplitude modulation terms	$(g_4 - g_5) - (g_3 - g_5)$ $(g_4 - g_2) - (g_3 - g_2)$	$(g_4 - g_3)$	2.4
g_4-g_5	13.6665	94.83				
g_4-g_2	10.4615	123.882				
g_3-g_5	13.143	98.607				
g_3-g_2	9.9677	130.019				
$p+s_3$	31.613	40.996	obliquity amplitude modulation terms	$(p + s_3) – (p + s_4)$	$(s_4 – s_3)$	1.2
$p+s_4$	32.68	39.657		$(p + s_3 + g_4 - g_3)$ $- (p + s_3 - g_4 + g_3)$	$2(g_4 - g_3)$	1.2
$(p+s_3+g_4-g_3)$	32.183	40.27				
$p+s_6$	24.128	53.714				
$(p+s_3-g_4+g_3)$	31.098	41.647		$(p + s_3) - (p + s_3 + g_4 - g_3)$	$(g_4 - g_3)$	2.4
$p+s_1$	44.861	28.889		$(p + s_3) - (p + s_3 - g_4 + g_3)$		

Such amplitude (and frequency) modulations of Earth's eccentricity, obliquity and climatic precession variations produce "beats" with longer periods. These modulations can be used to 'fingerprint' particular astronomical signals, and extract particular components from geological data (Meyers, 2019, 2015; Pälike et al., 2004; Shackleton et al., 1995; Zeeden et al., 2015). Important amplitude modulation terms for short eccentricity and obliquity are outlined in Table 2.1 (see Hinnov, 2000).

2.1.1. Chaotic behaviour of the solar system

In 1990, Laskar discovered the chaotic behaviour of the solar system due to the gravitational interactions of the bodies in the solar system. These dynamics are not fixed and it is theoretically impossible to predict the movements from their current position, masses and velocities (Laskar, 1990). The calculation of the orbit diverges exponentially with time. For example, the current position of a planet is known with a relative error of ~10^{-10}, this error increases to ~10^{-9} after 10 Myr, and reaches the order

of 1 after 100 Myr (Jacques Laskar, 1999). This fact limits the use of astronomical models for creating astronomically calibrated geological time scales (Laskar, 2003).
The chaotic motion of the solar system manifests itself in resonance changes of eccentricity and obliquity amplitude modulation terms. A combination of fundamental frequencies of Mars' and Earth's orbit expressed in $(g_4 - g_3) - 2(s_4 - s_3)$ oscillate at present at 0, like a pendulum. This system is called to be in libration. But this motion does not persist and can evolve into a new state, into circular and even more into libration motion. During the circular motion, the expression $(g_4 - g_3) - 2(s_4 - s_3) = 0$ changes into $(g_4 - g_3) - (s_4 - s_3) = 0$. This implies a change from a 2:1 resonance into a 1:1 (Laskar, 1999). The result is a missing $(g_4 - g_3)$ frequency term in obliquity, and in eccentricity the expression $g_4 – g_3$ changes into $2(g_4 - g_3)$ (Table 2.1).

To verify and extend theoretical astronomical models, it is important to detect astronomical chaos in the geological record, initially implemented by Pälike et al. (2004). This has received increased attention recently (Fang et al., 2015; Ma et al., 2019, 2017; Westerhold et al., 2017). Before being able to detect these chaotic transitions, it is necessary to know how similar resonance patterns appear in time series. Time series with well-known positions of resonance switches are best suited for such a test. For this purpose, we developed and test methods with the help of astronomical solutions La2004 and La2010c (Laskar et al., 2004, 2011) by adding auto-regressive (AR1) noise. For solution La2004 some resonance transitions were computed, for example at ~ 58 Ma, ~ 75 Ma and ~ 88 Ma. La2010c was calculated with transitions at ~ 55 Ma, ~ 70 Ma and ~ 86 Ma (see Fig 12, Laskar et al. (2011)). We also investigate the recently published Zb17e solution (Zeebe, 2017). This solution was calculated with the INPOP13c ephemeris, an Earth-Moon gravitation quadrupole and 9 planets (Pluto included) and 10 asteroids. A shift in resonance occur at ~ 54 Ma. This solution includes eccentricity and inclination values for the last 100 Ma. The fundamental frequencies of s_3, s_4, g_3 and g_4 are provided by Earth's orbital inclination in the absence of a detailed Earth orbital model for obliquity.
Motivated by (Pälike et al., 2004) who demonstrated the possibility to differentiate between astronomical solutions (and geological data) that do and do not exhibit chaotic transition(s), we intend to develop a method that can theoretically be applied on any proxy dataset showing a clear imprint of orbital variations. A clear imprint of relevant

orbital variations is especially important for amplitude investigations, because otherwise noise may dominate the outcome (Zeeden et al. 2015). Previous studies dealt with this topic by deciphering resonance transitions from amplitude modulation of eccentricity and obliquity (Fang et al., 2015; Ma et al., 2017; Westerhold et al., 2017). Here, we more thoroughly test several techniques including fundamental and instantaneous frequency analyses, amplitude analyses and their combination for the identification of transitions in geological datasets. We extract 2.4 and (possible) 1.2 Myr cycles from geological data through a combination of filtering and amplitude demodulation. During a chaotic transition, we require a distinct pattern characterised by an increase in amplitude of the 1.2 Myr cycle while the amplitude of the 2.4 Myr cycle falls to zero. We filtered 2.4 Myr cycles between 1/3500 kyr and 1/1800 kyr and 1.2 Myr cycles between 1/1800 kyr and 1/800 kyr (see Table 2.2 and appended R script 'ChaosSearch.R').

Table 2.2 Filter boundaries used in this study

Cycle	Min Frequency (kyr)	Max Frequency (kyr)
~ 405 kyr long eccentricity	1/630	1/280
~100 kyr short eccentricity	1/160	1/85
Obliquity	1/54	1/35
2.4 Myr	1/3500	1/1800
1.2 Myr	1/1800	1/800

2.1.2. Numerical Analysis of Fundamental Frequencies (NAFF)

One way to determine the frequency components of a time series is provided by Laskar's Numerical Analysis of Fundamental Frequencies (NAFF) algorithm. Like Fourier transformation the NAFF is able to convert a quasiperiodic signal into its frequency domain and even more precisely than Fourier transformation.

A quasiperiodic function of time with complex values

$$f(t)=\sum_{k=1}^{\infty} \boldsymbol{a_k} e^{i\nu_k t}$$

is used to find $\boldsymbol{a_k}$ (decreasing amplitudes) and $\boldsymbol{\nu_k}$ (frequencies) in an iterative way. For mathematical principles see Laskar (2003), Laskar (1993), Papaphilippou (1999) and Valluri and Merritt (1998).

A Swift language implementation based on the SDDS (Self Describing Data Sets) Toolkit Version 3.5.1 (Emery et al., 2008) for Fortran is used to perform NAFF (hpNAFF source code: https://paloz.marum.de/confluence/display/ESPUBLIC/NAFF).

From a definite window the application calculates a list of all fundamental frequency terms by using a moving window approach with a window size of 3000 kyr in steps of 100 kyr. Each window was detrended by polynomial regression (here order of 2). The application of this algorithm results in a list containing the columns frequency, amplitude, phase, significance and period, starting from t0 of each window and is sorted within the windows by decreasing amplitude.

Short eccentricity amplitude modulation terms $(g_4 - g_5) - (g_3 - g_5)$ and $(g_4 - g_2) - (g_3 - g_2)$ result in a period of 2.4 Myr $(g_4 - g_3)$ or, during a resonance transition, in ~ 1.2 Myr $(2(g_4 - g_3))$ (Laskar, 1999). In obliquity amplitude modulation, the terms $(p + s_3) - (p + s_3 + g_4 - g_3)$ (40.27 kyr) and $(p + s_3) - (p + s_3 - g_4 + g_3)$ (41.647 kyr) result in a beat term of $(g_4 - g_3)$ (2.4 Myr). This component does not exist during transitions, whereas $p + s_3$ (40.996 kyr) and $p + s_4$ (39.657 kyr), producing the beat term $(s_4 – s_3)$ (1.2 Myr), remain (Hinnov, 2013, 2000; Laskar, 1990).

The relevant fundamental frequency terms for obliquity are $p + s_3$ and $p + s_4$, $(p + s_3 + g_4 - g_3)$ and $(p + s_3 - g_4 + g_3)$, all between 1/39 and 1/41 kyr (or 31 – 32 arcseconds/year; see Table 2.1). In order to calculate relevant amplitude modulation terms, it is crucial to distinguish between the terms $p + s_3$ and $p + s_4$, $p + s_3 + g_4 - g_3$ and $p + s_3 - g_4 + g_3$, which is difficult due to similar frequencies and could lead to misinterpretation.

For inclination, the frequencies s_3, s_4, g_3 and g_4 were filtered between 65 and 77 kyr. These values are also rather close to each other and therefore difficult to distinguish in order to create frequency terms and perform calculations (s_3 ~ 68.7 kyr, s_4 ~ 72.9 kyr, g_3 ~ 74.6 kyr, g_4 ~ 72.3 kyr, see Table 6, Laskar et al., 2011). For this purpose, the frequency analyses were only being conducted on short eccentricity amplitude modulation for all datasets.

It is possible to either analyse the short eccentricity signal and calculate $(g_4 – g_3)$ (or $2(g_4 - g_3)$) from the fundamental frequency terms $(g_4 - g_5) - (g_3 - g_5)$ and $(g_4 - g_2) - (g_3 - g_2)$, or by extracting $(g_4 – g_3)$ (or $2(g_4 - g_3)$) from already demodulated short eccentricity as input.

2.1.3. Amplitude- and frequency analyses

Hilbert transformation extracts instantaneous frequency, amplitude and phase of a signal. From a time dependent amplitude A(t) and a time-dependent phase Θ(t) of a signal $f(t) = A(t)\, cos\, \theta(t)$, the time-dependent (instantaneous) frequency ω(t) is calculated by the rate of change of the time-dependent phase. $\omega(t) = \frac{d\theta(t)}{dt}$ (Hinnov et al., 2002; Taner et al., 1979; Vakman, 1996). We calculated instantaneous frequencies from the amplitude envelope of short (~ 100 kyr) eccentricity. This is done to compare the NAFF results with instantaneous frequencies and to test the suitability of both techniques for extracting information on chaotic transitions. The frequency range we focus on only includes possible resonance changes from 2.4 to 1.2 Myr. For this purpose, we filtered short eccentricity amplitude modulation between 1/3500 kyr and 1/800 kyr (see Table 2.2).

2.2. Testing and developing methods

In this section we test methods on several datasets. We describe the experiments and results and directly discuss which approaches are useful and where issues lie.

2.2.1. Testing filter settings for reconstructing relevant astronomical components

Except in few studies (Li et al. , 2018; Zeeden et al., 2018) filter settings for astrochronological studies are quite arbitrary chosen. Here we tested different Taner filter settings for extracting ~ 2.4 Ma eccentricity components from noisy data. The R programming language (R Development Core Team, 2016) was used, together with the 'astrochron' package

For this test, we used the last 15 Ma of the La2004 solution (Laskar et al., 2004) as template, from which we create an ETP curve, consisting of equal parts of standardised **e**ccentricity, **t**ilt/obliquity and **p**recession, by subtracting their individual means, dividing by their standard deviation, and adding these three components. This data set has a standard deviation of 1.7. We added auto-regressive noise (AR1 noise, depending on the previous data point) with rho=0.8, and a standard deviation of 0.5. The data set was tested against the ~ 2.4 Myr eccentricity component extracted from the 100 kyr signal.

Taner filter settings of lower cut-off frequency and upper cut-off frequency were tested in ranges from 1/50 to 1/100 and 1/105 to 1/200 [1/ kyr] in steps of 1/5, respectively. In addition, we tested the effect of changing roll-off rate (see R script in supplementary information A1 section 1 for details). Numerous filter settings gave similar good results with Pearson R^2 (Pearson, 1895) of > 0.98 between the record reconstructed from eccentricity and noisy ETP, see Supplementary Figures A1 – A4.

We chose to analyse 15 Ma of data here, in order to contain at least several 2.4 Myr eccentricity cycles. Datasets of this length can be expected to show changes in eccentricity filters due to chaotic transitions. When investigating much longer datasets, this may be suppressed due to the fact that a filter will be dominated by the dominant long eccentricity. For such long datasets, filters may not react to deviations from the mean cyclicity.

The identified most suitable roll-off rate of 10^{10} was identified for long eccentricity and obliquity filtering. In different tests, regarding the important frequencies for obliquity and long eccentricity (see discussion), we determined useful upper and lower frequencies for Taner filtering, as follows: long eccentricity is filtered between 1/630 and 1/280 kyr, short eccentricity between 1/160 and 1/85 kyr and obliquity between 1/54 and 1/35 kyr. For further amplitude investigations, we filtered 2.4 Myr cycles between 1/3500 kyr and 1/1800 kyr and 1.2 Myr cycles between 1/1800 kyr and 1/800 kyr. These filter boundaries were chosen based on experience after filtering 2.4 and 1.2 Myr cycles manually.

2.2.2. Method testing using astronomical solution La2004

To develop and test methods for detecting chaotic transitions, we initially used the La2004 solution (Laskar et al., 2004). We aim to discover distinctive transition intervals by several methods of data analyses: fundamental (NAFF) and instantaneous frequency, and filtering of datasets and their eccentricity and obliquity components.

2.2.2.1. Instantaneous Frequency and NAFF of La2004, 0 – 100 Ma

At first, we performed two different techniques of frequency analyses: fundamental (NAFF) and instantaneous frequency analyses (Figure 2.1).

From a normalized ETP curve of La2004 of the last 100 Ma, we extracted and demodulated short eccentricity by Hilbert transformation. To focus only on relevant

frequencies, we filtered the ~ 100 kyr amplitude modulation between 1/3500 kyr and 1/800 kyr (see filter settings in Table 2.2). Then we performed NAFF in steps of 100 kyr with a window size of 3000 kyr. From each moving window, a polynomial regression with order of 2 was subtracted before computing fundamental frequencies. The instantaneous frequencies were calculated with a time step of 1 kyr. Distinct resonance shifts can be deducted from switches of periods between ~ 2.4 and ~ 1.2 Myr (dashed lines in Figure 2.1) at ~ 57 Ma, ~ 78 Ma and ~ 88 Ma (arrows), although the ones at ~ 57 Ma and ~78 Ma are not particularly obvious. The sharp peak in frequency at ~ 32 Ma is an artefact of a low amplitude and does not indicate a chaotic transition (see Supplementary Figure A6). Next, we focus on the intervals between 50 - 65 Ma and 80 - 95 for further amplitude and filter analyses.

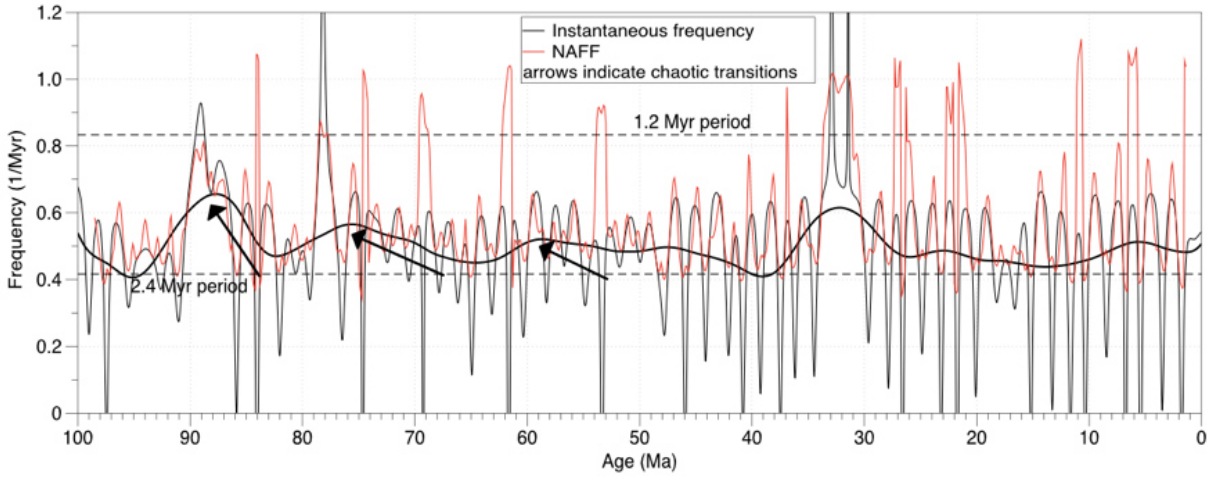

Figure 2.1. Frequency analyses of the last 100 Myr of La2004, applied on short eccentricity amplitude modulation. Fundamental frequency analyses (NAFF) showing (g_4 - g_3) or 2(g_4 - g_3) frequencies (1/Myr; red). Instantaneous frequencies (1/Myr; red). (black) with LOESS (LOcally Estimated Scatterplot Smoothing) trend line. Resonance shifts from ~ 2.4 Myr to ~ 1.2 Myr are indicated at ~ 58 Ma, ~ 75 Ma and ~ 88 Ma (arrows). All transitions show a switch back into ~ 2.4 Myr soon afterwards. Dashed lines mark 2.4 Myr and 1.2 Myr periods. The sharp peak in frequency at ~ 32 Ma is an effect of a zero amplitude. This is no indication for a transition (see Supplementary Figure A6).

2.2.2.2. Amplitude analyses of La2004, focus on transitions around 50 – 65 and 80 – 95 Ma

By filtering 2.4 and 1.2 Myr periods from amplitude modulation of long and short eccentricity and obliquity, we want to determine the position of chaotic transitions by identifying a missing 2.4 Myr cyclicity.

We used ETP (Eccentricity + 0.5 * Tilt – Precession) data of La2004 between 50 and 65 Ma and 80 – 95 Ma with eccentricity, obliquity and a standard deviation of 1.730. Evolutive harmonic analyses (EHA) of the two time intervals were performed using the 'eha' function provided in the "astrochron" package (Meyers, 2014) with a time step of 1 kyr and a window size of 500 kyr, padded to 5000 data points. A linear trend and mean value were removed from each window before analysis.

From each interval we extracted short and long eccentricity and obliquity by Taner band-pass filtering with a roll-off rate of 10^{10} (Taner et al., 1979). For filter settings see Table 2.2 (and R-Script ChaosSearch.R in supplementary material). Hilbert transformation was used to calculate the instantaneous amplitude modulation of each cycle. The output of essential periods of the Taner band-pass filters in the amplitude modulation could now reveal indications for a resonance shift from a 2.4 to a 1.2 Myr period. During a resonance transition, long and short eccentricity amplitude modulation should express the change of $g_4 – g_3$ into $2(g_4 - g_3)$, but with an opposite phase, as we demodulated direct ~ 405 kyr eccentricity and ~ 100 kyr eccentricity filters. In order to achieve a stronger signal-to-noise ratio, we combined these two amplitude modulations by subtracting long eccentricity amplitude from short eccentricity amplitude, which leads to an amplification of the signal (see Figure 2.2, 'combined eccentricity AM'). In obliquity, the expression $g_4 – g_3$ should be missing during transitions, while the $s_4 - s_3$ term remains. Due to the phase shift between obliquity and eccentricity (Hinnov, 2013), the exact timing of the resonance transition differs, when extracted from eccentricity or obliquity amplitude. Figure 2.2 presents the results of amplitude analyses: 2.4 and 1.2 Myr cycles could be detected in the amplitude modulation of all cycles and in the combined amplitude modulation of short and long eccentricity (in Figure: i, j). During ~ 87 – 90 Ma and ~ 56 – 59 Ma (highlighted with red boxes), the cyclicity changes from a 2.4 Myr to a 1.2 Myr period in all cycles. We can thus detect the chaotic intervals around ~ 58 and ~ 88 Ma.

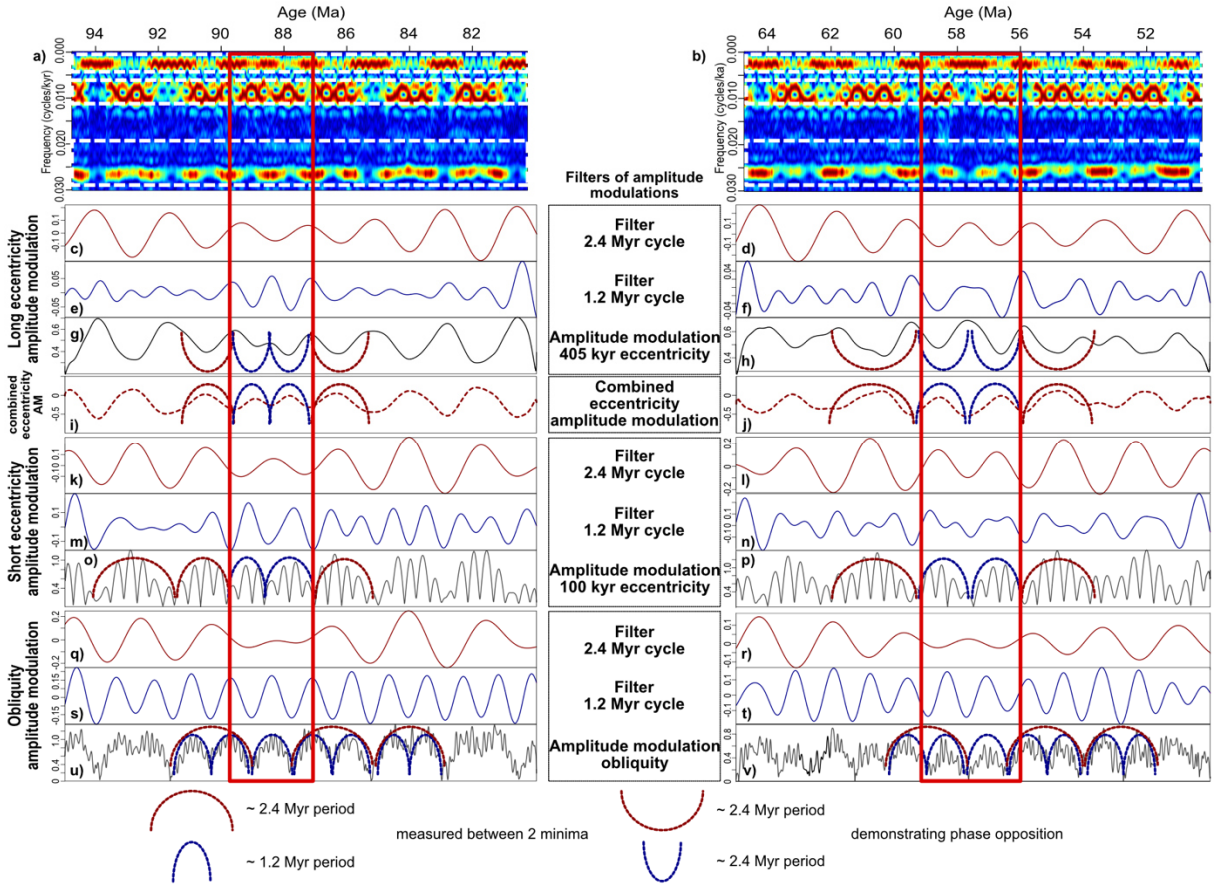

Figure 2.2. Amplitude analyses of La2004 between 95 - 80 Ma (left) and 65 - 50 Ma (right). Evolutive harmonic analyses (EHA) results are displayed in the top panels (a, b). Dashed boxes in a) and b) indicate the filtered cycles (long and short eccentricity and obliquity). Panels below show from top to bottom: Filters of long eccentricity amplitude modulation (g, h), the combined amplitude modulation of short and long eccentricity (i, j), short eccentricity (o, p) and obliquity (u, v) amplitude modulation together with filtered 1.2 Myr (dark blue: e, f, m, n, s, t) and 2.4 Myr (dark red: c, d, k, l, q, r) cycles from each amplitude modulation. In amplitude modulation (g, h, o, p, u, and v) and in combined filter (i, j) some recognizable periods of 2.4 (dark red) and 1.2 Myr (dark blue) are highlighted within red boxes. These also illustrate the phase opposition of long and short eccentricity. In resonance transitions, 2.4 Myr periods change into 1.2 Myr periods in eccentricity or disappear in obliquity. The identified chaotic intervals are at ~ 58 and ~ 88 Ma.

The initial test of different methods on a clean (non-noisy) data set consisting of long and short eccentricity and obliquity was successful (as expected). The resonance transitions detected in frequency agree with those in amplitude and filter analyses. They could be identified exactly where they were predicted in La2004.

This experiment demonstrates that care has to be taken when interpreting frequency analyses alone, because low amplitudes result in artefacts which can lead to misinterpretation of a chaotic transition. Further, not all transitions show a similar change in frequency analyses. From this experiment we conclude that amplitude modulation of an eccentricity signal comprising both the ~ 100 and ~ 405 kyr components indicates a shift from a 2.4 Myr to a 1.2 Myr period best.
In the next steps, we tested the methods on data sets without an obliquity contribution.

2.2.3. Testing the method, Analysis of Zb17e

To test the previous approach, we used the Zb17e – solution (Zeebe, 2017) consisting of eccentricity and **inclination** and a time step of Δ**t = 1.6** kyr. The Zb17e solution was treated differently because no obliquity but inclination is available.

2.2.3.1. Instantaneous Frequency and NAFF of Zb17e, 0 – 100 Ma

For frequency analyses, we extracted short eccentricity, demodulated it by Hilbert transformation and filtered between 1/3500 kyr and 1/800 kyr. The instantaneous frequencies were calculated in steps of 1.6 kyr, and NAFF was applied every 160 kyr (a multiple of 1.6 kyr), with a window size of 3000 kyr. Each window was detrended by polynomial regression with order of 2 (Figure 2.3). A distinct period switch from ~ 2.4 to ~ 1.2 Myr (dashed lines in Figure) was calculated at ~ 55 Ma (arrow). Some other frequency peaks (e. g. at ~ 43 and ~ 93 Ma) are artefacts of low amplitudes where frequencies cannot be determined with confidence (see Supplementary Figure A7). The interval between 47 and 62 Ma was analysed for further amplitude and filter analyses.

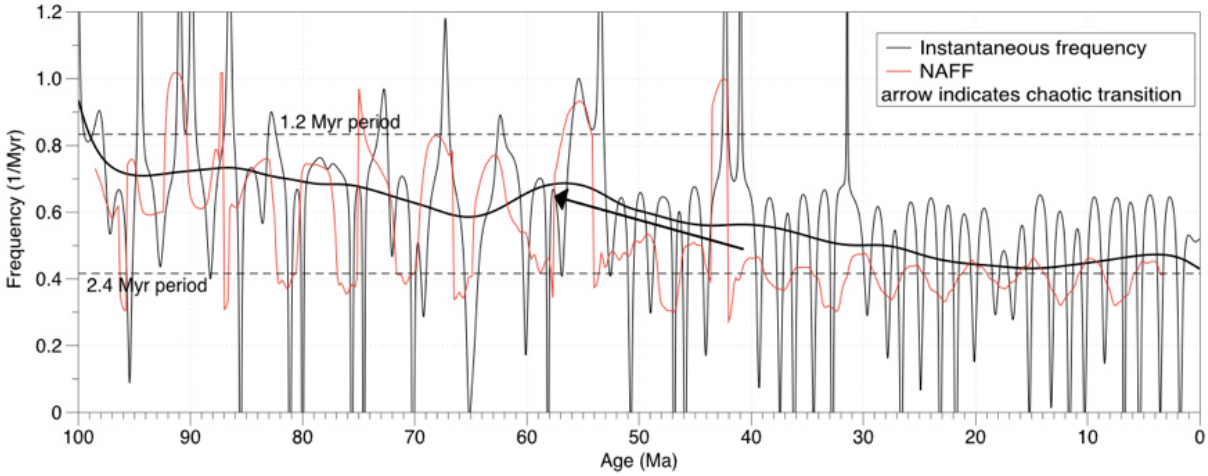

Figure 2.3. Frequency analyses of Zb17e of the last 100 Myr, applied on short eccentricity amplitude modulation. Fundamental frequency analyses (NAFF) showing (g_4- g_3) or 2(g_4 - g_3) frequencies (1/ Myr: red). Instantaneous frequencies (1/Myr: black) with LOESS (LOcally Estimated Scatterplot Smoothing) trend line. Dashed lines mark 2.4 Myr and 1.2 Myr periods. Frequencies analyses calculated a distinct resonance shift from ~ 2.4 Myr to ~ 1.2 Myr at ~ 55 Ma (black arrow) and remain at ~ 1.6 Myr afterwards. Several peaks (e. g. at ~ 43 and ~ 93 Ma) in frequency are artefacts of low amplitudes (see Supplementary Figure 7).

2.2.3.2. Amplitude analyses and filtering Zb17e, 47 – 62 Ma

Short eccentricity was filtered and demodulated as before, but as inclination includes the fundamental frequencies of s_3, s_4, g_3 and g_4, these were filtered together between 65 kyr and 76 kyr and demodulated by Hilbert transformation. EHA from 0 – 0.03 cycles/kyr with a window size of 500 kyr and a step of 1 kyr padded to 5000 data points for each eccentricity and inclination was applied. 2.4 and 1.2 Myr cycles were filtered for amplitude investigations, and to achieve an amplification of the signal, short and long eccentricity amplitude modulation were combined. We used the R script 'ChaosSearch.R' (supplementary material) for filtering. In Figure 2.4 we present the results of amplitude and filter analyses: 2.4 and 1.2 Myr periods could be recognized within the amplitude modulation of short (i), long eccentricity (e) and inclination (I). Also apparent is the low 2.4 Myr amplitude in contrast to a high 1.2 Myr amplitude in filtered cycles (highlighted with red box). As during resonance transitions the 2.4 Myr cyclicity disappears and the 1.2 Myr period remains, we could identify a chaotic interval around ~ 55 Ma.

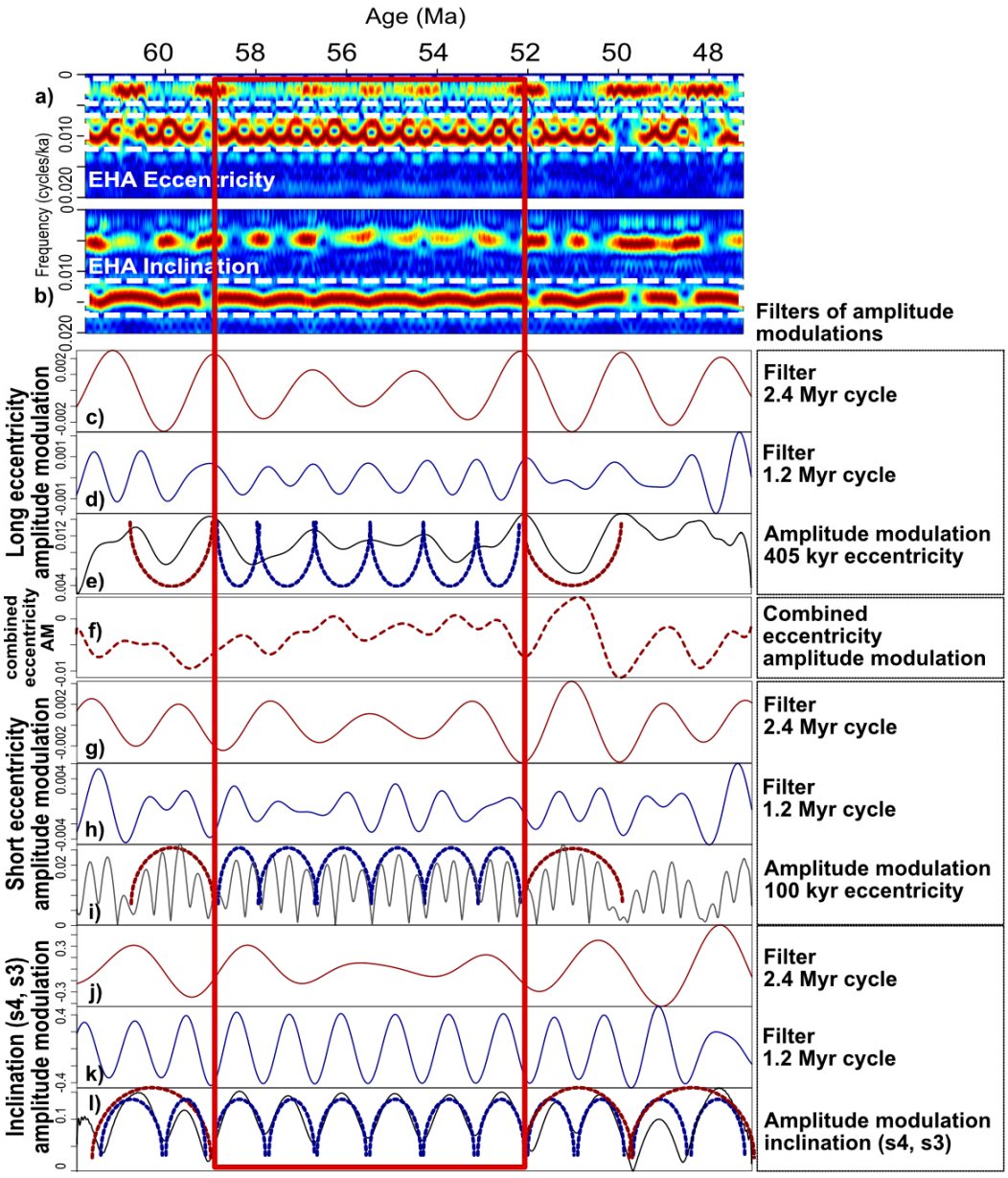

Figure 2.4. Amplitude Analyses of Zb17e between 47 and 62 Ma. Top panel: EHA of eccentricity (a) and inclination (b). Dashed boxes in a) and b) indicate the filtered cycles: long eccentricity, short eccentricity and filter of s_3, s_4, g_3 and g_4 between 65 and 77 kyr in inclination. Panels below show from top to bottom: Filters of long eccentricity amplitude modulation (e), the combined short and long eccentricity amplitude (f), short eccentricity (i) and inclination (i) amplitude modulation together with filtered 1.2 Myr (dark blue: d, h, k) and 2.4 Myr (dark red: c, g, j) of each amplitude modulation for amplitude comparisons. In amplitude modulation some recognizable 2.4 (darkred) and 1.2 Myr (darkblue) periods are highlighted within the red box. These also illustrate the phase opposition of long and short eccentricity. See legend of Figure 2.2 for details. As during a resonance transition only the 1.2 Myr period remains, we could identify a chaotic interval at ~ 55 Ma.

The second test was conducted on a non-noisy data set consisting of eccentricity and inclination (Zeebe, 2017). As inclination provides the fundamental frequencies s_3, s_4, g_3 and g_4, similar to obliquity, we could use inclination instead. Frequency analyses calculated the resonance transition exactly where it was calculated in Zb17e (at ~ 55 Ma; Figure 2.3), which agree with those detected in amplitude and filter analyses (Figure 2.4). Some jumps in frequencies are consequences of low amplitudes and could lead to misinterpretation and should always be considered during interpretations. For amplitude and filter analyses, we conclude that the test on inclination was successful, as it indicates a shift from a 2.4 Myr to a 1.2 Myr periodicity perfectly.
After we developed and tested the approach on undisturbed astronomical solutions with and without obliquity (inclination instead), we investigated a solution with additional noise in order to be prepared for applying the method on “real” geological data.

2.2.4. Analysis of a more realistic data set: La2010c with noise

The data set consisting of eccentricity with a standard deviation of 0.013 was modified by adding equally strong (same standard deviation) auto-regressive noise (AR1 surrogates) (Meyers, 2012) with rho=0.9 in order to simulate somewhat more realistic geologic data. Please note that here the time axis is still perfect, which will not be the case for geological data.

2.2.4.1. Instantaneous Frequency and NAFF of La2010c with noise, 0 - 100 Ma

Frequency analyses were applied on the demodulated short eccentricity and relevant frequencies between 1/3500 kyr and 1/800 kyr were filtered. We performed NAFF in steps of 100 kyr with a window size of 3000 kyr, detrended by polynomial regression with order of 2, and instantaneous frequencies were calculated for every 1 kyr. Resonance shifts between 2.4 Myr to 1.2 Myr periods (Figure 2.5: dashed lines) are indicated at ~ 55 Ma, ~ 70 and ~ 90 Ma (arrows). We noticed increasingly more frequency artefacts (e. g. at ~ 18, ~ 35 and ~ 43 Ma) resulting from low amplitudes in the solution (see Supplementary Figure A8). The intervals 65 – 45 Ma and 75 – 60 Ma were chosen for further amplitude and filter analyses.

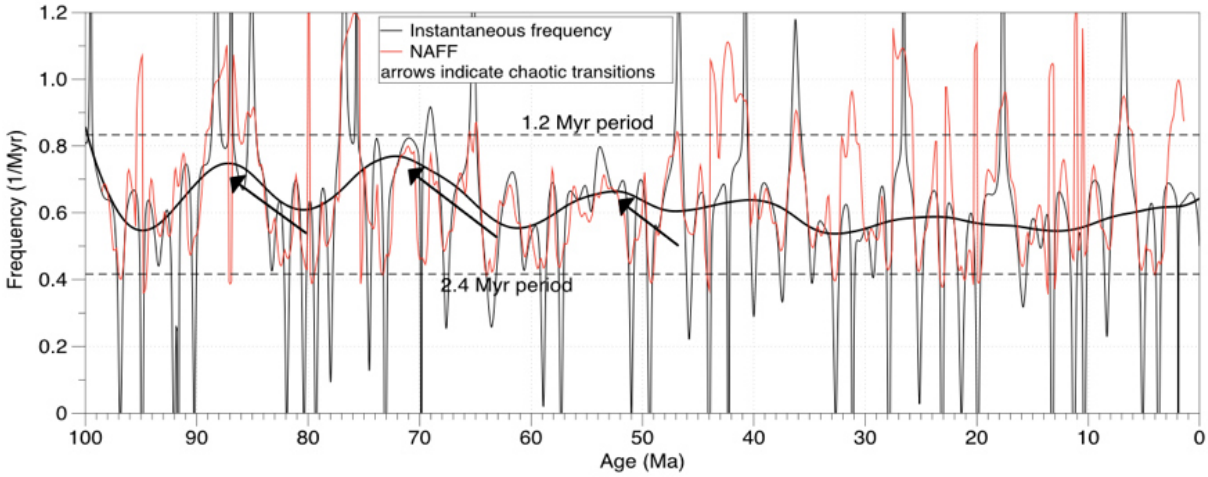

Figure 2.5. Frequency analyses of La2010c with additional noise (rho=0.9, sdv=0.013) over the last 100 Myr, applied on short eccentricity amplitude modulation. Fundamental frequency analyses (NAFF) showing (g_4- g_3) or 2(g_4 - g_3) frequencies (1/Myr: red). Instantaneous frequencies (1/Myr: black) with LOESS (LOcally Estimated Scatterplot Smoothing) trend line. Dashed lines mark 2.4 Myr and 1.2 Myr periods. Both frequency analyses calculated resonance shifts from ~ 2.4 Myr to ~ 1.2 Myr at ~ 55 Ma, ~ 70 and ~ 86 Ma (arrows). Several peaks (e. g. at ~ 18, ~ 35 and ~ 43 Ma) in frequency are artefacts of low amplitudes (see Supplementary Figure A8).

2.2.4.2. Amplitude analyses and filtering La2010c with noise, 45 – 60 Ma, 60 – 75 Ma

Using appended R script 'ChaosSearch.R', we filtered and demodulated long and short eccentricity and combined both. For additional amplitude investigation 2.4 and 1.2 Myr periods were filtered. An EHA from 0 – 0.02 cycles/kyr with a window size of 500 kyr and a step of 1 kyr padded to 5000 data points for each was applied. A linear trend and mean value were removed from each window. Figure 2.6 shows the results of amplitude analyses of the two different time intervals, 75 – 60 Ma (left) and 60 – 45 Ma (right). A few 2.4 and 1.2 Myr periods could be identified in short eccentricity amplitude (in Figure: o, p) and the combined filter of short and long eccentricity amplitude modulation (i, j). We also compared the amplitude of filtered 2.4 and 1.2 Myr cycles to determine chaotic intervals: High 2.4 Myr amplitudes vs. low 1.2 Myr amplitudes and a switch from a 2.4 to 1.2 Myr period are highlighted within the red boxes. From these analyses one may conclude the chaotic transitions to occur at ~ 55 Ma and ~ 70 Ma.

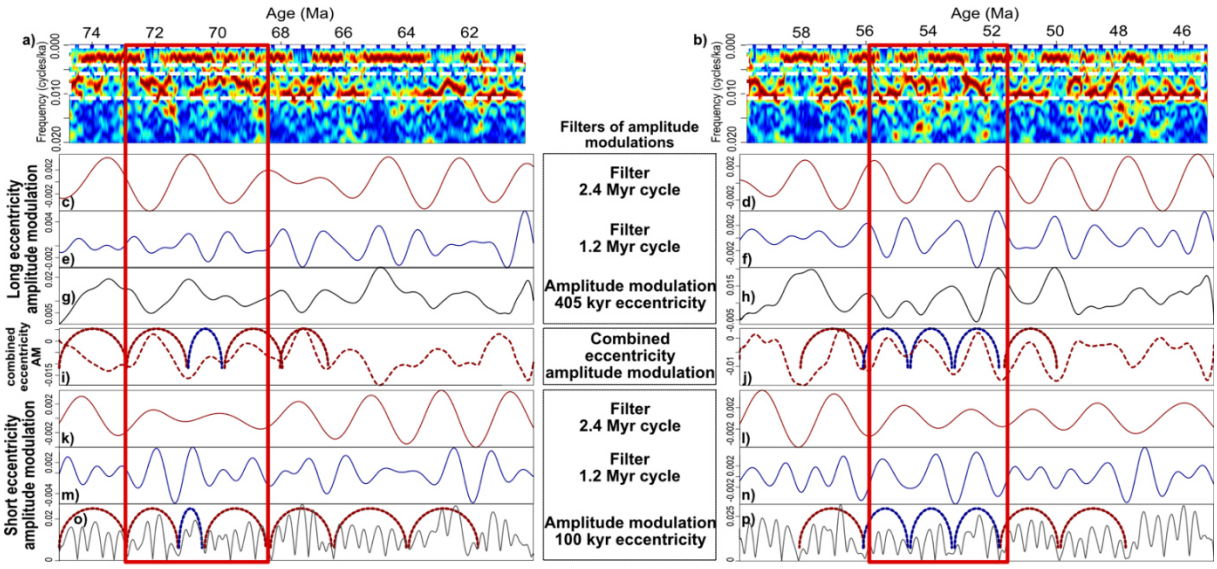

Figure 2.6. Amplitude analyses of two time intervals of La2010c with noise, 75 – 60 Ma (left) and 60 – 45 Ma (right). Evolutive harmonic analyses (EHA) results are displayed in the top panels (a, b). Filters of long eccentricity amplitude modulation (g, h), the combined amplitude modulation of short and long eccentricity (i, j) and short eccentricity (o, p) amplitude modulation together with filtered 1.2 Myr (dark blue: e, f, m, n) and 2.4 Myr (dark red: c, d, k, l) cycles from each amplitude modulation. In amplitude modulation of short eccentricity (o, p) and in combined filter (i, j) some recognizable periods of 2.4 (dark red) and 1.2 Myr (dark blue) are highlighted within red boxes. These also illustrate the phase opposition of long and short eccentricity. See legend of Figure 2.2 for details. During these time intervals, the 2.4 Myr period changes into a 1.2 Myr, hence we deduced a chaotic transition at ~ 55 Ma and ~ 70 Ma.

Applying and testing the methods on noisy data exposed limitations. The frequency analyses still show the transitions where they were expected and calculated in solution La2010c, but the artefacts occur more frequently in noisy dataset, which seriously challenges the interpretation. In the amplitude modulation of short eccentricity and in the combined filter of short and long eccentricity amplitude modulation, we could identify a few periods, but mainly we were able to detect the transitions with the help of amplitude comparisons of 2.4 and 1.2 Myr cycles. Without the reference from frequency analyses, it would be more difficult to identify resonance intervals.

We have tested and developed the methods on clean and noisy data successfully, which means, that we could find resonance transitions with frequency and filter/amplitude analyses exactly where they were calculated in astronomical solutions.

Now we intend to transfer this knowledge to real geological records reporting transitions and test these results.

2.3. Application on geological data

We intend to examine one recently published study reporting a chaotic transition: Westerhold et al. (2017) discovered a resonance transition at ~ 52 Ma in XRF data (Fe counts) of ODP Site 1258 (Leg 207, Demerara Rise).

2.3.1. ODP Site 1258, 46.95 – 56.63 Ma

We used appended R script 'ChaosSearch.R' on a calibrated XRF-data set (Fe counts) of Site 1258 (Westerhold et al., 2017) and applied the previously developed and tested approach of filter and amplitude analyses. EHA was conducted between 0 and 0.03 cycles/ka with a window size of 500 kyr and a step of 1 kyr. We calculated the instantaneous frequencies and performed NAFF as established above (Figure 2.7).
Both frequency analyses calculate a distinct switch back to a 'normal' remaining ~ 2 Myr period from an interval with a 'chaotic' ~ 1.2 Myr period (in Figure: dashed lines) at ~ 50 Ma (arrow). The jumps in frequencies at at ~ 48.5 and ~ 51 Ma were determined as artefacts due to low amplitudes (see Supplementary Figure A9).

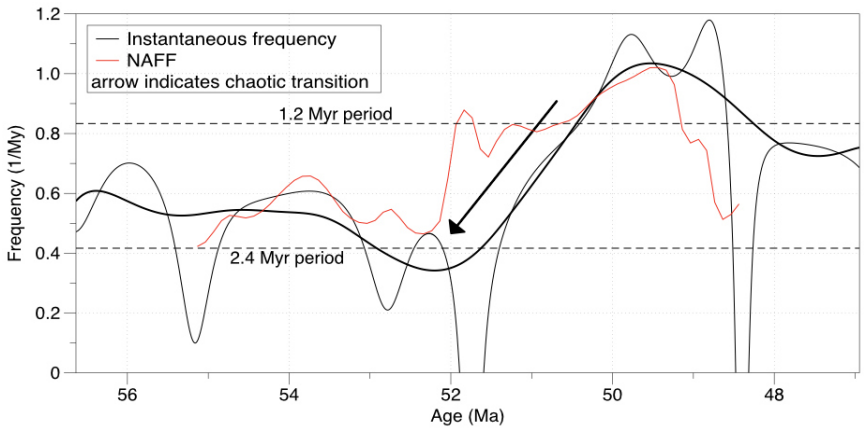

Figure 2.7 Frequency analyses of Site 1258 between 47 – 57 Ma, applied on short eccentricity amplitude modulation. Fundamental frequency analyses (NAFF) showing (g_4 - g_3) or 2(g_4 - g_3) frequencies (1/ Myr: red). Instantaneous frequencies (1/Myr: black) with LOESS (LOcally Estimated Scatterplot Smoothing) trend line. Dashed lines mark 2.4 Myr and 1.2 Myr periods. Both analyses calculate a distinct switch back to a ~2 Myr period at ~ 50 Ma coming from an interval with significantly shorter (~ 1.2 Myr) periods. The peaks at ~ 48.5, ~ 51 Ma) in frequency are artefacts of low amplitudes (see Supplementary Figure A9).

In Figure 2.8 we display the results of amplitude and filter analyses. We could identify a few 2.4 and 1.2 Myr cycles in the amplitude modulation of long and short eccentricity and oblquity (in Figure 2.8: d, h, k). Highlighted within the red box, we compared the amplitudes of filtered 2.4 Myr (f, i) and 1.2 Myr (g, j) cycles in short eccentricity and obliquity amplitude modulation. In resonance intervals we expect higher amplitudes of 1.2 Myr in contrast to 2.4 Myr cycles. On this basis we deduced a chaotic transition at ~ 50 Ma.

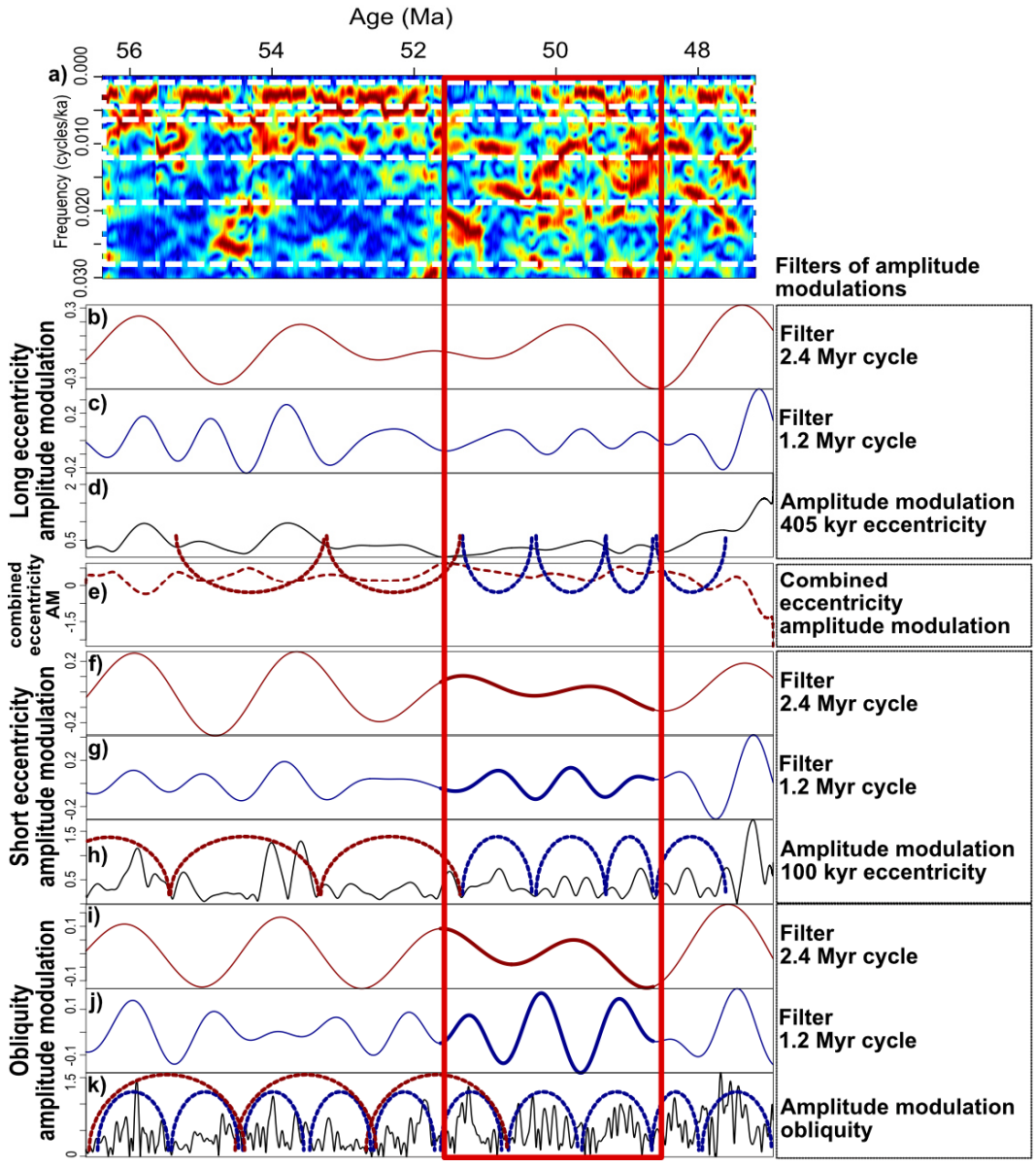

Figure 2.8. Amplitude Analyses of ODP Site 1258 (Fe), 47.03 – 56.09 Ma. Evolutive harmonic analyses (EHA) results are displayed at the top (a). Dashed boxes in a) indicate the filtered cycles (long and short eccentricity and obliquity). Panels below show from top to bottom: Filters of long eccentricity amplitude modulation (d), the combined amplitude modulation of short and long eccentricity (e), short eccentricity (h)

and obliquity (k) amplitude modulation together with filtered 1.2 Myr (dark blue: c, g, j) and 2.4 Myr (dark red: b, f, j) cycles from each amplitude modulation. In amplitude modulation (d, h, k) some recognizable periods of 2.4 (dark red) and 1.2 Myr (dark blue) are highlighted within red boxes. These also illustrate the phase opposition of long and short eccentricity. See legend of Figure 2.2 for details. Comparing the amplitudes of filtered 2.4 and 1.2 Myr helps to identify the resonance transition: High amplitudes of 1.2 Myr period in contrast to low amplitudes of 2.4 Myr period.

2.4. Discussion

2.4.1. Filter settings

2.4.1.1. Filter settings of short eccentricity and Taner roll-off rate

A most useful (Taner) filter should be set in a way to allow imperfect time scales and small shifts in the frequency to be filtered. At the same time wide filters will in reality include additional noise, therefore too wide filters are not desirable. The roll-off rate should be set in a way not to include too much noise. To account for both the results from experiments and these conceptual considerations, we propose using a Taner filter with cut-off frequencies set at 1/85 and 1/160, and a roll-off rate of 10^{10}. Especially higher roll-off rates give very similar results. Supplementary Figure A4 compares the results from a clean eccentricity, and the noisy ETP. The suggested filter settings obviously lead to satisfactory results.

2.4.1.2. Filter settings for long eccentricity

In order to enable to detect resonance switches in the amplitude modulation of long eccentricity, it is crucial to filter the g_3 - g_4 and $2(g_4$ - $g_3)$ components directly (see Supplementary Figure A5). Wider filtering causes disturbance in the filter output, narrow filtering excludes essential components. We propose filtering between 280 and 630 kyr, in order to minimise including too much noise, while considering, that much lower $2(g_4$ - $g_3)$ periods could be excluded. Reliable analyses should be only conducted compared to short eccentricity and/or obliquity as precaution.

2.4.2. Methodological considerations for detecting transitions

The here presented tests of methods helps to identify chaotic transitions in time series with limitations.

La2004, a solution consisting of long and short eccentricity and obliquity (and precession), makes it possible to recognize transitions by identifying the resonance change from 2.4 to 1.2 Myr in eccentricity and a missing 2.4 Myr cyclicity in obliquity amplitude modulation, even without filtering 1.2 and 2.4 Myr cycles and analysing their amplitudes (Figure 2.2). The transitions found here confirm the results of previous frequency analyses, since both NAFF and instantaneous frequency calculate transitions at ~ 58 Ma, ~ 75 Ma and ~ 88 Ma (Figure 2.1). Also apparent is the phase shift between obliquity and eccentricity and the phase opposition of short and long eccentricity. Filtering a combination of 1.2 and 2.4 Myr periods is beneficial, because these are always clear (Figure 2.2), and their amplitudes comparable. In resonance transitions, the 1.2 Myr period reaches highest amplitude while 2.4 Myr period disappears.

The application to the new solution Zb17e shows that it is also possible to discover the transition from inclination by filtering s_3 and s_4, g_3 and g_4. As similar to obliquity, the modulation of filtered s_3 and s_4, g_3 and g_4 results an amplitude with 2.4 and 1.2 Myr cycles. We could confirm that this solution exhibits only one transition at ~ 54 Ma and that the ~ 2.4 Myr periods remain shorter afterwards (here ~ 1.6 Myr; Figures 2.3 and 2.4). Similar to La2004 this solution is clean and the outcomes of all filter, frequency and amplitude investigations are equivalent.

To prepare these methods on geological data, we chose La2010c with additional auto-regressive noise, a record with well-known positions of chaotic transitions. Noise poses serious challenges when applying the methods, as exemplary, to a disturbed record. It became rather difficult to detect relevant 2.4 and 1.2 Myr periods in the amplitude modulation of long and short eccentricity. However, to compare the amplitudes of the filtered 1.2 and the 2.4 Myr periods helps to identify the transition (Figures 2.5 – 2.6).

For the development and tests on theoretical solutions La2004, La2010c and Zb17e we can summarize, that all frequency analyses calculate the transitions exactly where they were computed in their actual solution, as they are at ~ 58 Ma, ~ 75 Ma and ~ 88 Ma in La2004 and at ~ 55 Ma, ~ 70 Ma and ~ 86 Ma in La2010c and at ~ 54 Ma in Zb17e. Although both techniques of frequency analysis seem to be reliable, low

amplitudes can lead to artefacts in frequency analyses, which can lead to misinterpretations.

NAFF and fundamental frequency analyses of ODP Site 1258 (Westerhold et al., 2017) between 47 and 56 Ma display a distinct frequency switch at ~ 51 Ma (Figure 2.7). The obliquity influence during the analysed time interval of Site 1258 is not constant and vanishes at around 51.5 Ma (Figure 2.8). In short eccentricity and obliquity amplitude modulation, some short periods may be identified as indications for a resonance change, but especially comparing the amplitudes of filtered 2.4 and 1.2 Myr periods helps to identify the transition. However, it turned out that the combination of the amplitude modulations of short and long eccentricity is less useful due to the weak and unreliable 405 kyr amplitude modulation. Concerning the location of the transition, our analysis is consistent with Westerhold et al. (2017). However, without previous frequency analyses it would be much more difficult to detect resonance shifts in filter outputs and amplitude modulation. We suggest always combining frequency- and amplitude investigations on real geological data for a most robust interpretation.

2.4.3. Frequency analyses

Fundamental frequency analyses were conducted on short eccentricity amplitude modulation. The highest amplitude is the significant amplitude for every time step, even if the period is low. Further ~2.4 and or ~1.2 periods result from harmonics.

The most convenient window size is experienced to set at 3000 data points (kyr). Shorter windows were insufficient, as the output does not include the needed frequencies resulting from ($g_4 - g_3$; ~2.4 Myr). On the other hand, due to the long window size, the first and last inspected time step is window size/2 – time step, which is especially an issue for rather short data sets since it reduces the analysed data (for example: analyses between 90.18 and 85.38 Ma, in time steps of 100 kyr and a window size of 3000 kyr, first and last inspected average time step would be then 88.68 and 83.88 Ma). Especially for rather short dataset the window length limits applicability. However, it needs to be mentioned that also filters are not very reliably around the edges of datasets.

2.5. Conclusion

In order to verify and extend astronomical solutions, it is important to determine the exact timing of chaotic transitions in time series which most important manifestation is the change of two resonant astronomical frequencies of Mars' and Earth's orbit. To detect these transitions, we advocate the combination of frequency-, filter- and amplitude- analyses, which is a definite improvement to previous studies. Fundamental and instantaneous frequency analyses are able to display transitions that would possibly remain undetected in filter and amplitude analyses of noisy records (see application of the methods on Site 1258). In intervals of a resonance transition the 1.2 Myr period reaches highest amplitude compared to 2.4 Myr which will vanish due to the resonance switch of (g_4 - g_3) to 2(g_4 - g_3). We filter 2.4 and possible 1.2 Myr periods in order to determine the positions of transitions by investigating the amplitude of these two periods. This approach is particularly helpful and of great advantage over traditional filter and amplitude modulation analyses, because detecting chaotic transitions in disturbed “real” geological data is rather challenging. Applying the methods to ODP Site 1258 is difficult but trustworthy, because amplitude- (of 1.2 and 2.4 Myr cycles) and frequency analysis confirm each other and previous results from Westerhold et al. (2017). In general, it must be highlighted that the application to noisy data is difficult and caution is required with real geological data. The more lines of evidence, the more robust the application.

2.6. Acknowledgements

M.R. and H.P. were funded by the European Research Council Consolidator Grant Earth Sequencing (grant agreement 617462). CZ was funded by a PSL fellowship.

2.7. References

Emery, L., Borland, M., Shang, H., Soliday, R., 2008. User ’ s Guide for SDDS-compliant EPICS Toolkit Version 1 . 5.

Fang, Q., Wu, H., Hinnov, L.A., Jing, X., Wang, X., Jiang, Q., 2015. Geologic evidence for chaotic behavior of the planets and its constraints on the third-order eustatic sequences at the end of the Late Paleozoic Ice Age. Palaeogeogr. Palaeoclimatol. Palaeoecol. 440, 848–859. https://doi.org/10.1016/j.palaeo.2015.10.014

Hays, J.D., Imbrie, J., Shackleton, N.J., 1976. Variations in the Earth’s Orbit: Pacemaker of the Ice Ages. https://doi.org/10.1126/science.194.4270.1121

Hilgen, F.J., Hinnov, L.A., Abdul Aziz, H., Abels, H.A., Batenburg, S., Bosmans, J.H.C., de Boer, B., Hüsing, S.K., Kuiper, K.F., Lourens, L.J., Rivera, T., Tuenter, E., Van de Wal, R.S.W., Wotzlaw, J.-F., Zeeden, C., 2015. Stratigraphic continuity and fragmentary sedimentation: the success of cyclostratigraphy as part of integrated stratigraphy. Geol. Soc. London, Spec. Publ. 404, 157–197. https://doi.org/10.1144/SP404.12

Hinnov, L.A., 2013. Cyclostratigraphy and its revolutionizing applications in the earth and planetary sciences. Bull. Geol. Soc. Am. 125, 1703–1734. https://doi.org/10.1130/B30934.1

Hinnov, L.A., 2000. New Perspectives on orbitally forced Stratigraphy 12, 727–732. https://doi.org/10.1177/0741713604268894

Hinnov, L.A., Schulz, M., Yiou, P., 2002. Interhemispheric space-time attributes of the Dansgaard-Oeschger oscillations between 100 and 0 ka. Quat. Sci. Rev. 21, 1213–1228. https://doi.org/10.1016/S0277-3791(01)00140-8

Laskar, J., 2003. Chaos in the solar system, in: Annales Henri Poincaré. pp. 693–705. https://doi.org/10.1007/s00023-003-0955-5

Laskar, J., 2003. Frequency map analysis and quasiperiodic decompositions. https://doi.org/10.1109/PAC.2003.1288929

Laskar, J., 1999. The limits of Earth orbital calculations for geological time-scale use. Philos. Trans. R. Soc. A Math. Phys. Eng. Sci. 357, 1735–1759. https://doi.org/10.1098/rsta.1999.0399

Laskar, J., 1993. Frequency analysis for multi-dimensional systems. Global dynamics and diffusion. Phys. D Nonlinear Phenom. Vol. 67, Issues 1–3, 15 August 1993, Pages 257-281 67, 257–281. https://doi.org/https://doi.org/10.1016/0167-2789(93)90210-R

Laskar, J., 1990. The chaotic motion of the solar system: A numerical estimate of the size of the chaotic zones. Icarus 88, 266–291. https://doi.org/10.1016/0019-1035(90)90084-M

Laskar, J., Fienga, A., Gastineau, M., Manche, H., 2011. La2010: A new orbital solution for the long term motion of the Earth 4. https://doi.org/10.1051/0004-6361/201116836

Laskar, J., Joutel, F., Boudin, F., 1993. Orbital, precessional, and insolation quantities for the Earth from -20 Myr to + 10 Myr. Astron. Astrophys. (ISSN 0004-6361), vol. 270, no. 1-2, p. 522-533.

Laskar, J., Robutel, P., Joutel, F., Gastineau, M., Correia, A.C.M., Levrard, B., 2004. A long-term numerical solution for the insolation quantities of the Earth. Astron. Astrophys. 428, 261–285. https://doi.org/10.1051/0004-6361:20041335

Li, M., Hinnov, L.A., Huang, C., Ogg, J.G., 2018. Sedimentary noise and sea levels linked to land-ocean water exchange and obliquity forcing. Nat. Commun. 9. https://doi.org/10.1038/s41467-018-03454-y

Ma, C., Meyers, S.R., Sageman, B.B., 2019. Testing Late Cretaceous astronomical solutions in a 15 million year astrochronologic record from North America. Earth Planet. Sci. Lett. 513, 1–11. https://doi.org/10.1016/j.epsl.2019.01.053

Ma, C., Meyers, S.R., Sageman, B.B., 2017. Theory of chaotic orbital variations confirmed by Cretaceous geological evidence. Nature 542, 468–470. https://doi.org/10.1038/nature21402
Meyers, S.R., 2014. Astrochron: An R Package for Astrochronology.
Meyers, S.R., 2019. Cyclostratigraphy and the problem of astrochronologic testing. Earth-Science Rev. https://doi.org/10.1016/j.earscirev.2018.11.015
Meyers, S.R., 2015. Testing and Time Scale Optimization 1–16. https://doi.org/10.1002/2015PA002850.Received
Meyers, S.R., 2012. Seeing red in cyclic stratigraphy: Spectral noise estimation for astrochronology. Paleoceanography 27, 1–12. https://doi.org/10.1029/2012PA002307
Pälike, H., Laskar, J., Shackleton, N.J., 2004. Geologic constraints on the chaotic diffusion of the solar system. Geology 32, 929–932. https://doi.org/10.1130/G20750.1
Papaphilippou, Y., 1999. Frequency maps of LHC models. Proc. 1999 Part. Accel. Conf. (Cat. No.99CH36366) 3, 1554–1556. https://doi.org/10.1109/PAC.1999.794171
Pearson, K., 1895. Contributions to the Mathematical Theory of Evolution. III. Regression, Heredity, and Panmixia.
Shackleton, N.J., Hagelberg, T., Crowhurst, S.J., 1995. Evaluating the success of astronomical tuning: Pitfalls of using coherence as a criterion for assessing pre-Pleistocene timescales. Paleoceanography 10, 693–697. https://doi.org/10.1029/95PA01454
Taner, M.T., Koehler, F., Sheriff, R.E., 1979. Complex seismic trace analysis. Geophysics 44, 1041–1063. https://doi.org/10.1190/1.1440994
Team, R.D.C., R Development Core Team, R., 2016. R: A Language and Environment for Statistical Computing. R Found. Stat. Comput. https://doi.org/10.1007/978-3-540-74686-7
Vakman, D., 1996. On the analytic signal the teager-kaiser energy algorithm and other methods for defining amplitude and frequency. IEEE Trans. Signal Process. 44, 791–797. https://doi.org/10.1109/78.492532
Valluri, M., Merritt, D., 1998. Regular and Chaotic Dynamics of Triaxial Stellar Systems. Astrophys. J. 506, 686–711. https://doi.org/10.1086/306269
Westerhold, T., Röhl, U., Frederichs, T., Agnini, C., Raffi, I., Zachos, J.C., Wilkens, R.H., 2017. Astronomical Calibration of the Ypresian Time Scale: Implications for Seafloor Spreading Rates and the Chaotic Behaviour of the Solar System? Clim. Past Discuss. 1–34. https://doi.org/10.5194/cp-2017-15
Zeebe, R.E., 2017. Numerical Solutions for the orbital motion of the Solar System over the Past 100 Myr: Limits and new results. Astron. J. 154, 193. https://doi.org/10.3847/1538-3881/aa8cce
Zeeden, C., Kaboth, S., Hilgen, F.J., Laskar, J., 2018. Taner filter settings and automatic correlation optimisation for cyclostratigraphic studies. Comput. Geosci. 119, 18–28. https://doi.org/10.1016/j.cageo.2018.06.005

Zeeden, C., Meyers, S.R., Lourens, L.J., Hilgen, F.J., 2015. Testing astronomically tuned age models. Paleoceanography 30, 369–383. https://doi.org/10.1002/2014PA002762

Chapter 3

Investigating astronomical chaos in the Eocene-Paleocene-Late Cretaceous 69 - 34 Ma

Melanie Reinelt[1], Christian Zeeden[2], Mathieu Martinez[3], Heiko Pälike[1]

[1]MARUM - Center for Marine Environmental Sciences, University of Bremen, Leobener Str. 8, 28359 Bremen, Germany
[2]LIAG - Leibniz Institute for Applied Geophysics, GEOZENTRUM HANNOVER, Stilleweg 2, 30655 Hannover
[3]Université de Rennes 1, Géosciences Rennes, 263 Avenue Général Leclerc, 35042 Rennes CEDEX

Abstract

The use of astronomical models to improve geological time scales is limited due to the chaotic behaviour of the solar system. It is thus important to determine the signatures of astronomical chaos in geological data in order to test the applicability of astronomical solutions. One manifestation of astronomical chaos should be detectable in the evolution of g_4 - g_3 and $2(g_4$ - $g_3)$ periods in eccentricity and obliquity amplitude modulation. As a complete and long geological record is essential, we generated a splice of seven IODP/ODP datasets representing iron content from globally distributed sites. This splice covers the Eocene, the Paleocene and encompasses the Cretaceous-Paleogene boundary. We applied thoroughly tested techniques consisting of fundamental and instantaneous frequency analyses and amplitude investigations including additional inspections of extracted 2.4 and/or 1.2 Myr periods. In order to test which solution represents geological data best, we calculated Thomson Multitaper evolutive spectra of various established solution for comparison with the analysed K/Pg-Splice. This investigation concludes that the two indications of chaotic transitions we detected between ~44 – ~52 Ma and ~63 – ~66 Ma are most in accordance with the calculations of La2010a and La2010d.

3.1. Introduction

Cyclostratigraphy has become an important part of integrated stratigraphy (Hilgen et al., 2015; Hinnov, 2013), and can be combined with other stratigraphic and dating methods to establish precise and high-resolution integrated geological time scales (e.g. Gradstein et al., 2012; Hilgen et al., 2012; Hinnov and Hilgen, 2012). Age models have been constructed by correlating geological data to theoretical astronomical solutions as tuning targets. As the solar system is chaotic, it is impossible to predict the movements of all bodies from their current positions, masses and velocities (Laskar, 1990) precisely over long time scales. Chaos poses limits to integrate Earth's astronomical motions beyond 50 Ma. Consequently, the establishment of astronomical solutions for creating astronomically calibrated geological time scales is limited (Laskar, 1999).

To verify and extend theoretical astronomical models, it is important to detect signatures of the chaotic motion in the geological record. Initially tested by Pälike et al. (2004), this subject has received increased attention recently (e.g. Fang et al., 2015;

Ma et al., 2017, 2019; Olsen et al., 2019; Westerhold et al., 2017). A quantifiable chaotic motion of the solar system can manifest itself in a resonance change of the secular (fundamental) frequencies between Mars and Earth. The frequencies of Mars' and Earth's orbit expressed in $2(s_4 - s_3) = (g_4 - g_3)$ oscillate at present in libration with a resonance of 2:1. This motion may not be stable and has alternated with circular motion with a resonance of 1:1 expressed in $(g_4 - g_3) = (s_4 - s_3)$ and into a new 2:1 libration resonance with different $g_4 - g_3$ and $2(g_4 - g_3)$ periods afterwards. This resonance change should be observable in the geological record by investigating amplitude modulation patterns of eccentricity and obliquity (e.g. Hinnov, 2018; Pälike et al., 2004; Shackleton et al., 1995).

Short eccentricity amplitude modulation terms $(g_4 - g_5) - (g_3 - g_5)$ and $(g_4 - g_2) - (g_3 - g_2)$ result in a period of 2.4 Myr $(g_4 - g_3)$ and during a resonance transition in ~1.2 Myr $(2(g_4 - g_3))$ (Laskar, 1999). In obliquity amplitude modulation, the terms $(p + s_3) -$ $(p + s_3 + g_4 - g_3)$ (40.27 kyr) and $(p + s_3) - (p + s_3 - g_4 + g_3)$ (41.647 kyr) result in a beat term of $(g_4 - g_3)$ (2.4 Myr). This component does not exist during transitions. Conversely, $p + s_3$ (40.996 kyr) and $p + s_4$ (39.657 kyr), producing the beat term $(s_4 – s_3)$ (1.2 Myr), remain (Hinnov, 2013, 2000; Laskar, 1990). The most recent resonance transition was reported by Westerhold et al. (2017) at ~52 Ma in XRF data of OPD Site 1258 fitting well to La2010b and La2010c (Laskar et al., 2011a).

Here, we apply improved techniques developed by Reinelt et al. (2019, in review) including fundamental and instantaneous frequency analyses, amplitude analyses and their combination for the identification of transitions in geological datasets. During a chaotic transition, we expect a distinct pattern characterised by a missing 2.4-Myr cyclicity in eccentricity and obliquity amplitude.

The most critical time period to investigate for chaotic transitions is those closest to the limit of astronomical solution accuracy from 50 Ma back in time (Hinnov, 2018).

For this purpose, we investigated a continuous XRF-splice (Fe counts) spanning the Eocene, the Paleocene and part of the Late Cretaceous. As the cyclicity expressed by XRF measurements can be attributed to the orbital forcing of a combination of climate, ocean circulation, or biological productivity (Pälike et al., 2001; Röhl et al., 2001; Westerhold et al., 2007, 2008) we chose Fe counts as consistently available proxy, considering that the detailed phasing relationship between forcing and response can vary.

3.2. Material

3.2.1. Data XRF Splice

The aim of the XRF-Splice is to provide a continuous and high-resolution dataset for over 35 million years, intended to serve as a useful record to search for evidences for astronomical chaos. We spliced seven IODP/ODP datasets from globally distributed sites (Figure 3.1). The used Fe-records were published with respective astronomically tuned age models: ODP Site 320-U1333 (Westerhold et al., 2014), ODP Site 207-1260 (Westerhold & Röhl, 2013), ODP Sites 198-1209 and 208-1262 (Westerhold et al., 2007, 2008), ODP Sites 208-1263 and Site 207-1258 (Westerhold et al., 2017), and IODP Site 342-U1403 (Friedrich et al., 2016).

The XRF data of Site ODP Site 320-U1333 was tuned to a combination of La2011 (Laskar et al., 2011b) and La2004 (Laskar et al., 2004), as both eccentricity solutions are almost identical and La2004 also contains calculations for obliquity and precession (Westerhold et al., 2014). For XRF data of ODP Site 207-1260, Fe peaks were assumed to be precession maxima and were tuned to La2004 precession, with an error of $\pm$ 20 kyr (Westerhold & Röhl, 2013). XRF data of ODP Sites 198-1209 and 208-1262 were first tuned to 100 kyr and 405 kyr La2004 eccentricity (Westerhold et al., 2007, 2008), and later used for a multi-proxy data analysis (Westerhold et al., 2017): Together with XRF data of ODP Sites 208-1263 and 207-1258, the datasets were calibrated using the approach of Zeeden et al. (2015) by extracting short eccentricity from the precession signal and using short eccentricity amplitude modulation for tuning to La2004 (Laskar et al., 2004), La2010d (Laskar et al., 2011a) and La2011 (Laskar et al., 2011b). XRF data of IODP Site 342-U1403 was tuned to the 405 kyr eccentricity of La2011 by Friedrich et al. (2016).

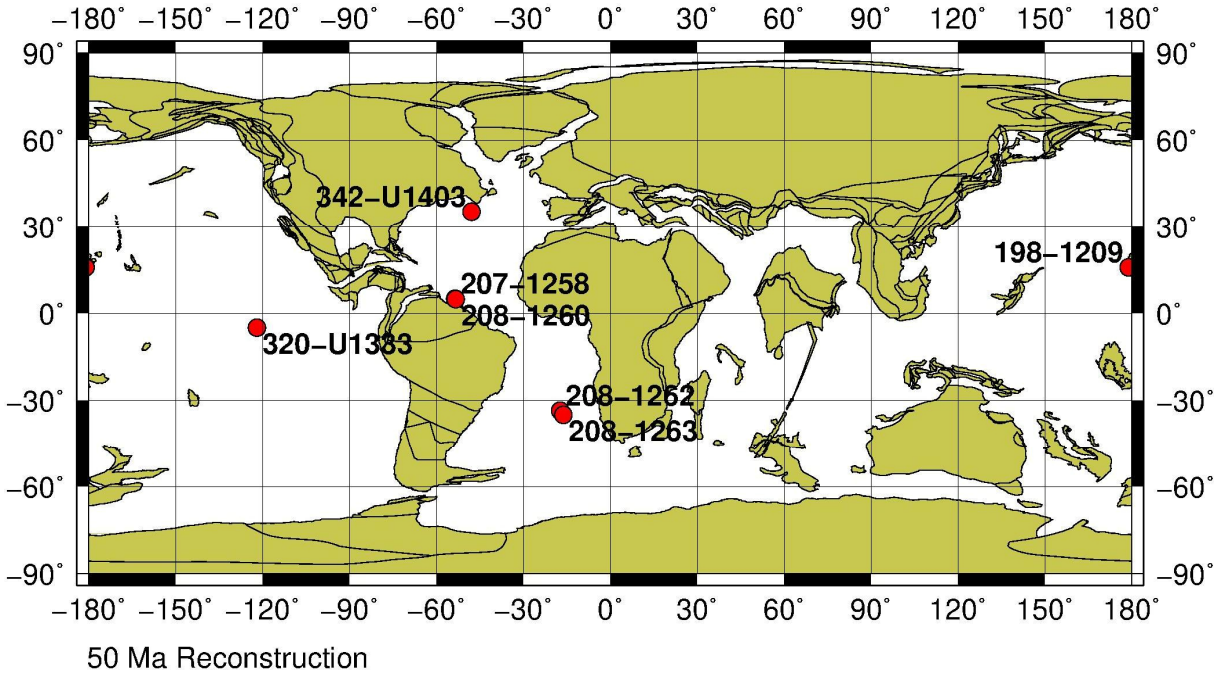

Figure 3.1 Palaeogeographic reconstruction (50 Ma) showing the locations of the Sites examined in this study. The map was constructed using ODSN Paleomap project: www.odsn.de/odsn/services/paleomap/paleomap.html

The presented splice spans the Eocene, the Paleocene and part of the Late Cretaceous, as indicated by magnetostratigrapy, biostratigraphy and astronomical tuning (Friedrich et al., 2016; Westerhold et al., 2017, 2014, 2008, 2007; Westerhold and Röhl, 2013). The entire splice contains 18,119 XRF measurements (Fe) and its average resolution is 1.91 kyr.

3.2.2. Splicing

The splice is the result of a combination of seven XRF (log_{10}[Fe counts]) records. All raw datasets were interpolated with individual mean sampling resolution and were plotted before detrending and normalization in Supplementary Figure B1. Before splicing, all datasets were smoothed by 10 % LOWESS regression (Cleveland, 1979) and detrended by subtracting the smoothed signal. For normalizing to unit variance, all datasets were divided by individual standard deviation after detrending (standard deviation = 1, mean = 0 for all) (Figure 3.2). As base anchor point for splicing, we used the U-Pb CA-ID-TIMS of the K/Pg-boundary of 66.021 ±0.081 Ma (Clyde et al., 2016). The start and end positions of anchor points (in depth domain) are given in Table 3.1.

Table 3.1 All sites with start and end positions in depth domain (revised meters composite depth, rmcd) with mean sample interval (dtmean), datapoints between start and end position, the intensity mean (mean int_sign) and the standard deviation (sd int_sign) of the interpolated signal (interpolated with dtmean). See Supplementary Figure B1 for all individually interpolated, undetrended and unnormalized datasets.

Site	Start Position depth (rmcd)		End Position depth (rmcd)		dtmean (m)	Data points	mean int_sign (log_{10})	sd int_sign (log_{10})
1403	274.72	End of data set	247.7	K/Pg	0.017	1598	4.53	0.15801
1209 1262	261.52	K/Pg	161.7	ELMO	0.020	4993	2.45	0.33579
1258	127.69	ELMO	39.19	BaseC21n	0.020	4329	3.38	0.13882
1263	217.94	BaseC21n	172.9	BaseC20n	0.021	2120	3.00	0.17401
1260	123.47	BaseC20n	64.07	TopC19n	0.021	2848	3.09	0.11054
1333	181.47	TopC19n	135.8	Ec/Oc	0.021	2189	4.32	0.20716

Splice 1209/1262 was created to bridge the condensed interval of Site 1262 with Site 1209, which has a higher resolution (Westerhold et al., 2008). The astronomical calibration of Westerhold et al. (2008) was revised by Hilgen et al. (2014). It turned out, that between K/Pg boundary and the Latest Danian Event (LDE) one 405 kyr cycle was missing. We used the age model of Hilgen et al. (2014) for this interval and the age model of (Westerhold et al., 2008) for the rest of splice 1209/1262.

The anchor points in the depth domain were calibrated with a new age resulting from anchoring to the absolute age of the K/Pg boundary. Beginning with the splice of Sites 1209/1262, we calibrated the position of the K/Pg boundary to 66.021 Ma, resulting in a new age for the next anchor point (ELMO, EMT-2; 54.037 Ma). This new age was then used for splicing Site 1258, which resulted in a new age for magnetochron Base C21n (47.889 Ma). This age was transferred to Site 1263 and led to a new age for magnetochron Base C20n (43.696 Ma), and so on, until we reached the end of our splice at the Eocene-Oligocene boundary with an age of 34.133 Ma (Figure 3.2).

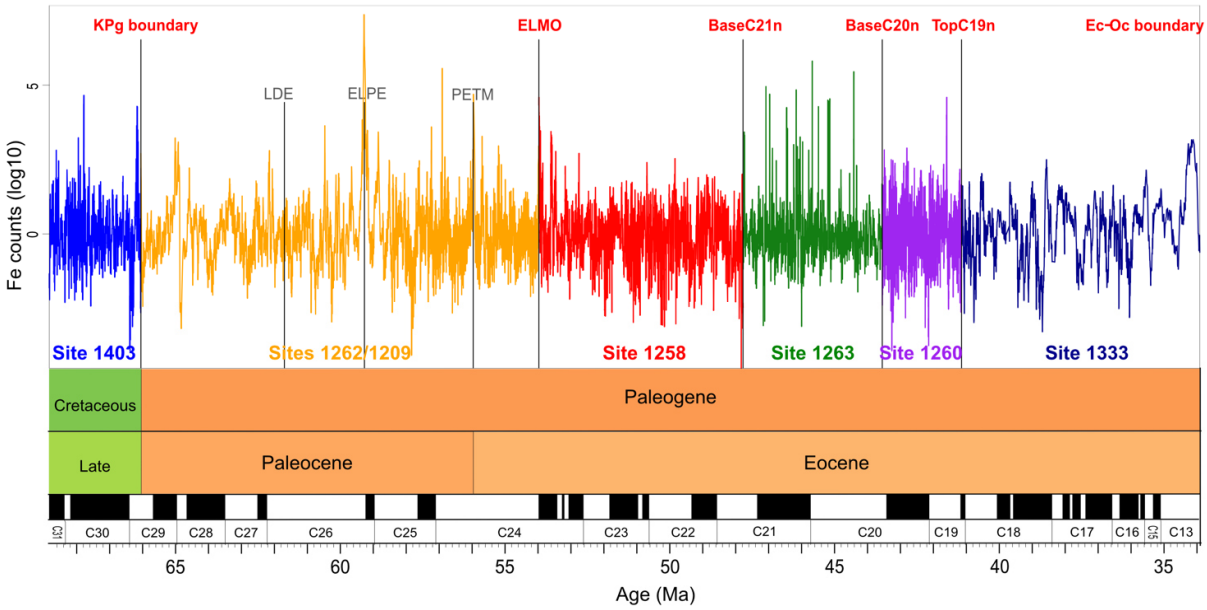

Figure 3.2 XRF (log_{10} Fe counts) splice from 34.13 to 68.78 Ma, consisting of seven globally distributed records with anchor points and 3 additional markings for events (LDE, ELPE and PETM). All datasets were detrended and normalized before splicing as described in text above. The absolute age of the K/Pg boundary was used as main anchor, which result in new subsequently calibrated ages for all anchor points (see Table 3.2).

The differences to the reference ages from GTS2012 (Gradstein et al., 2012) or (Westerhold et al., 2008) relative to 66.021 Ma are given in Table 3.2. In the perspective of detecting changes in the 2.4-Myr cycle, these age model differences appear too small compared to the periods explored to impact their identification (Martinez et al., 2016).

Table 3.2 Anchor used for splicing, with the main anchor of K/Pg boundary at 66.021 Ma and resulting ages for subsequent anchor points compared to reference ages.

Site	Start Position Age (Ma)		End Position Age (Ma)		Age (Ma)		Offset (kyr)
1403	K/Pg	66.021	End of data set	68.837	66.021	Clyde et al., 2016	
1209/ 1262	K/Pg	66.021	ELMO	54.037	54.438	Westerhold et al., 2008	-401
1258	ELMO	54.037	BaseC21n	47.889	47.349	GTS2012	540
1263	BaseC21n	47.889	BaseC20n	43.696	43.432	GTS2012	264
1260	BaseC20n	43.696	TopC19n	41.308	41.157	GTS2012	151
1333	TopC19n	41.308	Ec/Oc	34.133	33.89	GTS2012	243

After splicing, the entire record was interpolated with the mean average temporal resolution (1.91 kyr) in order to perform Multitaper method (MTM) spectral and frequency analyses.

3.3. Methods

To follow the approach of Reinelt et al. (2019, *in review*), we performed fundamental and instantaneous frequency analyses and investigated the amplitudes of eccentricity and obliquity to identify resonance transitions in geological datasets. For amplitude analyses and filtering, we used the R-Script ChaosSearch.R (appended in supplementary material).

The upper and lower frequencies for Taner filtering (Taner et al., 1979) ensuring the best extraction of astronomical (interference) signals were determined as follows: Long eccentricity between 1/630 and 1/280 kyr, short eccentricity between 1/160 and 1/85 kyr and obliquity between 1/54 and 1/35 kyr, For further ampltide investigations, we filtered the $g_4 - g_3$ (2.4 Myr) and (possible) $2(g_4 - g_3)$ (1.2 Myr) periods (2.4 Myr: 1/3500 kyr - 1/1800 kyr; 1.2 Myr: 1/1800 kyr - 1/800 kyr). All Taner filters have a roll-off rate (steepness of filter) of 10^{10}.

3.3.1. Frequency analyses

3.3.1.1. Fundamental frequencies

To determine the fundamental frequency components we used a Swift language implementation based on the SDDS (Self Describing Data Sets) Toolkit Version 3.5.1 (Emery et al., 2008) for Fortran (https://paloz.marum.de/confluence/display/ESPUBLIC/NAFF). The application is adapted from Laskar's Numerical Analysis of Fundamental Frequencies (NAFF) algorithm (Laskar, 1999; Laskar, 2003). From a definite window, it calculates a list of the strongest amplitude frequencies by using a moving window approach with a window size of 3000 kyr in steps of 191 kyr (191 kyr, a multiple of $1.91\Delta t$). Each window was detrended by polynomial regression (here of order 3). The output contains frequency, amplitude, phase, significance and period, starting from t0 of each window and is sorted within the windows by decreasing amplitude. We analysed the demodulated short eccentricity signal and extracted $(g_4 – g_3)$ or $2(g_4 - g_3)$ frequencies.

3.3.1.2. Instantaneous frequencies

Hilbert transformation extracts the instantaneous frequency, the amplitude and the phase of a signal (e.g. Hinnov et al., 2002; Taner et al., 1979; Vakman, 1996). We calculated instantaneous frequencies from the amplitude envelope of short eccentricity extracted from the entire splice in 1.9 kyr time steps. The fundamental frequency terms of short eccentricity producing the $g_4 – g_3$ beat term period of ~2.4 Myr are $(g_4 – g_5) – (g_3 – g_5)$ and $(g_4 – g_2) – (g_3 – g_2)$. Since filtering and demodulation short eccentricity includes the g_3 and g_4 frequencies directly, short eccentricity amplitude modulation is best suited to investigate resonance changes from $g_4 – g_3$ to $2(g_4 – g_3)$.

The frequency range we intend to focus on only includes possible resonance changes from $(g_4 - g_3)$ to $2(g_4 - g_3)$ with frequencies between 1/1800 and 1/800 for $2(g_4 - g_3)$ and 1/3500 – 1/1800 kyr for $g_4 - g_3$, so we filtered short eccentricity amplitude modulation between 1/3500 kyr and 1/800 kyr. We emphasize here that low amplitudes induce artefacts in form of sharp peaks in frequency analyses that may lead to misinterpretation, so we highlighted the intervals in Figures, where special caution is needed.

3.3.2. Amplitude analyses

We performed Evolutive harmonic analyses (EHA) of the splice using the ‘eha’ function provided in the “astrochron” package (Meyers, 2014) for R (R Core Team, 2016) with a time step of 2 kyr and a window size of 800 kyr, padded to 5000 data points. A linear trend and mean value were removed from each window before analysis.

We extracted short and long eccentricity and obliquity by Taner band-pass filtering with filter settings mentioned above. Hilbert transformation calculated the instantaneous amplitude modulation of each cycle. The output of essential periods of the Taner band-pass filters in the amplitude modulation possibly reveal indications for a resonance shift from a 2.4 to a 1.2 Myr period. During a resonance transition, long and short eccentricity amplitude modulation should express the change of $g_4 – g_3$ into $2(g_4 - g_3)$ with an opposite phase. In order to amplify the signal, we combined these two amplitude modulations by subtracting long eccentricity amplitude from short eccentricity amplitude (see Figure 3.4, ‘combined eccentricity AM’). In obliquity, the expression $g_4 – g_3$ (2.4 Myr) should be missing during transitions, while the $s_4 - s_3$ (1.2 Myr) term remains.

3.3.3. Comparison with astronomical solutions

To test and verify astronomical models, we intend to determine the discrepancies between real geological data and various established solutions of La2010a, La2010b, La2010c, La2010d, La2011 (Laskar et al., 2011a, 2011b), La2004 (Laskar et al., 2004) and ZB17e (Zeebe, 2017). Of all ZB17 solutions, we chose ZB17e for a better comparison: The ZB17e solution was calculated with the INPOP13c (Fienga et al., 2014) ephemeris and 10 asteroids, similarly to La2010/2011 solutions, calculated with INPOP6 and INPOP8 (Fienga et al., 2009, 2006) and INPOP10a (Fienga et al., 2011) ephemeris and 5 asteroids.

Determining discrepancies between the solutions and geological data can be best achieved by comparing the evolution of frequencies supported by an evolutive spectrum, which should indicate specific ratio switches from ~2.4 Myr to 1.2 Myr. A strong frequency response close to 1/0.41 Myr indicates a near ~2.4 Myr long eccentricity cycle, whereas values around 1/0.833 Myr indicate a switch towards a ~1.2 Myr cycle. For this purpose, we filtered short eccentricity amplitude modulation between 800 and 3500 kyr of the K/Pg-Splice and above mentioned astronomical solutions. and computed Thomson Multitaper (Thomson, 1982) evolutive spectra using a macOS tool (https://paloz.marum.de/confluence/display/ESPUBLIC/Spectrogram).

The parameter for computing evolutive spectra for solutions were: bandwidths product nw: 4, number of tapers: 6, points per window: 512, window increment: 64, FFT points: 4069, fmax: 0.016, and the adapted parameter for the K/Pg-Splice with different resolution were: bandwidths product nw: 4, number of tapers: 3, points per window: 1024, window increment: 64, FFT points: 4069, fmax: 0.008.

3.4. Results

3.4.1. Frequency analyses of megasplice

Fundamental frequency analyses (NAFF) were performed and instantaneous frequencies were calculated for every 1 kyr over the whole time span of our splice. For immediate comparison, we plotted the amplitude modulation of short eccentricity, filtered between 1/800 and 1/3500 kyr (Figure 3.3), amplitudes around zero inducing frequency peaks are red-marked.

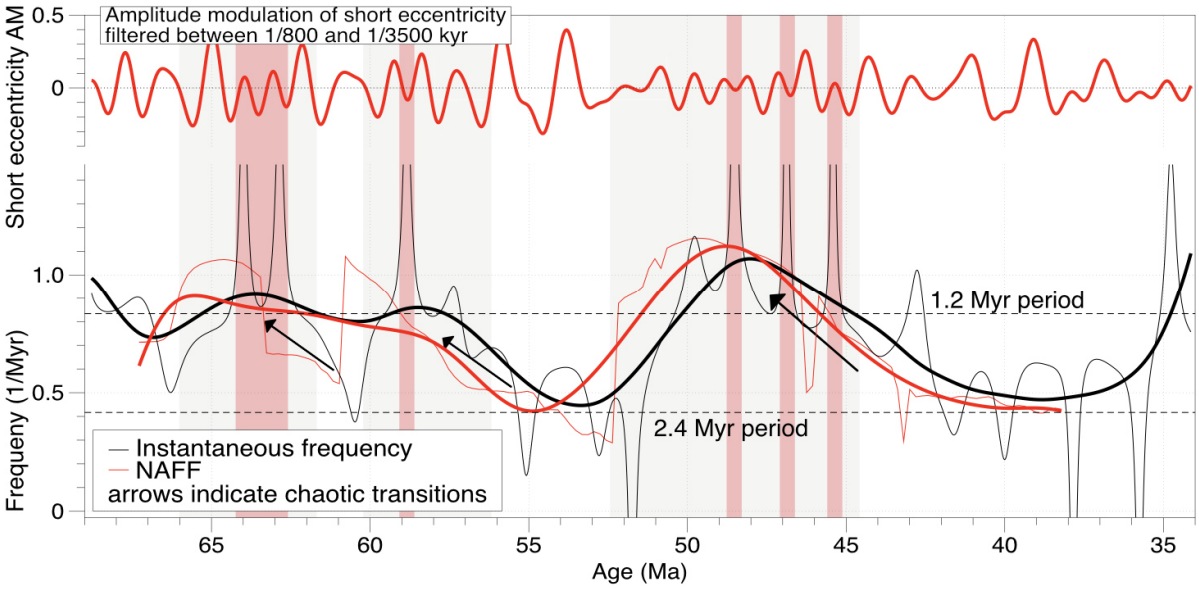

Figure 3.3 Frequency analyses of the splice applied on short eccentricity amplitude modulation. At the top: Amplitude modulation of short eccentricity filtered between 1/3500 and 1/800 kyr. Below: Fundamental frequency analyses (NAFF) showing (g_4 - g_3) or 2(g_4 - g_3) frequencies (1/Myr; red) between 1/3500 and 1/800 kyr. Instantaneous frequencies (1/Myr; black) with LOESS (LOcally Estimated Scatterplot Smoothing) trend line. Dashed lines mark 2.4 Myr and 1.2 Myr periods. Resonance shifts to ~1 Myr are indicated at ~44 – 52 Ma, ~56 – 60 Ma and ~63 – 66 Ma (arrows). The youngest transition switches back into ~2.4 Myr soon afterwards. The two shifts around ~59 and ~65 Ma occur too close to switch back in between. The sharp peaks in frequency (red marked) are an effect of a zero amplitude (we refer to the amplitude modulation of short eccentricity, red line at the top). This is no indication for a transition. The amplitude modulation of short eccentricity displays shorter periods during the intervals of resonance change (grey boxes) and a weak signal between 44 and 54 Ma.

The frequency analyses express resonance shifts between ~44 and 52 Ma, and two consecutive shifts between ~56 and 66 Ma, with slight discrepancies in the timing of the shift between NAFF and instantaneous frequency analyses. The amplitude of short eccentricity (red line at top of Figure 3.3) shows a weak signal from 44 to 54 Ma and shortened periodicities during the resonance shift intervals. On this account, detailed amplitude analyses were conducted in order to evaluate whether these resonance changes are evidences for astronomical chaos.

3.4.2. Amplitude analyses to investigate resonance shifts

For the evaluation of previous results, we performed complex amplitude analyses demonstrated in Figure 3.4. We investigated short and long eccentricity amplitude modulation and their combination, of obliquity amplitude modulation, and additional filtered $g_3 - g_4$ and $2(g_3 - g_4)$ periods. Within the red boxes (recognised as intervals of resonance shifts in frequency analyses), the filtered grand cycles (~2.4 and ~1.2 Myr) are highlighted, when they show an amplitude ratio suggesting a chaotic transition. During a chaotic transition, the $g_4 - g_3$ amplitude falls to zero, while the amplitude of $2(g_4 - g_3)$ increases, here apparent between ~44 and ~52 Ma. The resonance interval between 56 – 66 Ma implied by frequency analyses (red box) has no significant obliquity imprint, so that investigation could only be carried out on eccentricity. The amplitudes of the filtered ~2.4 and ~1.2 Myr cycles of short eccentricity display the specific ratio already at ~63 Ma, as the amplitude modulation and filter of long eccentricity show that particular pattern between ~64 and ~66 Ma. Some periods could be recognized in EHA spectrum (black markings).

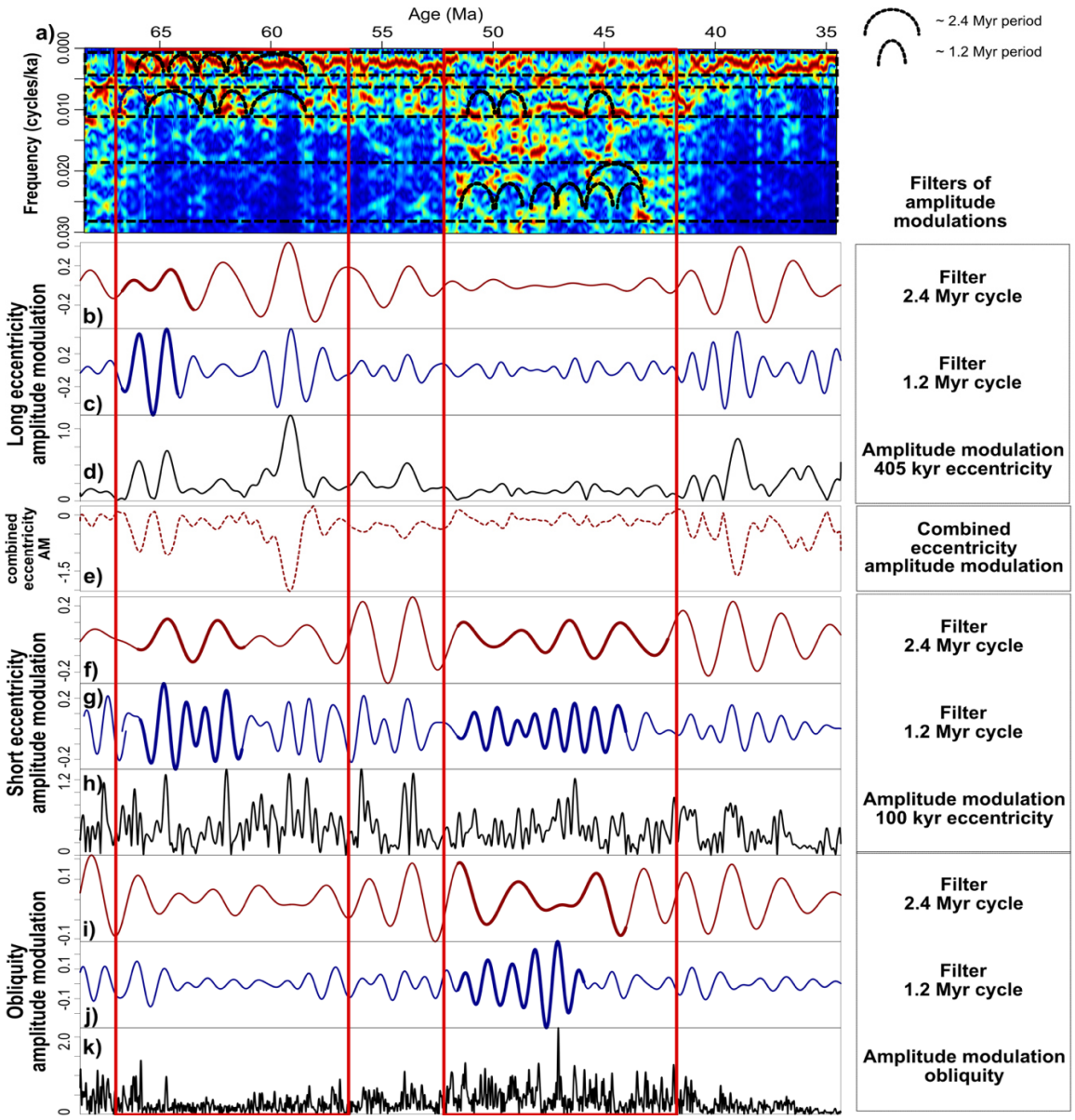

Figure 3.4 Amplitude analyses of the XRF-Splice. Evolutive harmonic analyses (EHA) results are displayed at the top (a). Panels below show from top to bottom: Filters of long eccentricity amplitude modulation (d), the combined amplitude modulation of short and long eccentricity (e), short eccentricity (h) and obliquity (k) amplitude modulation together with filtered $2(g_4 - g_3)$ (1.2 Myr, dark blue: c, g, j) and $g_4 - g_3$ (2.4 Myr, dark red: b, f, i) cycles from each amplitude modulation. The red boxes represent the intervals of resonance shifts recognised by frequency analyses. Between ~44 and 52 Ma higher $2(g_4 - g_3)/g_4 - g_3$ (~1.2/2.4 Myr) amplitude ratios are apparent in short eccentricity and obliquity amplitude modulation (marked by thick lines). Between 56 – 66 Ma the record has no obliquity imprint, but the amplitudes of short and long eccentricity indicate distinct amplitude ratios between ~63/64 and ~66 Ma (marked by thick lines), affirmed by some recognized ~1.2/~2.4 Myr periods in EHA spectrum (black markings).

3.4.3. Comparison with astronomical solutions

in order to compare the evolution of established solutions with our K/Pg-Splice and to determine the most fitting solution, all computed Thomson Multitaper (Thomson, 1982) evolutive spectra are plotted in Figure 3.5.

Starting from the transitions detected with further analysed and indicated in the evolutive spectrum of the K/Pg-Splice (1. top panel, red bordered boxes), overlaps are sought in the lower panels of the respective solutions. From top to bottom are displayed: The evolutive spectrum of 2. La2004, 3. La2010a, 4. La2010b, 5. La2010c, 6. La2010d, 7. La2011, 8. ZB17. La2004 shows a resonance transition at 55 – 60 Ma, La2010a indicates two transitions between ~57 and 60 Ma, and ~43 – 49 Ma. The resonance switches of La2010b and La2010c are similar between ~65 – 68 Ma, ~50 – 58 Ma. La2011 and ZB17e show switches at ~53 – 59 Ma. Overlaps of indicated transitions are obvious between the K/Pg-Splice and La2010a at 44 – 52 Ma, and between the K/Pg-Splice and La2010d at 63 – 66 Ma.

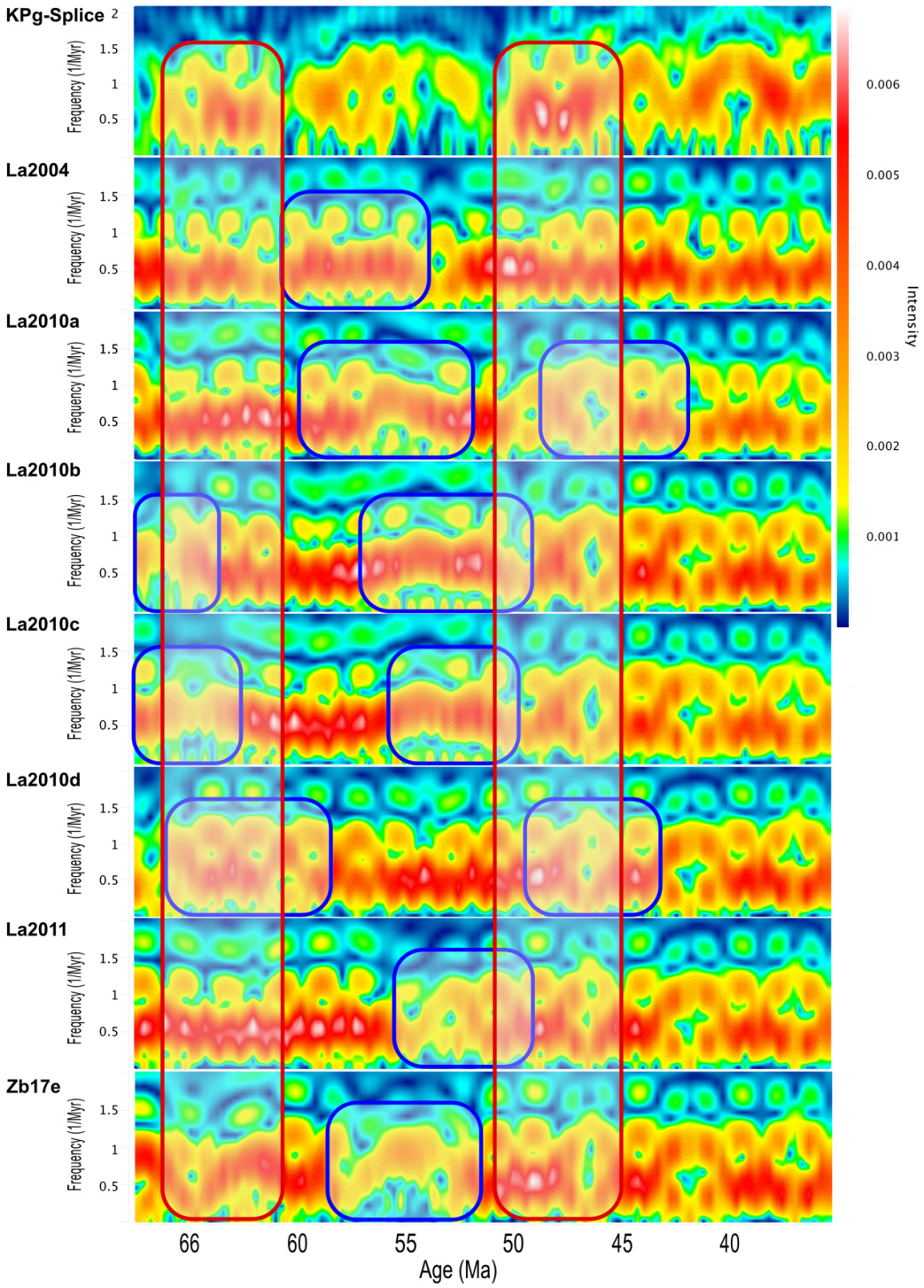

Figure 3.5 Thomson Multitaper evolutive spectrum calculated from short eccentricity amplitude modulation filtered between 800 and 3500 kyr. From top to bottom: K/Pg-Splice, La2004, La2010a, La2010b, La2010c, La2010d, La2011, ZB17e. The red bordered boxes indicate time intervals showing resonance switches in the K/Pg-Splice. The blue bordered boxes highlight resonance intervals in the respective solutions. Overlaps between the K/Pg-Splice transitions and the transitions in the solutions are obvious at ~44 – 52 Ma (K/Pg-Splice/ La2010a) and at ~63 – 66 Ma (K/Pg-Splice/ La2010d).

3.5. Discussion

3.5.1. Compatibility of Fe records

Since the Fe records originated from different regions with distinct local influences, it is important to ensure that they are nevertheless compatible in recording astronomical forcing. In order to ensure the compatibility, the data sets were detrended and then normalized. The cyclicity is not affected by the strength of Fe signals, but the amplitude is. This should be considered in the interpretation. In Supplementary Figure B1 all interpolated logarithmic datasets are plotted before they were detrended and normalized to visibly demonstrate the respective signals when interpreting the amplitudes.

In addition, we carried out instantaneous frequency analyses on all the individual datasets in order to exclude compatibility errors, which we return to in next section.

3.5.2. Splicing

The cycle-tuned durations of magnetochrons have estimated uncertainties up to 100 kyr (Westerhold et al., 2017, 2014, 2008; Westerhold and Röhl, 2013) depending on core quality, sampling resolution, condensed intervals, measurement uncertainties and other effects (e.g. Martinez et al., 2016; Zeeden et al., 2015). The absolute age of the K/Pg-boundary, based on the CA-ID-TIMS U-Pb age determination, has an uncertainty of 81 kyr (Clyde et al., 2016). Summarizing the errors regarding 3 magnetochrons and one ELMO-Event, the resulting age difference of -243 kyr for the Eocene-Oligocene boundary lies within error margins. Note that the age of ELMO has a difference of 401 kyr in contrast to the age resulting from astronomical tuning by Westerhold et al. (2008) due to a missing 405 kyr cycle (Hilgen et al., 2014). Considering this, we assume that no further errors have occurred while splicing.

To test the compatibility of the Fe datasets used in this study and to ensure that major errors can be excluded during splicing, we performed instantaneous frequency analyses of all records individually. Figure 3.6 shows that the previous findings can be confirmed. The evolution of instantaneous frequencies of the entire splice (Figure 3.6, top panel) is similar to those of the individual data sets (Figure 3.6, bottom panel).

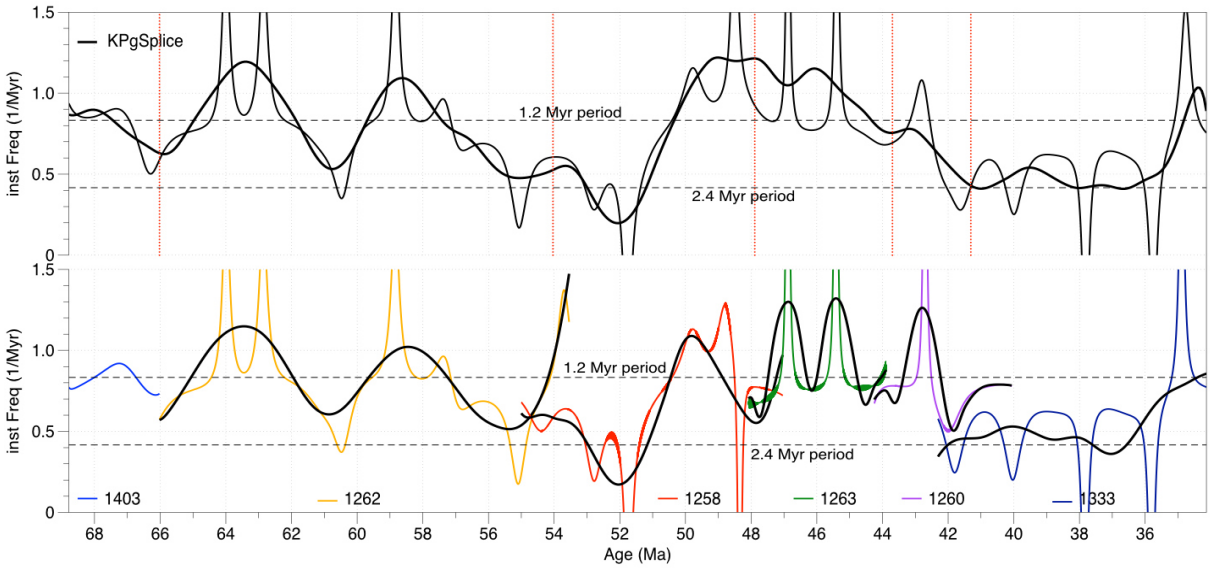

Figure 3.6: Instantaneous frequencies of the K/Pg-Splice (top panel) with trend line and splice points highlighted as vertical lines (for splice points see Figure 3.2). Bottom panel: Instantaneous Frequencies of individual datasets with small overlaps and individual LOESS trend lines. The trend lines were estimated on short datasets and have a different shape compared to the long splice, but the instantaneous frequencies are similar.

3.5.3. Frequency analyses

The frequency analyses were conducted on short eccentricity amplitude modulation. In Reinelt et al. (2019, in review), we performed several tests following Zeeden et al. (2018) to determine the optimal filter settings for the extraction of short eccentricity and its amplitudes. In order to focus only on relevant frequencies, we filtered the amplitude modulation of the short eccentricity cycle between 1/3500 and 1/800 kyr. These filter settings could be a source of bias, as possible $2(g_4 - g_3)$ periods lower than 800 kyr and $g_4 - g_3$ periods higher than 3500 kyr were excluded.

Between the trends of NAFF and instantaneous frequencies, a noticeable phase shift appears in time, despite several settings for NAFF, including adjustments on window size, detrending order and step size. A possible reason is that the sharp peaks of instantaneous frequencies pull the LOESS trend line towards lower (~1.2 Myr) periods, and without the peaks the progression would probably be consistent. Again, we emphasize that instantaneous frequencies should be interpreted carefully especially where amplitudes are low, to avoid misinterpretation. However, the comparison with

the demodulated short eccentricity shows that between ~44 – 52 Ma, ~56 – 60 Ma and at ~62 – 66 Ma a shortened cyclicity in the eccentricity and obliquity amplitudes could be confirmed (Figure 3.3). On this account we regarded these intervals for further analyses.

3.5.4. Amplitude analyses

For amplitude investigations we focused on possible resonance intervals identified by frequency analyses. As the interval between 56 and 66 Ma does not contain any obliquity signal, the analyses could only be base on eccentricity. The shift between ~56 – 60 Ma could not be confirmed as the EHA spectrum does not indicate a switch into a ~1.2 Myr period, and such an interpretation is not supported by eccentricity amplitude modulation and additional $g_4 - g_3$ and $2(g_4 - g_3)$ filters. The resonance switch during the 63/64 and ~66 Ma interval may be defined as a resonance transition, in both EHA spectrum and short and long eccentricity amplitude modulation. However, it should be noted that periodicities are not well recognizable in the EHA spectrum. Furthermore, the extraction of relevant periods from long eccentricity involves uncertainties, and consequently, the combination of long and short eccentricity amplitude modulation is not particularly reliable.

The analyses of the interval between ~44 and ~52 Ma could partly rely on obliquity in addition, which ensures a robust interpretation. Definite changes between a ~2.4 Myr period to a ~1.2 Myr period could be identified in obliquity and short eccentricity amplitude modulations and in also the EHA spectrum (Figure 3.4). The amplitude of long eccentricity is quite low during that time interval, consisting of Fe datasets of Site 1263 and Site 1258. Regarding the original data sets, we note that the Fe signal of these 2 datasets are even or lower than other datasets used for this splice (see Supplement Figure B1). Except for Site 1258, obliquity is not prominently present in the Paleocene and early Eocene, which is most likely due to minimal polar ice volumes and an overall low obliquity component in global climate variations during this time interval. As glaciated high-latitudes are known to be predominantly sensitive to obliquity (Berger and Loutre, 1994; Littler et al., 2014; Westerhold et al., 2017), this is not surprising.

3.5.5. Filter settings and amplitude modulation

As mentioned above, we used most reliable filter settings for short eccentricity determined by detailed tests. The filter boundaries for long eccentricity were chosen to filter g_3 - g_4 and $2(g_4$ - $g_3)$ components directly. To achieve this, we needed a broad filter with a minimum of noise, so we filtered between 280 and 630 kyr, which excludes even shorter periods. In order to comprise up to 800 kyr $2(g_4$ - $g_3)$ periods, the filter boundaries should be at 270 and 823 kyr, which would include more noise. Consistent analyses should be only conducted compared to short eccentricity and/or obliquity as precaution.

The combination of the demodulated long eccentricity and short eccentricity amplitude, which was meant to be supportive, became precarious due to the uncertainty of long eccentricity filtering. Furthermore, it is impossible to detect nodes and maxima of relevant periods in the output of demodulated cycles. However, filtering g_3 - g_4 and $2(g_4$ - $g_3)$ periods separately have proven to be particularly helpful, as comparing the amplitudes are of great assistance to identify the transition by investigating the specific ratio patterns.

3.5.6. Comparison with astronomical solutions

In order to better compare the development of frequencies, Multitaper Thomson (Thomson, 1982) evolutive spectra were calculated for various established astronomical solutions and the K/Pg-Splice (Figure 3.5). The red bordered boxes indicate resonance transitions at ~44 – 52 Ma and 63 – 66 Ma detected in the K/Pg-Splice, supported by previous frequency and amplitude analyses. The higher frequencies shown at e.g. ~40 Ma, and also during the interval between 52 and 63 Ma, weren't recognised in former frequency analyses (see Figure 3.3) nor confirmed by amplitude analyses (see Figure 3.4) and could maybe result from harmonics. Investigating the evolution of frequencies by means of Multitaper evolutive spectra is supportive, as the resonance transitions are well recognizable in the solutions (blue bordered boxes). For direct comparison, please see the resonance arguments $\theta = (s4 - s3) - 2(g_4 - g_3)$ for the different solutions in Figure 12 of Laskar et al. (2011a) and (Zeebe, 2017).

The resonance transitions between ~62 and ~66 Ma and between ~44 and ~52 Ma detected in the K/Pg-Splice occur at the same time as the transitions of La2010d (63

– 66 Ma) and La2010a (45 – 50 Ma). The conclusion of this comparison is consistent with the statements of (Boulila et al., 2012) and (Westerhold et al., 2012), that La2010d is best constrained in comparison with geological data. Additionally, multiple proxy analyses of Westerhold et al. (2017) show a very good match between geological data and the La2010b and La2010c solutions, which also supports the findings. Summing up, it should be noted, that La2010d match best with geological data, while La2010a is also consistent with the here analysed data before ~50 Ma regarded back in time.

3.6. Conclusion

Applying thoroughly tested methods, we searched for imprints of astronomical chaos in geological records of the Eocene, the Paleocene and the upper Late Cretaceous. As one manifestation of astronomical chaos should be detectable in the evolution of $g_4 - g_3$ and $2(g_4 - g_3)$ in eccentricity and obliquity amplitude modulation, a long and continuous dataset is essential. We used a high-resolution XRF splice consisting of seven datasets from seven different ODP/IODP Sites. For compatibility, all datasets were detrended and normalised before splicing. Applying the approach of Reinelt et al. (2019, *in review*), fundamental and instantaneous frequency analyses indicate intervals with resonance changes from $g_4 - g_3$ to $2(g_4 - g_3)$ periods, which were then addressed to further amplitude investigations. As, except for Site 1258, obliquity is not present in Paleocene and Eocene data considered here, reliable interpretations could only be conducted on short eccentricity, and long eccentricity with restrictions. Although individual methods have constraints (Reinelt et al., 2019, *in review*), the combination of the applied techniques and the additional filtering of $g_4 - g_3$ and $2(g_4 - g_3)$ periods is immensely supportive for a robust interpretation. We could confirm the reported evidence for a chaotic transition between ~44 and ~52 Ma (Westerhold et al., 2017) and detected a further transition between ~63 and ~66 Ma. Compared with astronomical solutions, it should be noted that La2010a and La2010d match best with here analysed geological data.

3.7. Acknowledgements

M.R., M.M. and H.P. were funded by the European Research Council Consolidator Grant Earth Sequencing (grant agreement 617462).

3.8. References

Berger, A.&, Loutre, M.F., 1994. Astronomical forcing through geological time, in: Orbital Forcing and Cyclic Sequences (IAS Special Publication), P. L. de Boer and D. G. Smith, Eds. pp. 15–24.

Boulila, S., Galbrun, B., Laskar, J., Pälike, H., 2012. A ~9myr cycle in Cenozoic δ 13C record and long-term orbital eccentricity modulation: Is there a link? Earth Planet. Sci. Lett. 317–318, 273–281. https://doi.org/10.1016/j.epsl.2011.11.017

Cleveland, W.S., 1979. Robust Locally Weighted Regression and Smoothing Scatterplots. J. Am. Stat. Assoc. 74, 829. https://doi.org/10.2307/2286407

Clyde, W.C., Ramezani, J., Johnson, K.R., Bowring, S.A., Jones, M.M., 2016. Direct high-precision U-Pb geochronology of the end-Cretaceous extinction and calibration of Paleocene astronomical timescales. Earth Planet. Sci. Lett. 452, 272–280. https://doi.org/10.1016/j.epsl.2016.07.041

Emery, L., Borland, M., Shang, H., Soliday, R., 2008. User ' s Guide for SDDS-compliant EPICS Toolkit Version 1 . 5.

Fang, Q., Wu, H., Hinnov, L.A., Jing, X., Wang, X., Jiang, Q., 2015. Geologic evidence for chaotic behavior of the planets and its constraints on the third-order eustatic sequences at the end of the Late Paleozoic Ice Age. Palaeogeogr. Palaeoclimatol. Palaeoecol. 440, 848–859. https://doi.org/10.1016/j.palaeo.2015.10.014

Fienga, A., Laskar, J., Kuchynka, P., Manche, H., Desvignes, G., Gastineau, M., Cognard, I., Theureau, G., 2011. The INPOP10a planetary ephemeris and its applications in fundamental physics. Celest. Mech. Dyn. Astron. 111, 363–385.

Fienga, A., Laskar, J., Morley, T., Manche, H., Kuchynka, P., Poncin-Lafitte, C. Le, Budnik, F., Gastineau, M., Somenzi, L., 2009. INPOP08, a 4-D planetary ephemeris: From asteroid and time-scale computations to ESA Mars Express and Venus Express contributions. https://doi.org/10.1051/0004-6361/200911755

Fienga, A., Manche, H., Laskar, J., Gastineau, M., 2006. INPOP06: A new planetary ephemeris. Proc. Int. Astron. Union 2, 471. https://doi.org/10.1017/S1743921307011465

Fienga, A., Manche, H., Laskar, J., Gastineau, M., Verma, A., 2014. INPOP new release: INPOP13b. ArXiv e-prints 423.

Friedrich, O., Batenburg, S.J., Moriya, K., Voigt, S., Cournède, C., Möbius, I., Blum, P., Bornemann, A., Fiebig, J., Hasegawa, T., Hull, P.M., Norris, R.D., Röhl, U., Westerhold, T., Wilson, P.A., 2016. Maastrichtian carbon isotope stratigraphy and cyclostratigraphy of the Newfoundland Margin (Site U1403, IODP Leg 342). Clim. Past Discuss. 1–21. https://doi.org/10.5194/cp-2016-51

Gradstein, F.M., Ogg, J.G., Schmitz, M.D., Ogg, G.M., 2012. The Geologic Time Scale 2012. https://doi.org/10.1016/B978-0-444-59425-9.01001-5

Hilgen, F.J., Abels, H.A., Kuiper, K.F., Lourens, L.J., Wolthers, M., 2014. Towards a stable astronomical time scale for the Paleocene: Aligning Shatsky Rise with the Zumaia – Walvis Ridge ODP Site 1262 composite. Newsletters Stratigr. 48, 91–

110. https://doi.org/10.1127/nos/2014/0054
Hilgen, F.J., Hinnov, L.A., Abdul Aziz, H., Abels, H.A., Batenburg, S., Bosmans, J.H.C., de Boer, B., Hüsing, S.K., Kuiper, K.F., Lourens, L.J., Rivera, T., Tuenter, E., Van de Wal, R.S.W., Wotzlaw, J.-F., Zeeden, C., 2015. Stratigraphic continuity and fragmentary sedimentation: the success of cyclostratigraphy as part of integrated stratigraphy. Geol. Soc. London, Spec. Publ. 404, 157–197. https://doi.org/10.1144/SP404.12
Hilgen, F.J., Lourens, L.J., Van Dam, J.A., Beu, A.G., Boyes, A.F., Cooper, R.A., Krijgsman, W., Ogg, J.G., Piller, W.E., Wilson, D.S., 2012. The Neogene Period, The Geologic Time Scale 2012. Elsevier. https://doi.org/10.1016/B978-0-444-59425-9.00029-9
Hinnov, L.A., 2018. Cyclostratigraphy and Astrochronology in 2018, Stratigraphy & Timescales. Elsevier Ltd. https://doi.org/10.1016/bs.sats.2018.08.004
Hinnov, L.A., 2013. Cyclostratigraphy and its revolutionizing applications in the earth and planetary sciences. Bull. Geol. Soc. Am. 125, 1703–1734. https://doi.org/10.1130/B30934.1
Hinnov, L.A., 2000. New Perspectives on orbitally forced Stratigraphy 12, 727–732. https://doi.org/10.1177/0741713604268894
Hinnov, L.A., Hilgen, F.J., 2012. Cyclostratigraphy and Astrochronology. Geol. Time Scale 2012 1–2, 63–83. https://doi.org/10.1016/B978-0-444-59425-9.00004-4
Hinnov, L.A., Schulz, M., Yiou, P., 2002. Interhemispheric space-time attributes of the Dansgaard-Oeschger oscillations between 100 and 0 ka. Quat. Sci. Rev. 21, 1213–1228. https://doi.org/10.1016/S0277-3791(01)00140-8
Laskar, J., 2003. Frequency map analysis and quasiperiodic decompositions. https://doi.org/10.1109/PAC.2003.1288929
Laskar, Jacques, 1999. The limits of Earth orbital calculations for geological time-scale use. Philos. Trans. R. Soc. A Math. Phys. Eng. Sci. 357, 1735–1759. https://doi.org/10.1098/rsta.1999.0399
Laskar, J., 1999. Introduction to Frequency Map Analysis, in: Simó C. (Eds) Hamiltonian Systems with Three or More Degrees of Freedom. NATO ASI Series. pp. 134–150. https://doi.org/10.1007/978-94-011-4673-9_13
Laskar, J., 1990. The chaotic motion of the solar system: A numerical estimate of the size of the chaotic zones. Icarus 88, 266–291. https://doi.org/10.1016/0019-1035(90)90084-M
Laskar, J., Fienga, A., Gastineau, M., Manche, H., 2011a. La2010: A new orbital solution for the long term motion of the Earth 4. https://doi.org/10.1051/0004-6361/201116836
Laskar, J., Gastineau, M., Delisle, J.-B., Farrés, A., Fienga, A., 2011b. Strong chaos induced by close encounters with Ceres and Vesta. Astron. Astrophys. 532, L4. https://doi.org/10.1051/0004-6361/201117504
Laskar, J., Robutel, P., Joutel, F., Gastineau, M., Correia, A.C.M., Levrard, B., 2004. A long-term numerical solution for the insolation quantities of the Earth. Astron. Astrophys. 428, 261–285. https://doi.org/10.1051/0004-6361:20041335

Littler, K., Röhl, U., Westerhold, T., Zachos, J.C., 2014. A high-resolution benthic stable-isotope record for the South Atlantic: Implications for orbital-scale changes in Late Paleocene-Early Eocene climate and carbon cycling. Earth Planet. Sci. Lett. 401, 18–30. https://doi.org/10.1016/j.epsl.2014.05.054

Ma, C., Meyers, S.R., Sageman, B.B., 2019. Testing Late Cretaceous astronomical solutions in a 15 million year astrochronologic record from North America. Earth Planet. Sci. Lett. 513, 1–11. https://doi.org/10.1016/j.epsl.2019.01.053

Ma, C., Meyers, S.R., Sageman, B.B., 2017. Theory of chaotic orbital variations confirmed by Cretaceous geological evidence. Nature 542, 468–470. https://doi.org/10.1038/nature21402

Martinez, M., Kotov, S., De Vleeschouwer, D., Pas, D., Pälike, H., 2016. Testing the impact of stratigraphic uncertainty on spectral analyses of sedimentary series. Clim. Past 12, 1765–1783. https://doi.org/10.5194/cp-12-1765-2016

Meyers, S.R., 2014. Astrochron: An R Package for Astrochronology.

Olsen, P.E., Laskar, J., Kent, D. V., Kinney, S.T., Reynolds, D.J., Sha, J., Whiteside, J.H., 2019. Mapping Solar System chaos with the Geological Orrery. Proc. Natl. Acad. Sci. 201813901. https://doi.org/10.1073/PNAS.1813901116

Pälike, H., Laskar, J., Shackleton, N.J., 2004. Geologic constraints on the chaotic diffusion of the solar system. Geology 32, 929–932. https://doi.org/10.1130/G20750.1

Pälike, H., Shackleton, N.J., Röhl, U., 2001. Astronomical forcing in Late Eocene marine sediments. Earth Planet. Sci. Lett. 193, 589–602. https://doi.org/10.1016/S0012-821X(01)00501-5

R, D.C.T., 2016. R: A Language and Environment for Statistical Computing. R Found. Stat. Comput. https://doi.org/10.1007/978-3-540-74686-7

Röhl, U., Ogg, J.G., Geib, T.L., Wefer, G., 2001. Astronomical calibration of the Danian time scale. West. North Atl. Palaeogene Cretac. Palaeoceanography 183, 163–184. https://doi.org/10.1144/GSL.SP.2001.183.01.09

Shackleton, N.J., Hagelberg, T., Crowhurst, S.J., 1995. Evaluating the success of astronomical tuning: Pitfalls of using coherence as a criterion for assessing pre-Pleistocene timescales. Paleoceanography 10, 693–697. https://doi.org/10.1029/95PA01454

Taner, M.T., Koehler, F., Sheriff, R.E., 1979. Complex seismic trace analysis. Geophysics 44, 1041–1063. https://doi.org/10.1190/1.1440994

Thomson, D.J., 1982. Spectrum Estimation and Harmonic Analysis 70.

Vakman, D., 1996. On the analytic signal the teager-kaiser energy algorithm and other methods for defining amplitude and frequency. IEEE Trans. Signal Process. 44, 791–797. https://doi.org/10.1109/78.492532

Westerhold, T., Röhl, U., 2013. Orbital pacing of Eocene climate during the Middle Eocene Climate Optimum and the chron C19r event: Missing link found in the tropical western Atlantic. Geochemistry, Geophys. Geosystems 14, 4811–4825. https://doi.org/10.1002/ggge.20293

Westerhold, T., Röhl, U., Frederichs, T., Agnini, C., Raffi, I., Zachos, J.C., Wilkens,

R.H., 2017. Astronomical Calibration of the Ypresian Time Scale: Implications for Seafloor Spreading Rates and the Chaotic Behaviour of the Solar System? Clim. Past Discuss. 1–34. https://doi.org/10.5194/cp-2017-15

Westerhold, T., Röhl, U., Laskar, J., 2012. Time scale controversy: Accurate orbital calibration of the early Paleogene. Geochemistry, Geophys. Geosystems 13, 1–19. https://doi.org/10.1029/2012GC004096

Westerhold, T., Röhl, U., Laskar, J., Raffi, I., Bowles, J., Lourens, L.J., Zachos, J.C., 2007. On the duration of magnetochrons C24r and C25n and the timing of early Eocene global warming events: Implications from the Ocean Drilling Program Leg 208 Walvis Ridge depth transect. Paleoceanography 22, 1–19. https://doi.org/10.1029/2006PA001322

Westerhold, T., Röhl, U., Pälike, H., Wilkens, R., Wilson, P.A., Acton, G., 2014. Orbitally tuned timescale and astronomical forcing in the middle Eocene to early Oligocene. Clim. Past 10, 955–973. https://doi.org/10.5194/cp-10-955-2014

Westerhold, T., Röhl, U., Raffi, I., Fornaciari, E., Monechi, S., Reale, V., Bowles, J., Evans, H.F., 2008. Astronomical calibration of the Paleocene time. Palaeogeogr. Palaeoclimatol. Palaeoecol. 257, 377–403. https://doi.org/10.1016/j.palaeo.2007.09.016

Zeebe, R.E., 2017. Numerical Solutions for the orbital motion of the Solar System over the Past 100 Myr: Limits and new results. Astron. J. 154, 193. https://doi.org/10.3847/1538-3881/aa8cce

Zeeden, C., Kaboth, S., Hilgen, F.J., Laskar, J., 2018. Taner filter settings and automatic correlation optimisation for cyclostratigraphic studies. Comput. Geosci. 119, 18–28. https://doi.org/10.1016/j.cageo.2018.06.005

Zeeden, C., Meyers, S.R., Lourens, L.J., Hilgen, F.J., 2015. Testing astronomically tuned age models. Paleoceanography 30, 369–383. https://doi.org/10.1002/2014PA002762

Chapter 4

Testing astronomical transitions in the Mesozoic with improved methodologies

Melanie Reinelt[1], Christian Zeeden[2], Heiko Pälike[1]

[1]MARUM - Center for Marine Environmental Sciences, University of Bremen, Leobener Str. 8, 28359 Bremen, Germany
[2]LIAG - Leibniz Institute for Applied Geophysics, GEOZENTRUM HANNOVER, Stilleweg 2, 30655 Hannover

Abstract

Cyclic orbital variations control insolation and climate on Earth. Astronomically driven cycles recorded in sediments are used to establish and support age models. Such age models are often adjusted to astronomical solutions, which are integrations of modern (initial) conditions of the solar system back in time. However, due to the chaotic behaviour of the solar system, the duration over which Earth's orbital variations can be computed with confidence is limited. One manifestation of astronomical chaos is the change of two resonant astronomical frequencies of Mars' and Earth's orbit and should be detectable in the evolution of $g_4 - g_3$ and $2(g_4 - g_3)$ periods in eccentricity and obliquity amplitude modulation in the geological record. For this purpose, we developed several methods for detecting such transitions. We combined complex frequency analyses with traditional amplitude modulation of eccentricity and obliquity. We filtered ~2.4 Myr ($g_4 - g_3$) and ~1.2 Myr $2(g_4 – g_3)$ periods from amplitude modulation for further amplitude investigations. Here we intend to apply and test these methods on various type of data and two studies reporting indications for astronomical chaos: Sonic velocity and natural gamma radiation borehole logs of the Triassic-Jurassic (199 – 223 Ma) proposing a $g_4 – g_3$ period of 1.747 Myr, which could be an evidence for a chaotic transition somewhere between ~50 and 200 Ma and Formation Micro-Resistivity Imaging and $\delta^{13}C$ datasets of the Late Cretaceous (82 - 97 Ma), where two adjacent chaotic transitions have been detected. Applying our methods, we could confirm these findings.

4.1. Introduction

Cyclostratigraphy, together with other (standard) stratigraphic methods, is used to construct geological time scales (e.g Gradstein et al., 2012; Hilgen et al., 2012; Hinnov and Hilgen, 2012). In this context, theoretical astronomical models serve as templates for establishing tuned time scales. However, the solar system is chaotic which makes it impossible to extrapolate astronomical models from recent initial conditions. In addition, the close encounters of the orbits of Ceres and Vesta induce a strong chaos and influences the calculation of Earth's eccentricity (Laskar et al., 2011b). A major contribution to the chaotic motion of the solar system manifests itself in resonance changes of the secular (fundamental) frequencies between Mars and Earth. A combination of fundamental frequencies of Mars' and Earth's orbit expressed in $(g_4 - g_3) - 2(s_4 - s_3)$ oscillate at present at 0, in libration motion. But this motion can evolve into circular and even more into libration motion. During the circular motion, the expression $(g_4 - g_3) - 2(s_4 - s_3) = 0$ changes into $(g_4 - g_3) - (s_4 - s_3) = 0$. This implies a change from a 2:1 resonance into a 1:1 (Laskar, 1999). The result is a missing $(g_4 - g_3)$ frequency term in obliquity, and in eccentricity the expression $g_4 - g_3$ changes into $2(g_4 - g_3)$. The timing of such resonance shift(s) has been predicted to occur sometime between 50 and 100 Myr ago (Laskar, 1990; Laskar et al., 2004) and should be observable in the cyclostratigraphical record by investigating amplitude modulation patterns of eccentricity and obliquity. The challenge is to detect astronomical chaos in geological data in order to verify and extend astronomical models. In Reinelt et al. (2019, in review), we developed and tested several techniques to search for signatures of chaotic transitions in geological data. Now we intend to examine data from two recent studies reporting evidences for astronomical chaos to further test our advanced methods.

Using the Geological Orrery, a network of orbital records, Olsen et al. (2019) analysed Triassic-Jurassic (199 – 223 Ma) lacustrine and fluvial sediments of the Newark and Hartford Basins and the Colorado Plateau, North America. A composite geologic record was tuned with the help of U–Pb ages of three interbedded lava intrusions and the 405 kyr eccentricity 'McLaughlin Cycle' of the Colorado Plateau (Olsen et al., 1996). With spectral (Multitaper Method and Wavelet) and fundamental frequency analyses they detected a 1.747 Myr $g_4 - g_3$ eccentricity period between 199 and 223 Ma,

matching the La2010d eccentricity solution (Laskar et al., 2011). This shortened g_4 - g_3 period was specified to represent a fingerprint of solar system chaos. To examine the evolution of the grand eccentricity cycle with a current period of ~2.4 Myr ($g_4 – g_3$), they performed frequency analyses of La2004 (Laskar et al., 2004) and La2010 (Laskar et al., 2011) of the last 250 Ma and stated that the fundamental frequencies calculated from Newark-Hartford core data match the secular frequencies of the orbital motion and this makes the detection of a 1.747 Myr g_4 - g_3 period convincing.

Two chaotic events have been detected in the Late Cretaceous in North American Libsack (82 - 90 Ma) and Iona (90 - 97 Ma) cores. Ma et al. (2017) reported the evidence for one 1:1 resonance transition in Formation Micro-Resistivity Imaging (FMI) data, a proxy for carbonate content, of the Libsack core between 84 and 88 Ma. Later, they extended their assessment using grayscale and $\delta^{13}C$ data of the Iona core (Eldrett et al., 2015) in order to investigate, whether a 2:1 resonance was present in the solar system before this transition (Ma et al., 2019). When investigating amplitude modulation and the integration of high-precision radioisotope data, they discovered another transition between 89 and 93 Ma. They used an astronomically-tuned $\delta^{13}C$ composite of the Iona and Libsack/Angus for evaluation. Although the $\delta^{13}C$ values differ from the standard curve of the English Chalk and comparing the Colorado and Texas carbon isotope curves reveals some discrepancies in the timing of carbon isotopic events, they regarded the Iona and Libsack/Angus records as compatible. They state, that cyclicity is not affected by radioisotopic anchoring.

4.2. Material

As we intend to test our approach on preferably various type of data, we selected the sonic velocity and (natural) gamma radiation borehole measurements of the Newark–Hartford plateau (Olsen et al., 2019) and Formation Micro-resistivity Imaging data of the Libsack core (Ma et al., 2017). In addition, we used $\delta^{13}C$ data of the Iona core (Eldrett et al., 2015; Ma et al., 2019) to investigate the applicability for bulk stable isotope data.

High-resolution geophysical datasets like FMI reflect depositional rhythms in centimetre scale and can record possible orbital influences (e.g. Locklair & Sageman 2008). The Newark and Hartford Basin rift lake sediments are paced by orbital cycles.

The cementation expressed in sonic parameters reflect precessional variability, but also reveal eccentricity components with periods of $g_4 - g_3$ (~2.4 Myr recently) and $g_1 - g_5$ (~900 kyr) and $g_2 - g_1$ (~700 kyr) (Olsen et al., 2019).

4.3. Methods

We followed the approach of Reinelt et al. (2019, in review) and performed fundamental and instantaneous frequency analyses combined with amplitude investigations of eccentricity and obliquity for the identification of resonance transitions. We extracted 2.4 Myr and (possible) 1.2 Myr cycles from eccentricity and obliquity amplitude modulation and look for a distinct pattern characterised by an increase in amplitude of the 1.2 Myr cycle during a chaotic transition while the amplitude of the 2.4 Myr cycle falls to zero.

We determined the optimal upper and lower frequencies for Taner filtering (Taner et al., 1979) for the best extraction of astronomical (interference) signals and the optimal roll-off rate (steepness of filter) of 10^{10}. Long (~405 kyr) eccentricity frequency was filtered between 1/630 and 1/280 kyr, short (~100 kyr) eccentricity between 1/160 and 1/85 kyr and obliquity between 1/54 and 1/35 kyr. We extracted $g_3 - g_4$ and possible $2(g_3 - g_4)$ periods separately (~2.4 Myr cycles as filtered between 1/3500 kyr and 1/1800 kyr and ~1.2 Myr cycles as filtered from 1/1800 kyr to 1/800 kyr). The used R script for filtering is available in supplementary material.

4.3.1. Frequency analyses

To determine the fundamental frequencies of a signal with Laskar's Numerical Analysis of Fundamental Frequencies (NAFF) algorithm (Laskar, 2003), we used a Swift language implementation based on the SDDS (Self Describing Data Sets) Toolkit Version 3.5.1 (Emery et al., 2008) for Fortran:
https://paloz.marum.de/confluence/display/ESPUBLIC/NAFF).

The algorithm calculates a list of all fundamental frequency terms using a moving window approach with a window size of 3000 kyr and time steps of 100 kyr. Each window was detrended by polynomial regression (here order of 2) before further analysis. The application results in a list containing the columns frequency, amplitude, phase, significance and period, starting from t0 of each window and is sorted within the windows by decreasing amplitude. We analysed the demodulated short eccentricity

signal. The frequency range we focus on only includes possible resonance changes from (g_4 – g_3) to 2(g_4 - g_3) frequencies. Therefore, we filtered short eccentricity amplitude modulation between 1/3500 kyr and 1/800 kyr.

The instantaneous frequencies were calculated from the amplitude envelope of short eccentricity filtered between 1/3500 kyr and 1/800 kyr in 1 kyr time steps. The fundamental frequency terms of short eccentricity producing the g_4 – g_3 beat term period of ~2.4 Myr are (g_4 – g_5) – (g_3 –g_5) and (g_4 – g_2) – (g_3 – g_2). Since filtering and demodulation short eccentricity includes the g_3 and g_4 frequencies directly, short eccentricity amplitude modulation is best suited to investigate resonance changes from g_4 – g_3 to 2(g_4 – g_3). Hilbert transformation extracts instantaneous frequency, amplitude and phase of a signal. From a time dependent amplitude A(t) and a time-dependent phase (t) of a signal $f(t) = A(t)\, cos\, \theta(t)$, the time-dependent (instantaneous) frequency (t) is calculated by the rate of change of the time-dependent phase. $\omega(t) = \frac{d\theta(t)}{dt}$ (e.g. Taner et al., 1979; Vakman, 1996; Hinnov et al., 2002).

4.3.2. Amplitude analyses

Exclusively when previous frequency analyses indicated resonance transition(s), we conducted amplitude investigations for the specific time interval (and per dataset). We firstly performed Evolutive harmonic analyses (EHA) using the ‘eha’ function provided in the “astrochron” package (Meyers, 2014) for R (R Core Team, 2016) with a time step of 1 kyr and a window size of 500 kyr, padded to 5000 data points on δ^{13}C Iona and FMI Libsack data. Linear trends and mean values were removed from each window before analysis. Secondly we extracted short and long eccentricity and obliquity by Taner band-pass filtering (Taner et al., 1979) using above mentioned filter boundaries. Hilbert transformation calculated the instantaneous amplitude modulation of each cycle. From demodulated cycles we filtered g_4 – g_3 (2.4 Myr) and possible 2(g_4 – g_3) (1.2 Myr) periods for further amplitude investigations. We combined the amplitude modulations of long and short eccentricity amplitude which leads to an amplification of the signal (see Figure 4.4, ‘combined eccentricity AM’). During a resonance transition, long and short eccentricity amplitude modulation should express the change of g_4 – g_3 into 2(g_4 - g_3), with an opposite phase. In obliquity, the expression g_4 – g_3 (2.4 Myr)

should be missing during transitions, while the s_4 - s_3 (1.2 Myr) term remains (Laskar, 1990; Hinnov, 2000, 2013).

4.4. Results

4.4.1. Frequency analyses

Fundamental and instantaneous frequencies for all datasets are presented in figures 4.1 and 4.2, including a direct comparison to the short eccentricity amplitude - filtered between 1/3500 and 1/800 kyr.

The results for Cretaceous datasets of Iona ($\delta^{13}C$) and Libsack (FMI) cores are shown in Figure 4.1. Both frequency analyses express resonance shifts between ~84 Ma and ~88 Ma, and at ~90 – 93 Ma. The amplitude of short eccentricity (red line at top of Figure 4.1) displays a weak signal and a shortened cyclicity (< 1.5 Myr) over the whole two investigated time intervals.

Detailed amplitude analyses were conducted for Iona and Libsack datasets in order to evaluate whether the resonance changes detected by frequency analyses are evidences for astronomical chaos (see section 3.2. Amplitude analyses).

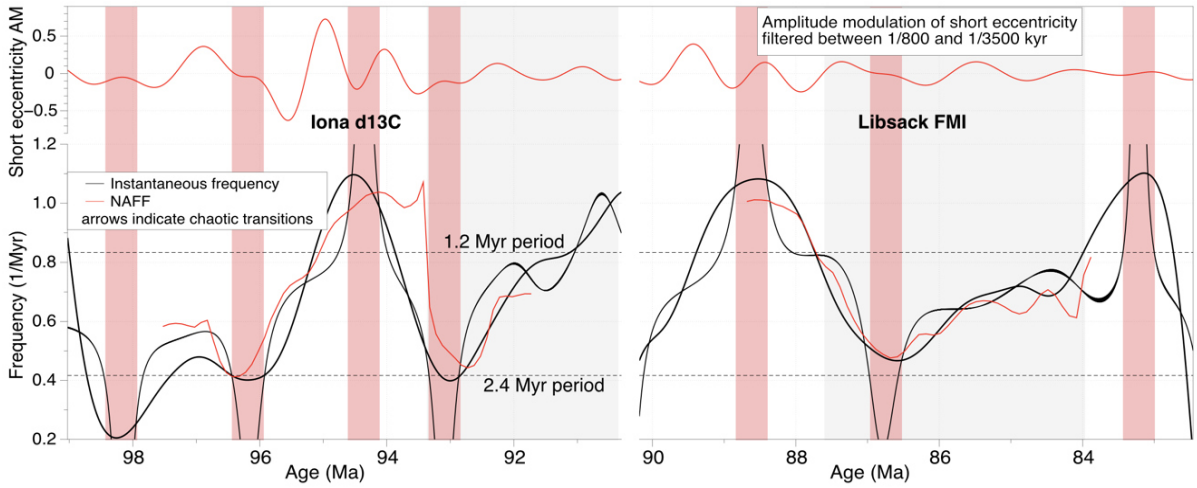

Figure 4.1 Frequency analyses of the $\delta^{13}C$ Iona core (left, ~99 - 90 Ma) and FMI Libsack core (right, ~90 – 82 Ma) applied on short eccentricity amplitude modulation. At the top: Amplitude modulation of short eccentricity filtered between 1/3500 and 1/800 kyr for both records. Below: Fundamental frequency analyses (NAFF) showing (g_4 - g_3) or 2(g_4 - g_3) frequencies (1/Myr; red) between 1/3500 and 1/800 kyr. Instantaneous frequencies (1/Myr; black) with LOESS (LOcally Estimated Scatterplot Smoothing) trend line. Dashed lines mark 2.4 Myr and 1.2 Myr periods. Resonance shifts to ~1 Myr are indicated between the sharp peaks in Libsack core at ~84 Ma and ~88 Ma, and at ~90 – 93 Ma in

Iona core. The sharp peaks in frequency are an effect of a zero amplitude (highlighted in red) and should not be regarded as indications for a transition. During intervals of resonance changes (grey boxes) the amplitude of the demodulated short eccentricity exhibits a weak signal and short cyclicity (< 1.5 Myr) over the whole time intervals.

Figure 4.2 demonstrates the results of fundamental and instantaneous frequency analyses of the Newark-Hartford datasets.

As shown in the top panel of Figure 4.2, instantaneous frequencies calculated from the gamma ray dataset show strong fluctuations. The 100 kyr amplitude modulation displays a remarkable amplitude difference between the first part of the series (from 229 to 218 Ma) and the second part (from 218 to 202 Ma). Measuring instantaneous frequencies at time-points with zero amplitude result in sharp peaks for some intervals (red marked). These are no real resonance shifts but artefacts of no amplitude. Overall the g_4 - g_3 period appears to vary between 1/0.9 (1.11 Myr) and 1/0.6 Myr (1.67 Myr) with a mean frequency of 0.82 Myr (period of ~1.22 Myr).

Both fundamental and instantaneous frequency analyses of the Newark-Hartford sonic velocity dataset calculate a g_4 - g_3 period of 1/0.9 (1.11 Myr) – 1/0.5 Myr (2 Myr) with a mean frequency of 0.62 Myr (period of ~1.62 Myr), fluctuating due to sharp frequency peaks (bottom panel of Figure 4.2). The amplitude modulation of short eccentricity (red line at the top) displays a noisy fluctuating amplitude with several intervals of a zero amplitude, which influence frequency analyses (red marked), but no indication of a resonance transition during this time interval.

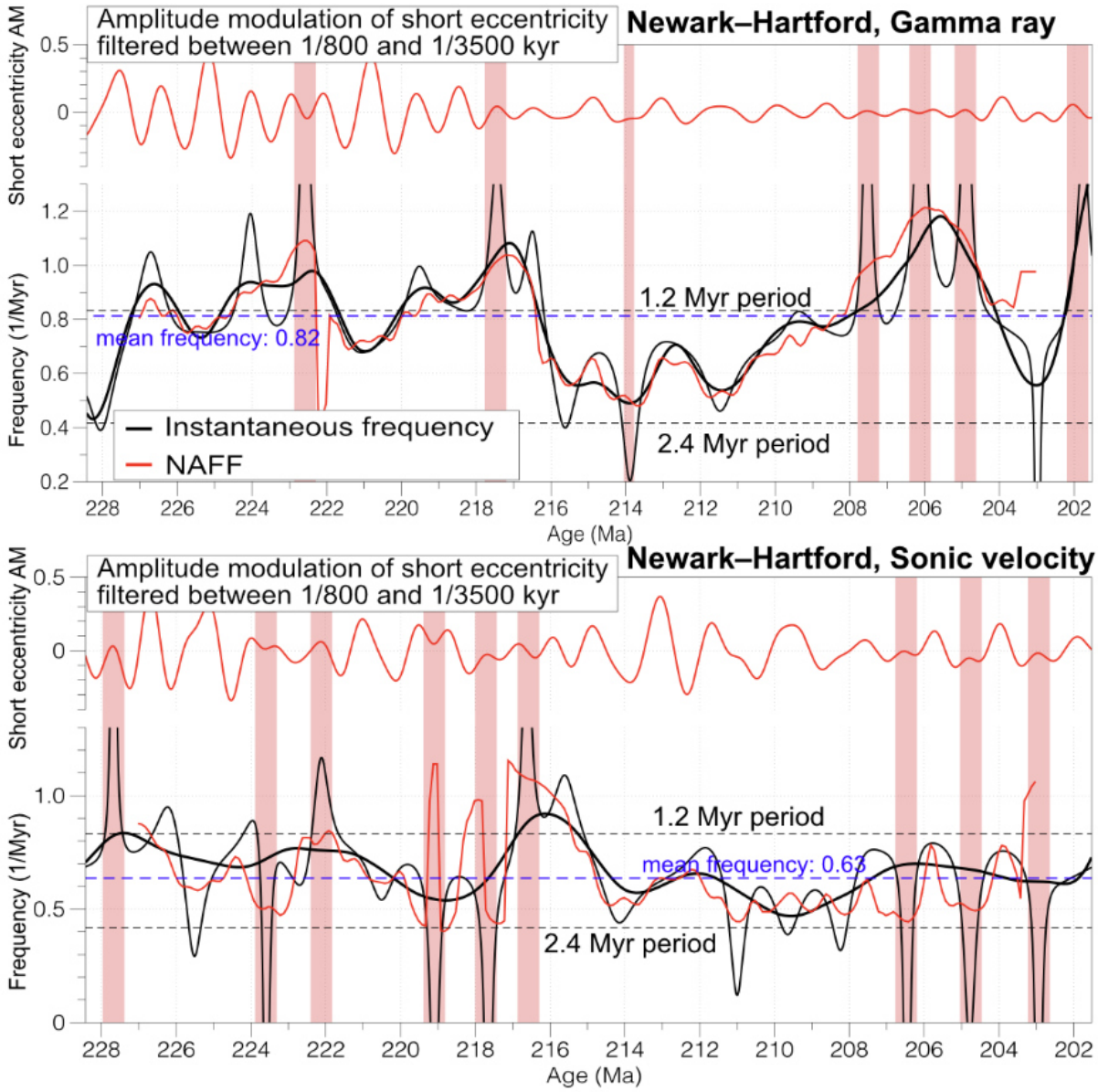

Figure 4.2 Time-evolutive frequency analyses of Newark–Hartford datasets applied on short eccentricity amplitude modulation. Top panel: gamma ray, bottom panel: sonic velocity. The red line at the top of each panel shows the amplitude modulation of short eccentricity filtered between 1/3500 and 1/800 kyr. Fundamental frequency analyses (NAFF) presenting ($g_4 - g_3$) or $2(g_4 - g_3)$ frequencies (1/Myr; red) between 1/3500 and 1/800 kyr. Instantaneous frequencies (1/Myr; black) with LOESS (LOcally Estimated Scatterplot Smoothing) trend line. Dashed lines mark 2.4 Myr and 1.2 Myr periods. Top panel, gamma ray: The demodulated short eccentricity (red line at the top) displays a weak signal between 202 and 218 Ma, and high amplitudes between 218 and 229 Ma. There are several intervals with an amplitude at zero, effecting frequency analyses (red marked). A shortened cyclicity is obvious over the whole record, also evident in short eccentricity amplitude modulation. At 210 Ma the period is around 1.2 Ma with a slight

shift to ~1/0.6 Myr afterwards and a period around 0.8 – 0.9 Myr between 218 and 227 Ma, with a mean frequency of 0.82 Myr. Bottom panel, sonic velocity: The demodulated short eccentricity (red line at the top) displays a noisy fluctuating amplitude and several intervals with an amplitude around zero, which effect frequency analyses (red marked). A $g_4 - g_3$ period of 1/0.8 (1.25 Myr) – 1/0.5 Myr (2 Myr) is observable over the whole record, with a mean frequency of 0.62 Myr.

4.4.2. Amplitude analyses: Cretaceous, FMI Libsack 82.45 - 90.183 Ma and $\delta^{13}C$ Iona 90.30 - 99.025 Ma

To evaluate previous frequency analyses, we performed complex amplitude analyses on the Iona and Libsack core datasets. We investigated short and long eccentricity amplitude modulation and their combination, obliquity amplitude modulation of the Libsack record, and additional filtered $g_3 - g_4$ and $2(g_3 - g_4)$ periods (Figure 4.3). Within the red boxes (recognised as intervals of resonance shifts in frequency analyses), ~2.4 and ~1.2 Myr cycles are highlighted, when they show an amplitude ratio suggesting a chaotic transition: The $g_4 - g_3$ amplitude falls to zero, while the amplitude of $2(g_4 - g_3)$ increases. That specific ratio is evident in long and short eccentricity amplitude modulation between ~93 – 90 Ma and in obliquity and long eccentricity amplitude modulation between ~88 – 84 Ma. Some ~1.2 Myr periods could be recognised in EHA spectrum (black markings).

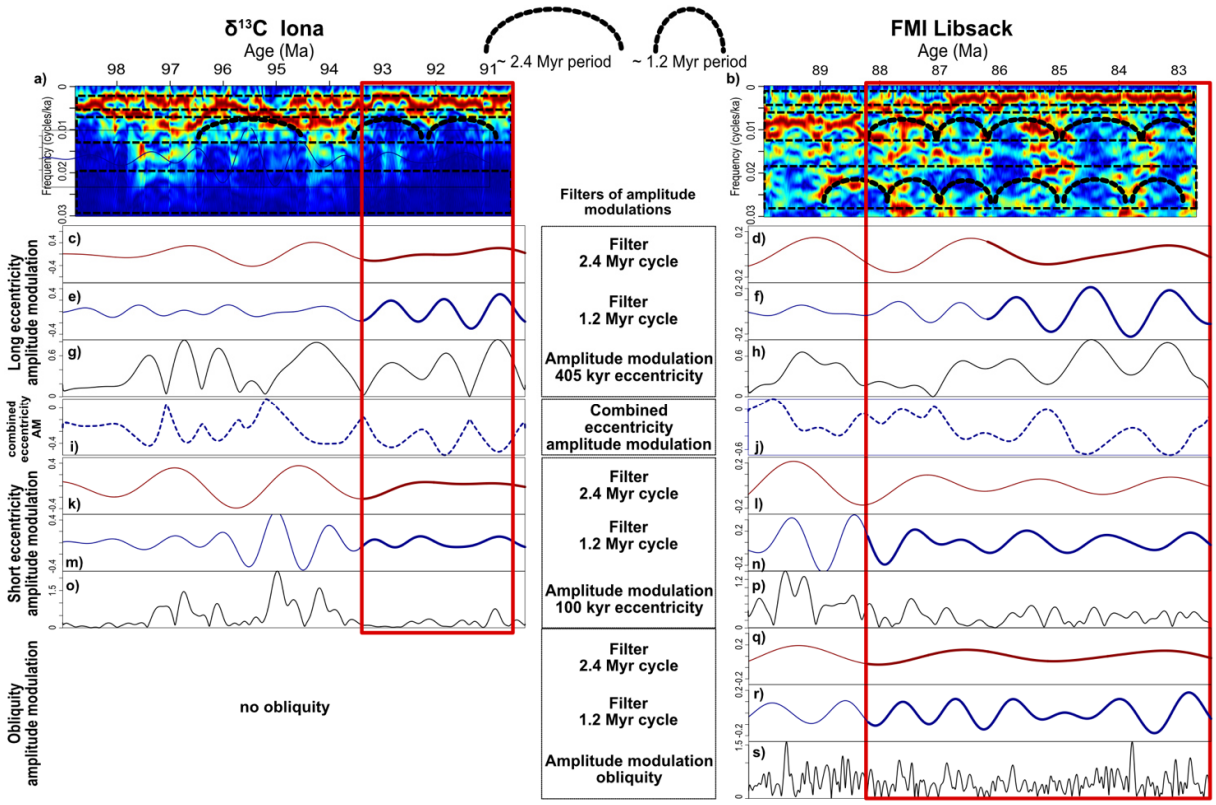

Figure 4.3 Amplitude analyses of $\delta^{13}C$ Iona 99.025 - 90.30 Ma (left) and FMI Libsack 90.183 - 82.45 Ma (right). Evolutive harmonic analyses (EHA) results are displayed at the top (a, b). Panels below show from top to bottom: Filters of long eccentricity amplitude modulation (g, h), the combined amplitude modulation of short and long eccentricity (I, j), short eccentricity (o, p) and obliquity (s) amplitude modulation together with filtered $2(g_4 - g_3)$ (1.2 Myr, dark blue: e, f, m, n, r) and $g_4 - g_3$ (2.4 Myr, dark red: c, d, k, l, q) cycles from each amplitude modulation. The red boxes represent the intervals of resonance shifts recognised by frequency analyses. The $d^{13}C$ Iona dataset lacks of obliquity imprint, but the amplitudes of short and long eccentricity indicate specific $2(g_4 - g_3)/ g_4 - g_3$ ratios during the resonance interval (marked by thick lines). During the resonance interval of FMI Libsack data (right panel) the 1.2 Myr/2.4Myr ratio is obvious in obliquity and long eccentricity amplitude modulation, with a phase shift. $2(g_4 - g_3)$ (~1.2 Myr) periods are confirmed by EHA (black markings).

4.5. Discussion

4.5.1.Filter settings and amplitude modulation

As already discussed in Reinelt et al. (2019, in review), we determined the theoretically optimal filter settings for the extraction of short eccentricity and its amplitudes following

Zeeden et al. (2018). The filter for long eccentricity was chosen to be as broad as possible to filter 2(g_4 - g_3) periods between 280 and 630 kyr.
Short eccentricity amplitude modulation was filtered between 1/3500 and 1/800 kyr to only focus on relevant frequencies. Filtering this way exclude possible 2(g_4 - g_3) periods lower than 800 kyr and g_4 - g_3 periods higher than 3500 kyr, which could be a source of errors.

4.5.2. Frequency analyses

4.5.2.1. Frequency analyses of FMI Libsack and $\delta^{13}C$ Iona

In accordance with Ma et al. (2017, 2019), both NAFF and fundamental frequency analyses calculate distinct resonance shifts between ~90 – 93 Ma in Iona and ~84 – 88 Ma in Libsack core data (Figure 4.1). Due to artefacts of a zero amplitude, sharp peaks of instantaneous frequencies pull the LOESS trend line towards lower (~1.2 Myr) periods, which especially with the short records of Iona and Libsack could may to misinterpretation. Nevertheless, taking this into account it is obvious that frequencies are getting higher during specific intervals and the demodulated short eccentricity (red line at top of Figure 4.1) confirms a shortened cyclicity (~1.2 Myr).

4.5.2.2. Frequency analyses of Newark–Hartford

The results of frequency analyses of gamma radiation and sonic velocity datasets agree with Olsen et al. (2019). NAFF and fundamental frequency analyses show an average shortened cyclicity between 202 and 220 Ma with a frequency range of 1/0.8 (1.25 Myr) – 1/0.5 Myr (2 Myr). The average g_4 - g_3 periods of the examined datasets vary between 1.22 Myr for gamma radiation and 1.62 Myr for sonic velocity measurements, while the lower 1.22 Myr mean period of gamma radiation may be induced by the high amount of artefact peaks.
There is no indication for a transition within this time interval. As mentioned above, some artefact peaks distort the progression of instantaneous frequencies. The shortened g_4 - g_3 period could be an evidence for the chaotic behaviour of the solar system and a chaotic transition somewhere between ~50 and ~200 Ma. After a resonance switch from a motion in libration to circulation and back into libration, the g_4 - g_3 (and s_4 - s_3) expression appears with a shortened period (see Figure 13 in Laskar et al., 2011).

4.5.3. Amplitude analyses of FMI Libsack and $\delta^{13}C$ Iona

The resonance intervals identified by frequency analyses were chosen for amplitude investigations. We intended to compare our interpretation with those of Ma et al. (2019).

In contrast to Ma et al. (2019), we based our analyses of the $\delta^{13}C$ Iona data only on eccentricity (left panel, Figure 4.3). Between ~90 and 93 Ma, a cyclicity of ~1.2 Myr ($2(g_4 - g_3)$) is recognisable in the EHA short eccentricity band (markings in Figure 4.3 a). This resonance change is also supported by additionally filtered $g_4 - g_3$ and $2(g_4 - g_3)$ components of short and long eccentricity amplitude modulation (thick lines, Figure 4.3, left panel) while comparing their amplitudes.

The resonance switch detected by frequency analyses between ~83 and 88 in the Libsack data (Figure 4.3, right panel) could be identified in short eccentricity and obliquity bands in the EHA spectrum (markings in Figure 4.3 b). This is also obvious while comparing the filtered $g_4 - g_3$ and $2(g_4 - g_3)$ amplitudes of obliquity and long eccentricity amplitude modulation, while the exact timing of the resonance transition differs due to the phase shift between obliquity and eccentricity (Hinnov, 2013). The filtered $g_4 - g_3$ and $2(g_4 - g_3)$ periods of short eccentricity show no significant difference in amplitude, but short periodicities in general. The combination of frequency analyses and amplitude demodulation including additional filter investigations helped to confirm the evidences for two resonance transitions between 84 and 93 Ma, as reported by Ma et al. (2019). However, it seems the transition already initiates before or at ~83 Ma, giving an additional information to the interpretation of Ma et al. (2019).

4.6. Conclusion

In order to test our methods to detect indications for astronomical chaos in geological time series, we have chosen two recent studies reporting evidences for chaotic transitions. As we intended to use various type of data, we selected sonic velocity and gamma radiation borehole measurements of the Newark–Hartford plateau (Olsen et al., 2019) and Formation Micro-resistivity Imaging and $\delta^{13}C$ data of North American Libsack and Iona cores (Ma et al., 2019). Olsen et al. (2019) discovered shorter $g_4 - g_3$ cycles of 1.747 Myr between 202 and 229 Ma, while Ma et al. (2019) detected two chaotic transitions in the Cretaceous between 84 and 93 Ma. We applied our approach

of Reinelt et al. (2019, *in review*), consisting of a combination of frequency-, filter- and amplitude analyses, on each of the datasets. Applying fundamental and instantaneous frequency analyses, we detected two intervals with resonance changes from $g_4 - g_3$ to $2(g_4 - g_3)$ periods in the Cretaceous between ~83 and 93 Ma, which were then addressed to further amplitude investigations. In accordance with Ma et al. (2019), we confirmed the findings by comparing the amplitudes of additionally filtered $g_4 - g_3$ and $2(g_4 - g_3)$ components, which exhibit a specific ratio pattern during a chaotic interval. Our frequency analyses of the Newark-Hartford datasets exposed a shortened $g_4 - g_3$ period between 202 and 229 Ma, which could be interpreted as an evidence for astronomical chaos somewhere between ~50 and ~200 Ma The recent $g_4 - g_3$ period of 2.364 Myr changes into a new shorter $g_4 - g_3$ period after a chaotic transition (Laskar et al., 2011a; Olsen et al., 2019).

4.7. Acknowledgements

M.R. and H.P. were funded by the European Research Council Consolidator Grant Earth Sequencing (grant agreement 617462).

4.8. References

Eldrett, J.S., Ma, C., Bergman, S.C., Lutz, B., Gregory, F.J., Dodsworth, P., Phipps, M., Hardas, P., Minisini, D., Ozkan, A., Ramezani, J., Bowring, S.A., Kamo, S.L., Ferguson, K., Macaulay, C., Kelly, A.E., 2015. An astronomically calibrated stratigraphy of the Cenomanian, Turonian and earliest Coniacian from the Cretaceous Western Interior Seaway, USA: Implications for global chronostratigraphy. Cretac. Res. 56, 316–344. https://doi.org/10.1016/j.cretres.2015.04.010

Emery, L., Borland, M., Shang, H., Soliday, R., 2008. User ' s Guide for SDDS-compliant EPICS Toolkit Version 1 . 5.

Gradstein, F.M., Ogg, J.G., Schmitz, M.D., Ogg, G.M., 2012. The Geologic Time Scale 2012. https://doi.org/10.1016/B978-0-444-59425-9.01001-5

Hilgen, F.J., Lourens, L.J., Van Dam, J.A., Beu, A.G., Boyes, A.F., Cooper, R.A., Krijgsman, W., Ogg, J.G., Piller, W.E., Wilson, D.S., 2012. The Neogene Period, The Geologic Time Scale 2012. Elsevier. https://doi.org/10.1016/B978-0-444-59425-9.00029-9

Hinnov, L.A., 2013. Cyclostratigraphy and its revolutionizing applications in the earth and planetary sciences. Bull. Geol. Soc. Am. 125, 1703–1734. https://doi.org/10.1130/B30934.1

Hinnov, L.A., 2000. New Perspectives on orbitally forced Stratigraphy 12, 727–732.

https://doi.org/10.1177/0741713604268894
Hinnov, L.A., Hilgen, F.J., 2012. Cyclostratigraphy and Astrochronology. Geol. Time Scale 2012 1–2, 63–83. https://doi.org/10.1016/B978-0-444-59425-9.00004-4
Hinnov, L.A., Schulz, M., Yiou, P., 2002. Interhemispheric space-time attributes of the Dansgaard-Oeschger oscillations between 100 and 0 ka. Quat. Sci. Rev. 21, 1213–1228. https://doi.org/10.1016/S0277-3791(01)00140-8
Laskar, J., 2003. Frequency map analysis and quasiperiodic decompositions. https://doi.org/10.1109/PAC.2003.1288929
Laskar, J., 1990. The chaotic motion of the solar system: A numerical estimate of the size of the chaotic zones. Icarus 88, 266–291. https://doi.org/10.1016/0019-1035(90)90084-M
Laskar, J., Fienga, A., Gastineau, M., Manche, H., 2011a. La2010: A new orbital solution for the long term motion of the Earth 4. https://doi.org/10.1051/0004-6361/201116836
Laskar, J., Gastineau, M., Delisle, J.-B., Farrés, A., Fienga, A., 2011b. Strong chaos induced by close encounters with Ceres and Vesta. Astron. Astrophys. 532, L4. https://doi.org/10.1051/0004-6361/201117504
Laskar, J., Robutel, P., Joutel, F., Gastineau, M., Correia, A.C.M., Levrard, B., 2004. A long-term numerical solution for the insolation quantities of the Earth. Astron. Astrophys. 428, 261–285. https://doi.org/10.1051/0004-6361:20041335
Locklair, R.E., Sageman, B.B., 2008. Cyclostratigraphy of the Upper Cretaceous Niobrara Formation, Western Interior, U.S.A.: A Coniacian-Santonian orbital timescale. Earth Planet. Sci. Lett. 269, 540–553. https://doi.org/10.1016/j.epsl.2008.03.021
Ma, C., Meyers, S.R., Sageman, B.B., 2019. Testing Late Cretaceous astronomical solutions in a 15 million year astrochronologic record from North America. Earth Planet. Sci. Lett. 513, 1–11. https://doi.org/10.1016/j.epsl.2019.01.053
Ma, C., Meyers, S.R., Sageman, B.B., 2017. Theory of chaotic orbital variations confirmed by Cretaceous geological evidence. Nature 542, 468–470. https://doi.org/10.1038/nature21402
Meyers, S.R., 2014. Astrochron: An R Package for Astrochronology.
Olsen, P.E., Kent, D. V., Cornet, B., Witte, W.K., Schlische, R.W., 1996. High-resolution stratigraphy of the Newark rift basin (early Mesozoic, eastern North America). Geol. Soc. Am. Bull. 108, 40–77. https://doi.org/10.1130/0016-7606(1996)108<0040:hrsotn>2.3.co;2
Olsen, P.E., Laskar, J., Kent, D. V., Kinney, S.T., Reynolds, D.J., Sha, J., Whiteside, J.H., 2019. Mapping Solar System chaos with the Geological Orrery. Proc. Natl. Acad. Sci. 201813901. https://doi.org/10.1073/PNAS.1813901116
R, D.C.T., 2016. R: A Language and Environment for Statistical Computing. R Found. Stat. Comput. https://doi.org/10.1007/978-3-540-74686-7
Taner, M.T., Koehler, F., Sheriff, R.E., 1979. Complex seismic trace analysis. Geophysics 44, 1041–1063. https://doi.org/10.1190/1.1440994
Vakman, D., 1996. On the analytic signal the teager-kaiser energy algorithm and

other methods for defining amplitude and frequency. IEEE Trans. Signal Process. 44, 791–797. https://doi.org/10.1109/78.492532
Zeeden, C., Kaboth, S., Hilgen, F.J., Laskar, J., 2018. Taner filter settings and automatic correlation optimisation for cyclostratigraphic studies. Comput. Geosci. 119, 18–28. https://doi.org/10.1016/j.cageo.2018.06.005

Chapter 5

General Conclusion and Outlook

The primary aim of this thesis was to develop innovative methods for detecting signatures of astronomical chaos in geological data and to search for chaotic transitions in geological time series. In order to verify and extend astronomical solutions, it is important to determine the imprint of chaotic transitions in time series. The most important manifestation of solar system chaos is the change of two resonant astronomical frequencies of Mars' and Earth's orbit. To detect these resonance changes, we combined frequency-, filter- and amplitude-analyses, which definitely improve previous methodologies.

The application of these techniques made it possible to detect two chaotic transitions in a spliced record encompassing the Eocene, the Paleocene, and the Cretaceous-Paleogene boundary. The most recent transition was found between ~44 and ~52 Ma in accordance to (Westerhold et al., 2017) and a further one was detected between ~62 and ~66 Ma. An additional test could confirm reported evidences for astronomical chaos in the Late Cretaceous between 84 and 93 Ma (Ma et al., 2019) and between 202 and 229 Ma of Jurassic-Triassic borehole datasets (Olsen et al., 2019).

In order to determine how resonance patterns appear, the tests and improvements of several techniques were obtained with the help of the astronomical solutions La2004, La2010c (Laskar et al., 2011a, 2004) and ZB17e (Zeebe, 2017), which provide time series with well-known positions of resonance switches. Fundamental and instantaneous frequency analyses can indicate resonance transitions exactly where they were calculated and predicted to occur in the respective solution. Based on the results of frequency analyses, amplitude analyses of eccentricity and obliquity were performed, including additional inspections of extracted 2.4 and/or 1.2 Myr amplitudes. In intervals of a resonance transition the 1.2 Myr period reaches highest amplitude compared to 2.4 Myr which will vanish due to the resonance switch of (g_4 - g_3) to 2(g_4 - g_3). Comparing the amplitudes of filtered g_4 – g_3 and 2(g – g_3) components is particularly helpful and of great advantage over traditional filter and amplitude modulation inspections.

Previously tested and improved methods were applied on a continuous and high-resolution XRF splice consisting of iron datasets from seven globally distributed ODP/IODP Sites. To ensure the compatibility, all individual datasets were detrended and normalized before splicing, which was confirmed by further tests. Summarizing the subsequent offsets between the ages of three magnetochrons and one ELMO-Event

before and after splicing, the resulting age difference of -243 kyr in constrast to GTS2012 (Gradstein et al., 2012) for the Eocene-Oligocene boundary lies within error margins. Fundamental and instantaneous frequency analyses indicate intervals with resonance changes from $g_4 - g_3$ to $2(g_4 - g_3)$ periods from ~44 - ~52 Ma and between ~62 and ~66 Ma. Addressing these intervals to further amplitude investigations confirm these results. In comparison with astronomical solutions, it was determined that La2010a and La2010d match best with the here analysed geological data.
Supporting previous findings, the methods were subjected to further tests. For these tests, two recent studies reporting evidences for astronomical chaos in various type of geological data were selected: a) Olsen et al. (2019) discovered shorter $g_4 - g_3$ cycles of 1.747 Myr between 202 and 229 Ma in sonic velocity and gamma radiation borehole measurements of the Newark–Hartford plateau and b) Ma et al. (2019) detected two chaotic transitions in the Cretaceous between 84 and 93 Ma in Formation Micro-resistivity Imaging and $\delta^{13}C$ data of North American Libsack and Iona cores. The application of a combination of frequency-, filter- and amplitude analyses confirmed the studies, while the amplitudes of additionally filtered $g_4 - g_3$ and $2(g_4 - g_3)$ components exhibit the specific ratio pattern during the chaotic intervals of 84 - 88 and 89 - 93 Ma. The frequency analyses of the Newark-Hartford datasets exposed a shortened $g_4 - g_3$ period between 202 and 229 Ma.

This PhD project tests and provides useful and improved methodologies to detect astronomical chaos in geological data. Although individual methods have constraints and caution is required with real geological data, the combination of the tested techniques and the additional filtering of $g_4 - g_3$ and $2(g_4 - g_3)$ periods is immensely supportive.

Nonetheless, to make well founded conclusions, additional research is needed, and in the following, several ideas are provided:

- A similar study on different proxies for the time spanning the Eocene, the Paleocene, and the Cretaceous-Paleogene boundary would be relevant to support (or challenge) the findings.

- It would also be important to extend the investigations and search for astronomical chaos in geological data of the Late Cretaceous from the Cretaceous-Paleogene boundary to ~83 (Ma et al., 2019).

- An expansion of fundamental frequency analyses could be achieved by obtaining individual g-frequencies. As outlined and carried out by Olsen et al. (2019), the secular frequency g_5 of Jupiter is considered a constant (4.25 arcseconds/y, Laskar et al., 2011), and g_2 is obtained from the stable 405 kyr cycle ($g_2 - g_5$). In addition, it is possible to recover g_1 from $g_1 - g_5$, g_3 from $g_3 - g_5$, g_4 from $g_4 - g_5$.

5.1. References

Gradstein, F.M., Ogg, J.G., Schmitz, M.D., Ogg, G.M., 2012. The Geologic Time Scale 2012. https://doi.org/10.1016/B978-0-444-59425-9.01001-5

Laskar, J., Fienga, A., Gastineau, M., Manche, H., 2011. La2010: A new orbital solution for the long term motion of the Earth 4. https://doi.org/10.1051/0004-6361/201116836

Laskar, J., Robutel, P., Joutel, F., Gastineau, M., Correia, A.C.M., Levrard, B., 2004. A long-term numerical solution for the insolation quantities of the Earth. Astron. Astrophys. 428, 261–285. https://doi.org/10.1051/0004-6361:20041335

Ma, C., Meyers, S.R., Sageman, B.B., 2019. Testing Late Cretaceous astronomical solutions in a 15 million year astrochronologic record from North America. Earth Planet. Sci. Lett. 513, 1–11. https://doi.org/10.1016/j.epsl.2019.01.053

Olsen, P.E., Laskar, J., Kent, D. V., Kinney, S.T., Reynolds, D.J., Sha, J., Whiteside, J.H., 2019. Mapping Solar System chaos with the Geological Orrery. Proc. Natl. Acad. Sci. 201813901. https://doi.org/10.1073/PNAS.1813901116

Westerhold, T., Röhl, U., Frederichs, T., Agnini, C., Raffi, I., Zachos, J.C., Wilkens, R.H., 2017. Astronomical Calibration of the Ypresian Time Scale: Implications for Seafloor Spreading Rates and the Chaotic Behaviour of the Solar System? Clim. Past Discuss. 1–34. https://doi.org/10.5194/cp-2017-15

Zeebe, R.E., 2017. Numerical Solutions for the orbital motion of the Solar System over the Past 100 Myr: Limits and new results. Astron. J. 154, 193. https://doi.org/10.3847/1538-3881/aa8cce

Zeeden, C., Kaboth, S., Hilgen, F.J., Laskar, J., 2018. Taner filter settings and automatic correlation optimisation for cyclostratigraphic studies. Comput. Geosci. 119, 18–28. https://doi.org/10.1016/j.cageo.2018.06.005

Appendices

A.1 Supplementary Information for Chapter 2: Detecting chaotic transitions in geological time series: Applying improved methodologies

1. Filter settings for reconstructing relevant astronomical components

Please note that the appended R script uses noise generation. Because not for one part this depends on random number generation, the results from different runs may vary. The R-Script for testing filter settings used for this study can be downloaded here: https://www.dropbox.com/s/lxgd8g4y0k2cobg/testFilterPropoerties_100kyrecc_noise.R?dl=0

Filter settings of short eccentricity

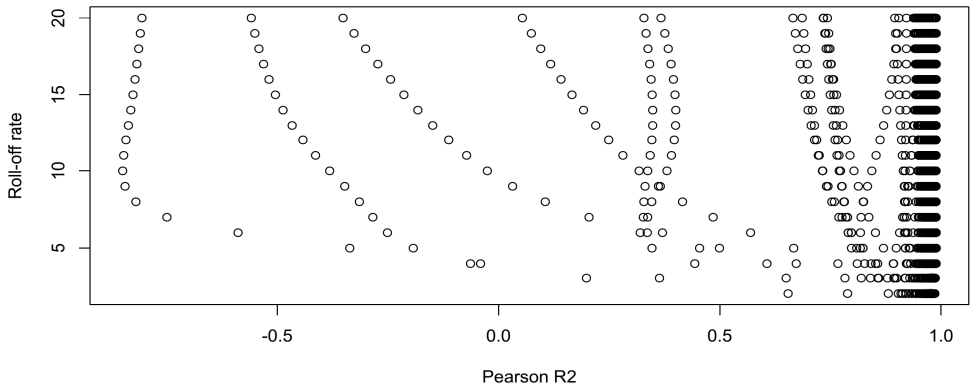

Supplementary Figure A1. Dependency of correlation coefficient and roll-off rate for experiments.

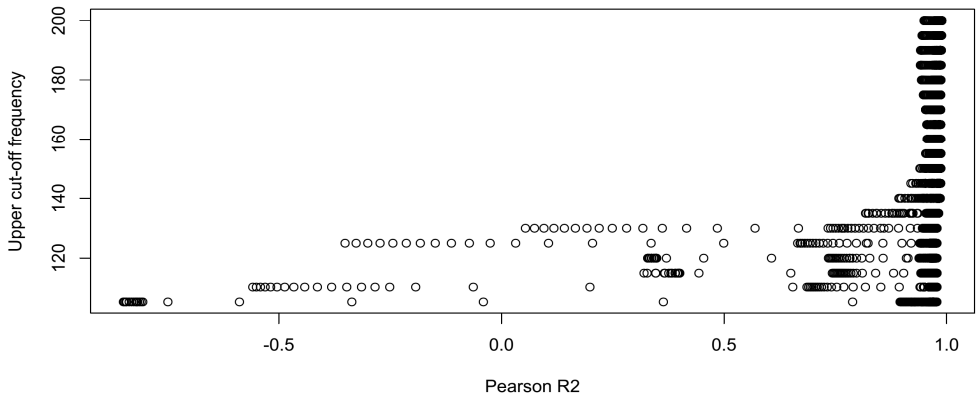

Supplementary Figure A2. Dependency of correlation coefficient and the upper cut-off frequency of Taner filter settings for experiments.

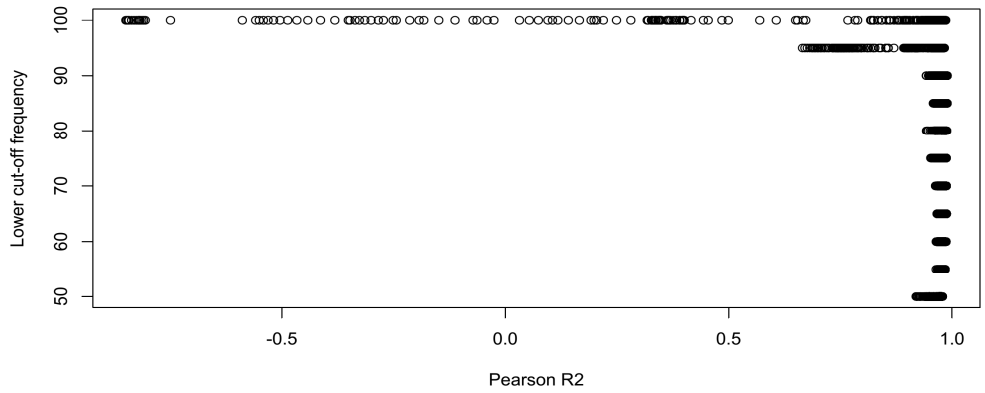

Supplementary Figure A3. Dependency of correlation coefficient and the lower cut-off frequency of Taner filter settings for experiments.

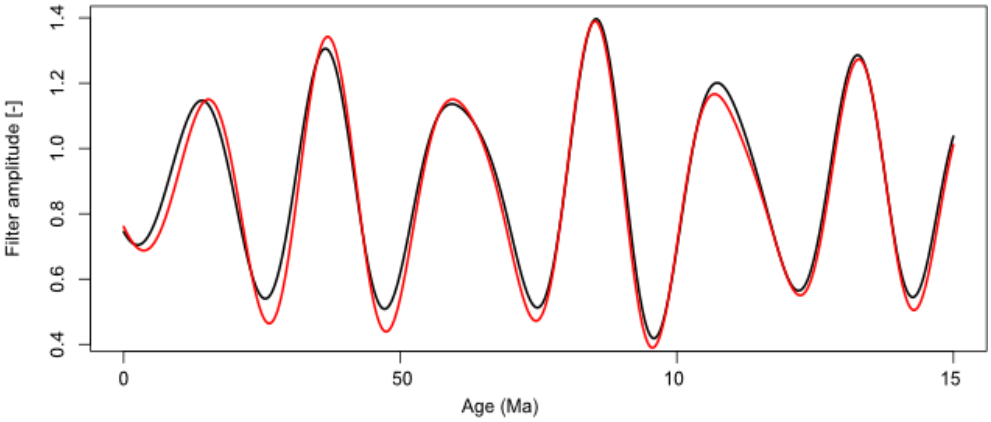

Supplementary Figure A4. Comparison of extracting the ~2/2.4 Ma eccentricity component from amplitude modulations of the ~100 ka component. Red: as extracted from clean eccentricity, black: reconstructed from a noisy ETP signal.

Filter settings of long eccentricity

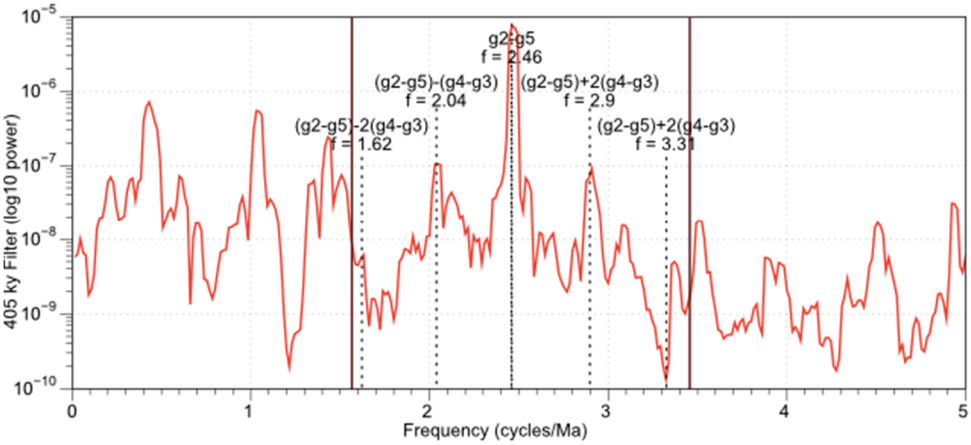

Supplementary Figure A5. Filter for 405 kyr eccentricity to include all needed frequency terms (see Laskar 2011). We filtered between 1.538 cycles/Ma and 3.571 cycles/Ma.

2. Amplitude modulation of short eccentricity

La2004

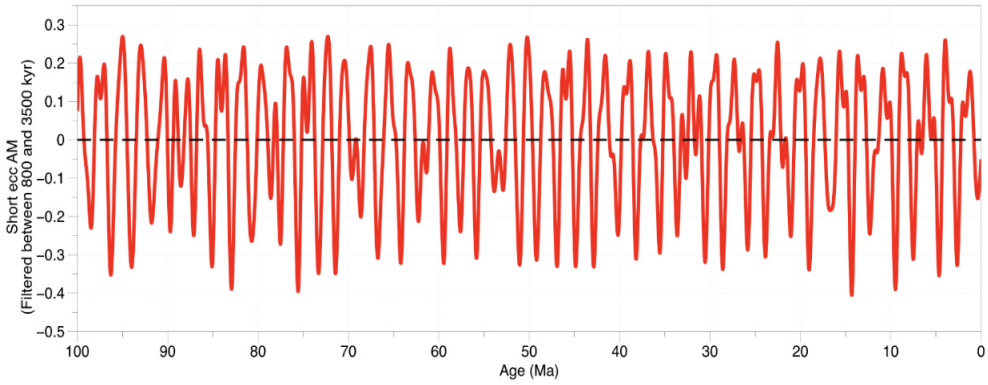

Supplementary Figure A6. La2004, 0 – 100 Ma. Amplitude modulation of short eccentricity, filtered between 800 and 3500 ky. As a consequence of an amplitude around zero at ~ 32, the calculation of phase and frequency is impossible.

Zb17e

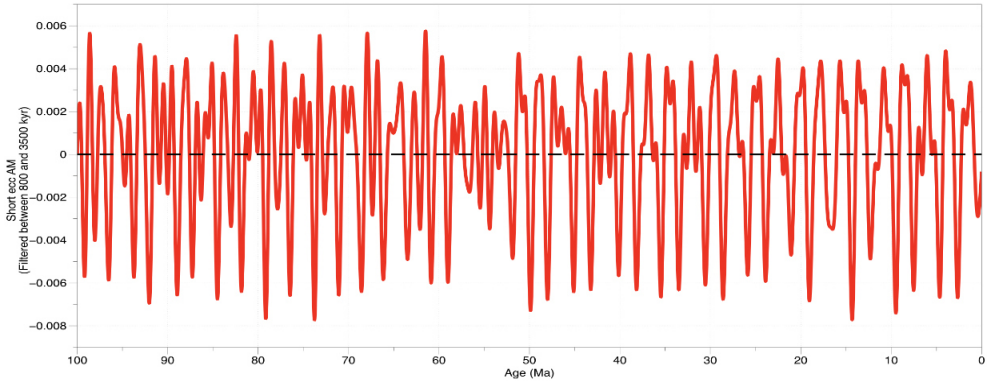

Supplementary Figure A7. Zb17e, 0 – 100 Ma. Amplitude modulation of short eccentricity, filtered between 800 and 3500 ky. As a consequence of an amplitude around zero at ~ 43 and ~90 Ma, the calculation of phase and frequency is impossible.

La2010c

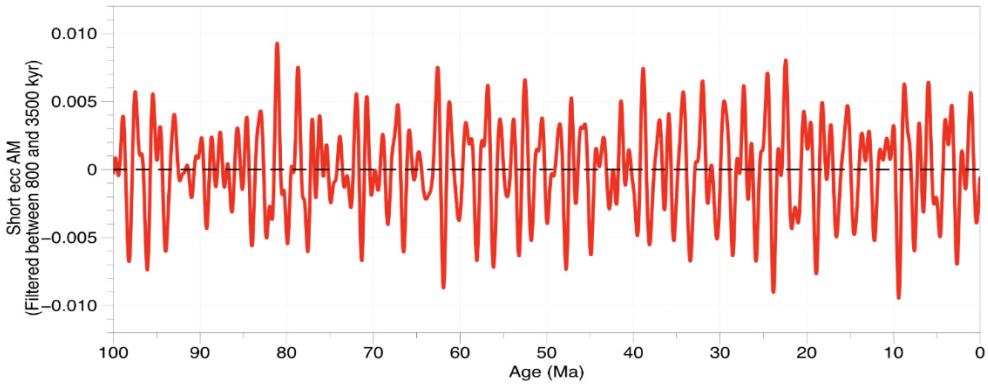

Supplementary Figure A8. La2010c with AR1, 0 – 100 Ma. Amplitude modulation of short eccentricity, filtered between 800 and 3500 ky. As a consequence of a zero amplitude at ~ 18 Ma, ~ 26 Ma, ~78 Ma for example, the calculation of phase and frequency is impossible.

Site 1258

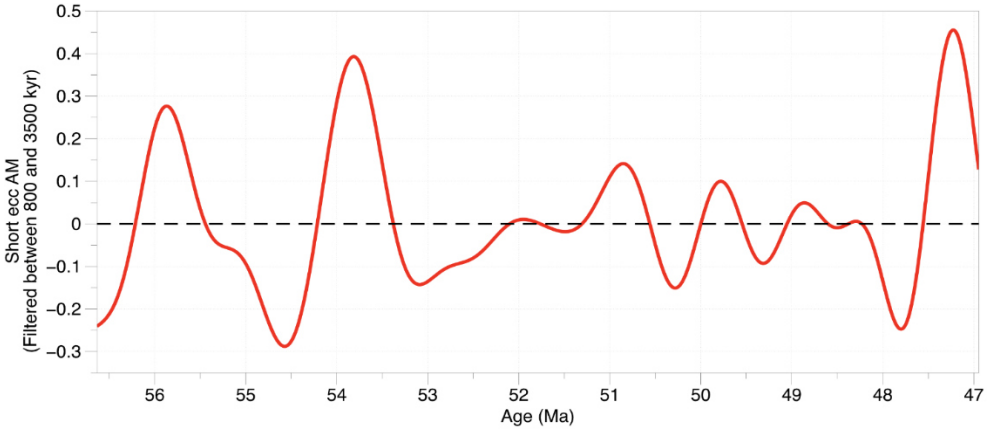

Supplementary Figure A9. Site 1258. Amplitude modulation of short eccentricity, filtered between 800 and 3500 ky. As a consequence of a zero amplitude at ~ 48.5 and ~ 52 Ma, the calculation of phase and frequency is impossible.

A.2 Supplementary Information for Chapter 3: Investigating astronomical chaos in the Eocene-Paleocene-Late Cretaceous 69-34 Ma

1. XRF splice datasets, interpolated log_{10}Fe signal

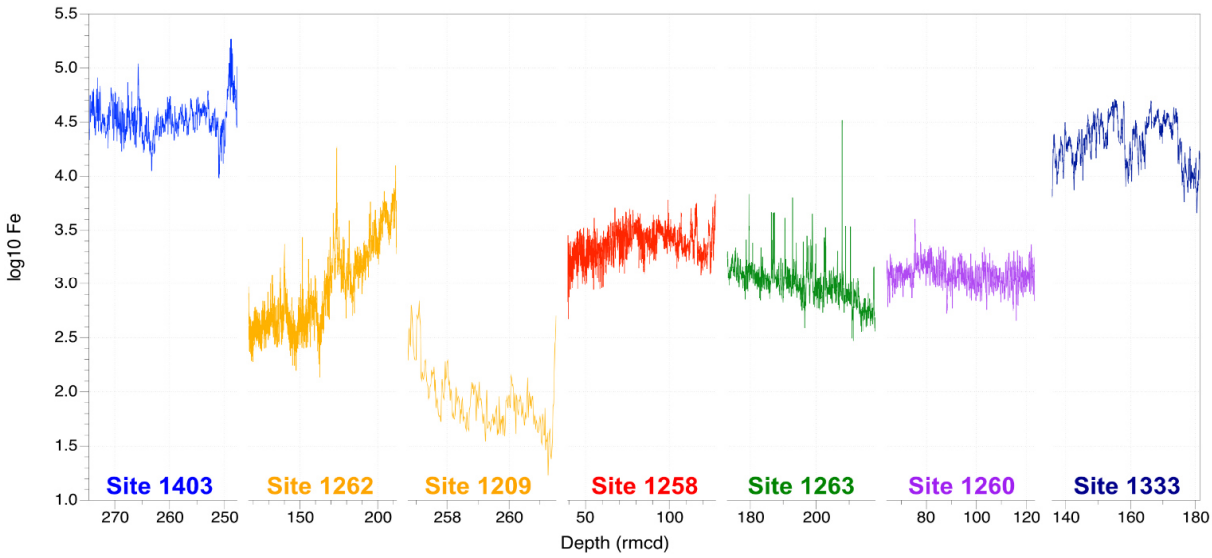

Supplementary Figure B1. All log_{10} Fe datasets individually interpolated with dtmean (see Table 2.1 in manuscript) in depth domain (rmcd).

The K/Pg-Splice data including results from frequency analyses can be downloaded here: https://www.dropbox.com/s/82pn7pedvfl5e3l/Supplement_Splice.xlsx?dl=0

2. Fundamental frequency analyses

The source code for Fortran can be found here:
https://paloz.marum.de/confluence/display/ESPUBLIC/NAFF
We performed NAFF on short eccentricity amplitude modulation filtered between 1/3500 and 1/800 Myr.
The code line is:
./hpnaff K/Pg_Splice_AM100.txt -o 3 -k 1 -s 3000 -w 191 -m 1 -d 3 -dC > NAFF_K/Pg_Splice_AM100.txt
While K/Pg_Splice_AM100.txt is the demodulated short eccentricity already filtered, s is the window size, w is the step interval, detrended by polynomial regression order 3.

3. Comparison with astronomical solutions

In order to show the regular pattern without a resonance transition, Thomson Multitaper (Thomson, 1982) evolutive analyses were conducted on La2010d (Laskar et al., 2011a) for the last 30 Ma.

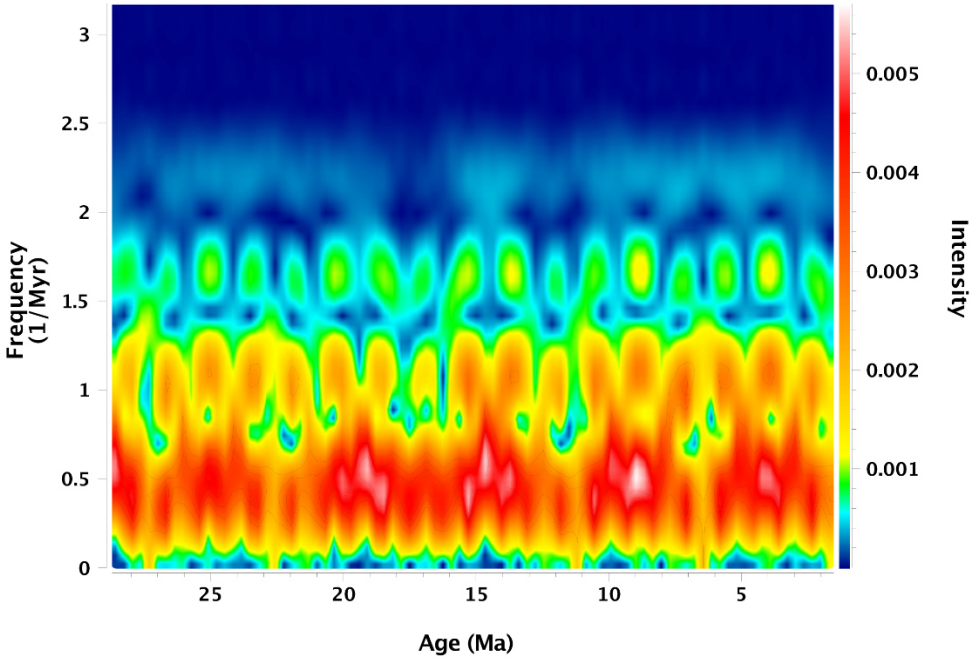

Supplementary Figure B2 Thomson Multitaper evolutive spectrum calculated from short eccentricity amplitude modulation filtered between 800 and 3500 kyr for La2010d, 0 – 30 Ma. The frequencies show a clear pattern without resonance shifts and a constant ~2.4 Myr (1/0.00041 kyr) period.

A.3 R-function ‘Chaos Search’: Script for filtering relevant cycles

The following script filters 2.4 Myr and 1.2 Myr from eccentricity and/or obliquity amplitude modulation to detect resonance transitions. It uses the free statistical software R (R Core Team, 2016; https://cran.r-project.org) and the package Astrochron (Meyers, 2014; https://cran.rproject.org/package=astrochron).

```
### Taner filter settings ###
# roll-off rate 10^10
# Long eccentricity: 280 - 630 kyr
# Short eccentricity: 85 - 160 kyr
# Obliquity: 35 - 45 kyr
# Inclination:
# s3 and s4: 65 - 77 kyr
### required: ETP dataset, 2 columns, 1 = age, 2 = ETP/Signal
# add period option:
# long eccentricity: 405
# short eccentricity: 100
# Obliquity: Tilt

# call function
chaosSearch <- function(dat, period ="100") {

if (period == "405"){
# extract eccentricity
eccDat = data.frame(dat[,1], dat[,2])

### Filter long eccentricity between 280 kyr and 630 kyr
longEcc_filter = taner(eccDat, padfac=8, flow=1/630, fhigh=1/280, roll=10^10, demean=F,
detrend=F, addmean=F, output=1, xmin=0, xmax=0.07, genplot=T, verbose=T)

# perform Hilbert transformation of 405 kyr Filter
longEcc_AM = hilbert(longEcc_filter, padfac=2, demean=F, detrend=F, output=T,
addmean=F,genplot=T,verbose=T)

# Filter 2.4 and 1.2 Myr cycle in long eccentricity amplitude modulation
# 2.4 Myr cycle between 1.8 and 3.5 Myr
Filter_2.4My_405AM = taner(longEcc_AM, padfac=8, flow=1/3500, fhigh=1/1800,
roll=10^10, demean=F, detrend=F, addmean=F, output=1, xmin=0, xmax=0.07, genplot=T,
verbose=F)
```

```
# 1.2 Myr cycle between 800 kyr and 1.8 Myr
Filter_1.2My_405AM = taner(longEcc_AM, padfac=8, flow=1/1800, fhigh=1/800, roll=10^10,
demean=F, detrend=F, addmean=F, output=1, xmin=0, xmax=0.07, genplot=T, verbose=F)

# return data to workspace
AM405_Search = list(age=dat[,1],
longEcc_AM = longEcc_AM[, 2],
Filter_2.4My_405AM = Filter_2.4My_405AM[, 2],
Filter_1.2My_405AM = Filter_1.2My_405AM[,2])
list2env(AM405_Search, envir = .GlobalEnv )
}
##################


if (period == "100"){
# extract eccentricity
eccDat = data.frame(dat[, 1], dat[, 2])

# Filter short eccentricity between 85 kyr and 160 kyr (tested)
shortEcc_filter = taner(eccDat, padfac=8, flow=1/160, fhigh=1/85, roll=10^10, demean=F,
detrend=F, addmean=F, output=1, xmin=0, xmax=0.07, genplot=T, verbose=F)

# perform Hilbert transformation of 100 kyr Filter
shortEcc_AM = hilbert(shortEcc_filter, padfac=2, demean=F, detrend=F, output=T,
addmean=F,genplot=T,verbose=T)

# Filter 2.4 and 1.2 Myr cycle in short eccentricity amplitude modulation
# 2.4 Myr cycle between 1.8 and 3.5 Myr
Filter_2.4My_100AM = taner(shortEcc_AM, padfac=8, flow=1/3500, fhigh=1/1800,
roll=10^10, demean=F, detrend=F, addmean=F, output=1, xmin=0, xmax=0.07, genplot=T,
verbose=F)

# 1.2 Myr cycle between 800 kyr and 1.8 Myr
Filter_1.2My_100AM = taner(shortEcc _AM, padfac=8, flow=1/1800, fhigh=1/800,
roll=10^10, demean=F, detrend=F, addmean=F, output=1, xmin=0, xmax=0.07, genplot=T,
verbose=F)

# return data to workspace
AM100_Search = list(age=dat[, 1],
shortEcc_AM = shortEcc_AM[,2],
Filter_2.4My_100AM = Filter_2.4My_100AM[,2],
Filter_1.2My_100AM = Filter_1.2My_100AM[,2])
list2env(AM100_Search,envir=.GlobalEnv )
}
##################
```

```
if (period == "Tilt"){
# extract obliquity
tiltDat = data.frame(dat[, 1], dat[, 2])

# Filter obliquity between 28 kyr and 54 kyr
obliquity_filter=taner(tiltDat, padfac=8, flow=1/54, fhigh=1/35, roll=10^10, demean=F,
detrend=F, addmean=F, output=1, xmin=0, xmax=0.07, genplot=T, verbose=F)

# perform Hilbert transformation of obliquity Filter
obliquity_AM = hilbert(obliquity_filter, padfac=2, demean=F, detrend=F, output=T,
addmean=F,genplot=T,verbose=T)

# Filter 2.4 and 1.2 Myr cycle in obliquity amplitude modulation
# 2.4 Myr cycle between 1.8 and 3.5 Myr
Filter_2.4My_OblAM=taner(obliquity_AM, padfac=8, flow=1/3500, fhigh=1/1800,
roll=10^10, demean=F, detrend=F, addmean=F, output=1, xmin=0, xmax=0.07, genplot=T,
verbose=F)

# 1.2 Myr cycle between 800 kyr and 1.8 Myr
Filter_1.2My_OblAM = taner(obliquity_AM, padfac=8, flow=1/1800, fhigh=1/800,
roll=10^10, demean=F, detrend=F, addmean=F, output=1, xmin=0, xmax=0.07, genplot=T,
verbose=F)

# return data to workspace
AMObliquity_Search = list(age=dat[, 1],
obliquity_AM = obliquity_AM[, 2],
Filter_2.4My_OblAM = Filter_2.4My_OblAM[, 2],
Filter_1.2My_OblAM = Filter_1.2My_OblAM[, 2])
list2env(AMObliquity_Search,envir =.GlobalEnv )
}
##################


if (period == "Incl"){
# extract inclination, used for Zb17e, Chapter 2
incldat = data.frame(dat[, 1],dat[, 3])

# Filter s3 and s4 in inclination between 65 kyr and 77 kyr
Filter_Incl = taner(incldat, padfac=8, flow=1/76, fhigh=1/65, roll=10^10, demean=F,
detrend=F, addmean=F, output=1, xmin=0, xmax=0.07, genplot=T, verbose=F)

# perform Hilbert transformation of inclination s3 and s4
Filter_Incl_AM = hilbert(Filter_Incl, padfac=1, demean=F, detrend=F, output=T, addmean=F,
genplot=T, verbose=T)

# Filter 2.4 and 1.2 Myr cycle in inclination amplitude modulation
# 2.4 Myr cycle between 1.8 and 3.5 Myr
```

```
Filter_2.4My_AMIncl = taner(Filter_Incl_AM, padfac=8, flow=1/3500, fhigh=1/1800,
roll=10^10, demean=F, detrend=F, addmean=F, output=1, xmin=0, xmax=0.07, genplot=T,
verbose=F)

# 1.2 Myr cycle between 800 kyr and 1.8 Myr
Filter_1.2My_AMIncl = taner(Filter_Incl_AM, padfac=8, flow=1/1800, fhigh=1/800,
roll=10^10, demean=F, detrend=F, addmean=F, output=1, xmin=0, xmax=0.07, genplot=T,
verbose=F)

# return data to workspace
AMIncl_Search = list(age=dat[, 1],
Filter_Incl_AM = Filter_Incl_AM[, 2],
Filter_2.4My_AMIncl = Filter_2.4My_AMIncl[, 2],
Filter_1.2My_AMIncl = Filter_1.2My_AMIncl[, 2])
list2env(AMIncl_Search,envir =.GlobalEnv ) }}
```